Engineering Journal

American Institute of Steel Construction

Engineering Journal

American Institute of Steel Construction

Dedicated to the development and improvement of steel construction, through the interchange of ideas, experiences and data.

The articles contained herein are not intended to represent official attitudes, recommendations or policies of the Institute. The Institute is not responsible for any statements made or opinions expressed by contributors to this Journal.

The opinions of the authors herein do not represent an official position of the Institute, and in every case the officially adopted publications of the Institute will control and supersede any suggestions or modifications contained in any articles herein.

The information presented herein is based on recognized engineering principles and is for general information only. While it is believed to be accurate, this information should not be applied to any specific application without competent professional examination and verification by a licensed professional engineer. Anyone making use of this information assumes all liability arising from such use.

Manuscripts are welcomed, but publication cannot be guaranteed. All manuscripts should be submitted in duplicate. Authors do not receive a remuneration. Guidelines for authors are printed on the inside back cover.

Engineering Journal (ISSN 0013-8029) is published quarterly. Subscriptions: Members: one subscription, $40 per year, included in dues; Additional Member Subscriptions: $40 per year. Non-Members U.S.: $160 per year. Foreign (Canada and Mexico): Members $80 per year. Non-Members $160 per year. Published by the American Institute of Steel Construction at 130 E. Randolph Street, Suite 2000, Chicago, IL 60601.

Periodicals postage paid at Chicago, IL and additional mailing offices. **Postmaster:** Send address changes to *Engineering Journal* in care of the American Institute of Steel Construction, 130 E. Randolph Street, Suite 2000, Chicago, IL 60601.

Subscriptions: subscriptions@aisc.org, 312.670.2400

Archives: Search at **www.aisc.org/ej**. Article downloads are free for current members and are avaialable for a nominal fee for non-members.

Experimental Investigation of a Steel-Framed Building for Disproportionate Collapse

EBIJI AKAH, CURTIS WOOD, KAI LI and HALIL SEZEN

ABSTRACT

This paper presents the experimental and numerical investigation of the progressive collapse vulnerability of an existing steel building, Haskett Hall, on the Ohio State University campus. The building was tested by removing one of the first-story columns to observe its collapse resistance and to evaluate the effectiveness of current modeling and analysis guidelines. Progressive collapse is a relatively large partial or complete collapse of a structure due to the loss of a vertical load-carrying element—a column in this case. Few researchers have been able to conduct full-scale experiments to understand the progressive collapse mechanism. In this research, deflections and deformations of steel structural components were measured during the field experiment. Computational models and simulations were examined and compared with the experimental data from the field tests. The contribution and effects of infill walls to progressive collapse resistance of frame structures were investigated. The test data collected in this research can be used to help develop recommendations for improved procedures for progressive collapse analysis of frame buildings.

Keywords: steel frame, disproportionate collapse, full-scale experiment, infill wall.

BACKGROUND INFORMATION

The term *progressive collapse* can be defined as the partial or total collapse of a structure that may be caused by local structural failure. The General Services Administration (GSA), American Society of Civil Engineers (ASCE), and the U.S. Department of Defense (DoD) have developed guidelines to evaluate, design and improve progressive collapse resistance of existing and new buildings. The GSA (2013) outlines procedures to evaluate whether a building, based on its size and shape, is vulnerable to progressive collapse. ASCE 7 (2010) and the AISC *Seismic Provisions* (AISC, 2010) both outline approaches to maintain structural integrity when a load-carrying member is damaged. Lastly, UFC 4-023-03 outlines how to prevent progressive collapse in multistory buildings (DoD, 2013). This research uses these guidelines to test and analyze whether a given structure is susceptible to progressive collapse. This paper focuses on the instrumentation and testing of Haskett Hall,

shown in Figure 1, to determine the potential for progressive collapse. One column was removed from the building within a short time period, as recommended by the GSA design guidelines, by Loewendick Demolition Contractors in November 2013. The two-dimensional (2D) linear static and nonlinear dynamic structural analyses have been performed using structural analysis programs to compare with the simulated and experimental data. This experiment is part of a larger research program at the Ohio State University (OSU) involving steel frame, reinforced concrete, and masonry buildings. (Akah, 2015; Li, 2017; Song and Sezen, 2013; Song et al., 2014)

BUILDING DESCRIPTION

Haskett Hall was a four-story building built in 1925 on the OSU campus in Columbus, Ohio. The building consisted of classrooms, offices and laboratories. A section on the north side of the building was used as a three-story testing laboratory. According to the original construction drawings provided by OSU, the building included built-up steel columns using rivets and channels, reinforced concrete slabs for the flooring, and steel I-beams encased with concrete. Figure 2 shows the elevation of the exterior frame on the west side of the building, including dimensions between centerlines of beams and columns. The building included a grid of seven columns that ran in the north-south direction and six columns that ran in the east-west direction. The total number of primary columns for the building was 38 (Figure 3). Occasionally, joists below floor slabs were used in the east-west direction. Joists were typically spaced at 2.08 ft (0.64 m). Typical reinforced concrete slab thickness was 7.0 in. (178.0 mm) without joists and 2.5 in. (63.5 mm) with joists.

Ebiji Akah, Design Engineer, SMBH Inc., Columbus, OH. Email: eakah@smbhinc.com

Curtis Wood, Senior Structural Engineer, E.L. Robinson Engineering, Columbus, OH. Email: cwood@elrobinson.com

Kai Li, Ph.D. Candidate, Department of Civil, Environmental and Geodetic Engineering, The Ohio State University, Columbus, OH. Email: li.3910@osu.edu

Halil Sezen, Professor, Department of Civil, Environmental, and Geodetic Engineering, The Ohio State University, Columbus, OH. Email: sezen.1@osu.edu (corresponding)

Historic sections and built-up column members were represented by equivalent sections in the programs (SAP2000, 2011). Properties of these sections were based on the original plans and the AISC database of historically available sections, as described earlier (Brockenbrough, 2003). When the building was designed in 1924, structural steel had to conform to the ASTM A9-21 standard, which had a minimum required tensile strength of 60,000 psi and a minimum required yield point of 30,000 psi. Yield strength for the beams and columns are assumed to be 36,000 psi, also assuming the actual yield strength would be slightly higher than the required minimum. Some of these beams were encased with concrete with a specified compressive strength of 4,000 psi. The cross-section of the encased floor beams is shown in Section G-G in Figure 4. Steel beams located in the perimeter frames were partially encased in concrete for fireproofing (Figure 5). Beams were connected to columns using rivets through angles that were located on the bottom flanges and webs (Figure 5). The reinforced concrete slab on beams created a more rigid connection with some composite action. The primary columns within the building were built-up sections—I-sections bracketed by two channel sections that were connected with rivets (e.g., column 27 in Figure 3). The original plans did not detail specific beam types. The beam depth and weight/foot were listed as 15" I @42#, 18" I @55#, 24" BI @73.5# etc. Known beam dimensions were used to determine, for example, that the 15" I @42# was a B15×42. The remaining beams were not exposed during the experiment; therefore, the closest historic beams with "B" designation were chosen for consistency. If a "B" type beam was not available, "G" designated beams were used. Member selection considered historic standard sections that were available during the 1924 construction of Haskett Hall. A similar selection process was used for column sizes.
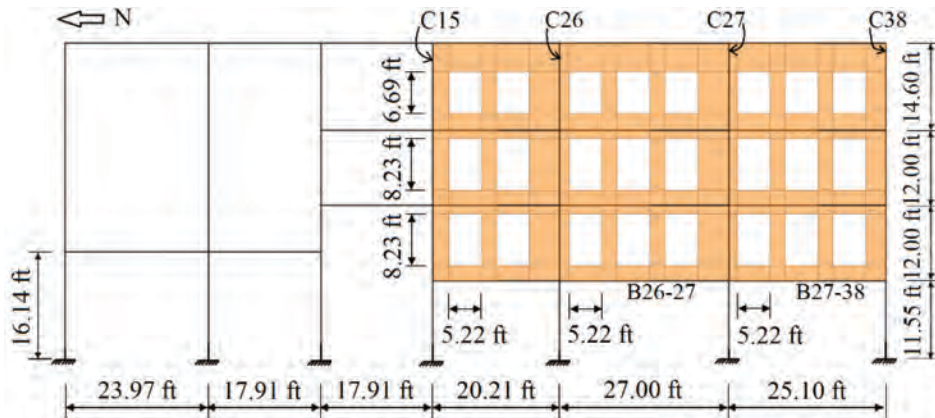

Fig. 1. Haskett Hall.

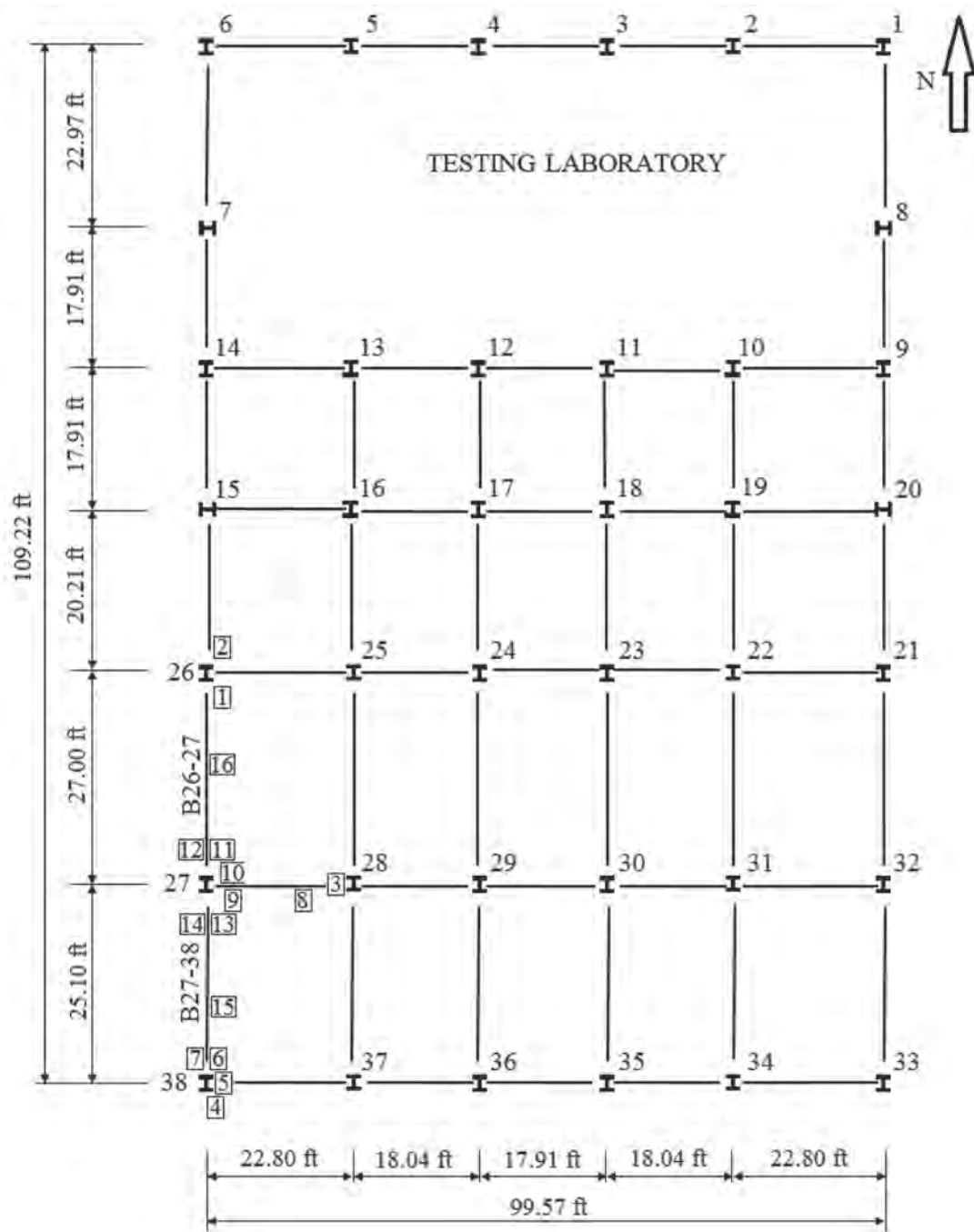*Fig. 2. Haskett Hall western elevation and bay layout.*

Fig. 3. Haskett Hall simplified layout with strain gauges on columns (numbered 1–7 in rectangle) and beams (8–16).

INSTRUMENTATION AND COLUMN REMOVAL

GSA (2013) specifies that buildings are analyzed for progressive collapse by removing a first-story column at the middle of the long side of the structure, the middle of the short side of the structure, and at a corner of the structure. However, after initial discussions with the demolition contractor, it became apparent that only one column would be removed by the demolition contractor structure. While not exactly in the middle of the long side of the building, column 27 (Figure 3) matched the closest to the GSA guidelines of the available columns. Column 27 was removed by the use of a processor—a hydraulic demolition shear equipment attached to a large trackhoe/excavator. The processor was placed around column 27 and a section of the column was crushed by the claws of the processor. By using the processor, column removal time was minimized. Table 1 details the column removal process.

Strain gauges, installed on three neighboring columns and three connecting beams, measured uniaxial strains during the column removal. Furthermore, linear variable differential transformer displacement sensors (LVDT) measured the vertical and horizontal vibrations and displacements around the removed column. A total of 16 strain gauges were used in the experiment: seven were attached to columns and nine were attached to beams. Columns 26, 27 and 38, along with the adjoining first-story beams, were exposed and cleaned for strain gauge attachment. Because Haskett Hall was a steel-framed building, only the brick façade and exterior infill walls were required to be removed. All interior drywall had previously been removed. The strain gauges were installed on both the flanges and the webs of the neighboring columns. All beams had gauges placed on the bottom face of the bottom flange. Column 26 had two gauges installed 3.08 ft from the base of the column. Column 38 had three gauges installed 6.17 ft from the base and one gauge 4.58 ft from the base. Column 28 had one gauge placed 4.58 ft from the base. Three LVDT or displacement sensors were used in Haskett Hall. Two LVDT were placed vertically on both side of column 27 and one LVDT was placed horizontally at the beam-column joint. Figures 3 and 6 show strain gauge and LVDT placement.

Fifteen strain gauges recorded dynamic strain data during column removal. There were five distinct physical events, and the corresponding measured strain histories helped understand the behavior of the building during those events. Initially, all strain gauges and displacement sensors had stable readings. When the processor made contact with the test column, strain and displacement values started to increase. A period for the processor began when the claw closed, making contact with the column (Figure 7, left), and ended when the claw opened and was no longer in contact with the column (Figure 7, right). These five periods are shown in Table 1. Figure 8 shows column 27 (in red circle) that was scheduled to be demolished before removal (top) and after removal (bottom).

Analysis of Measured Strains

The measured strains captured the effects of the processor movements and helped understand the response at the strain gauge locations. Figure 8 shows strain histories measured by strain gauges 1–7. It presents how the processor's contact with the column affected the measured strain values. At each time that the processor made contact with the removed column, there was a jump in the measured strain.
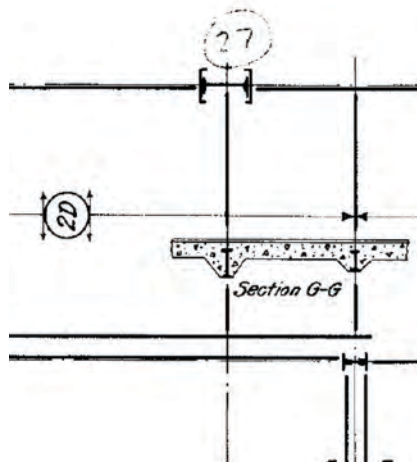

Fig. 4. Close-up detail of column 27 encased in concrete (partial plan view from original drawings), and beam-column connection with rivets through angle on beam bottom flange and web.
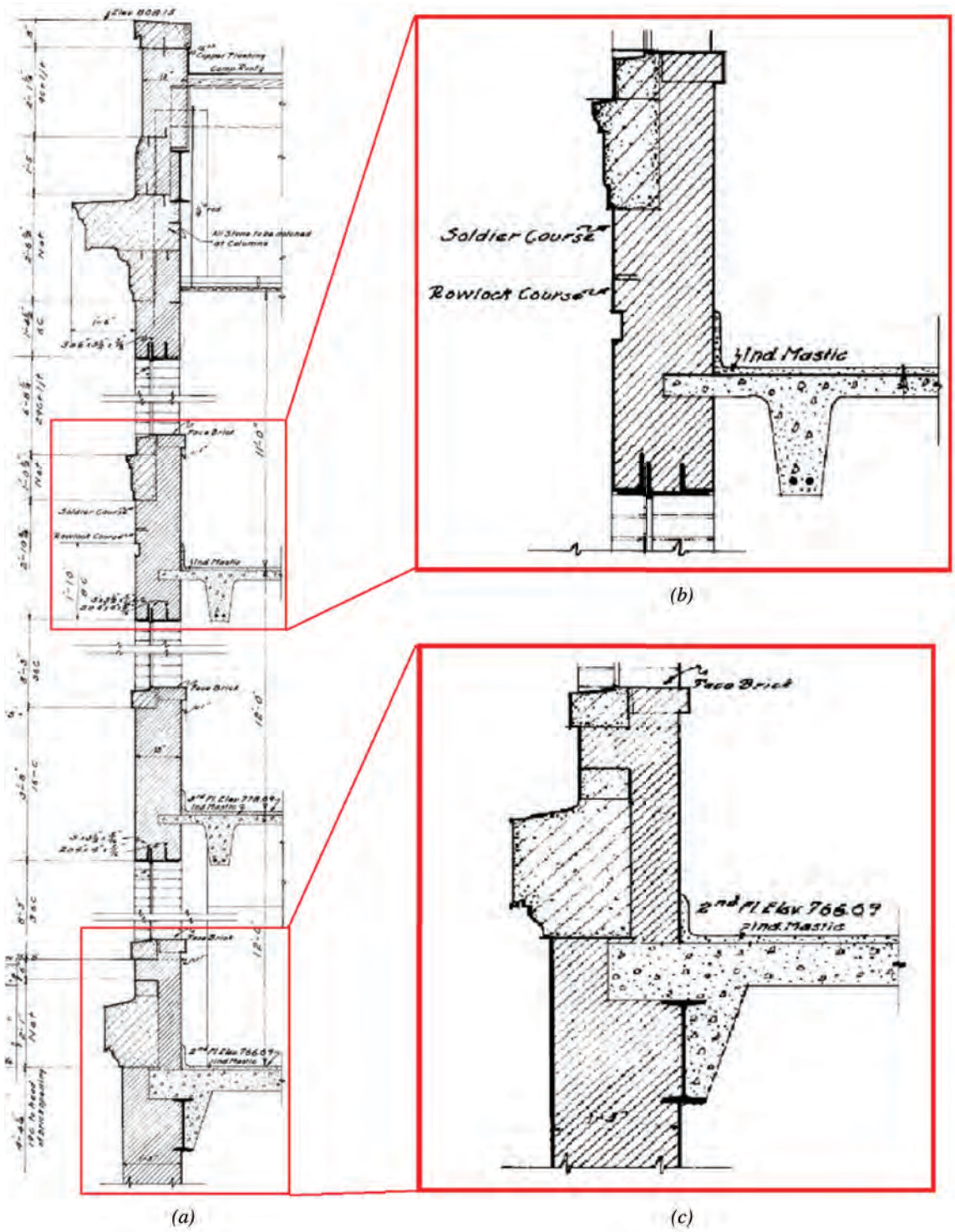
Fig. 5. (a) Façade cross-section from original drawings; (b) close-up of second floor; (c) close-up of fourth floor.

Table 1. Processor Contact with Test Column		
Contact Number and Event	**Contact Start Time, sec**	**Contact End Time, sec**
1. Strains/displacements increased from zero	168.5	177.7
2. Bricks in exterior column web crumbled	184.6	191.2
3. Column bent inward	208.6	218.5
4. Column warped and twisted by processor	221.6	231.8
5. Column was cut through and second floor beams deflected downward	247.8	251.7

*Fig. 6. Vertical LVDT to the south (in circle on left) and north (in circle on right)
of the removed column and horizontal LVDT (rectangle) attached to the removed column.*

Fig. 7. Column 27 under removal (left) and finished removal (right).

With strain gauge 3, the first contact time started at 168.49 seconds, with the processor closing its claw, and resulted in a strain increase of approximately -20×10^{-6} in./in. Negative strain values indicate compression and positive strain values indicate tension. Once the processor opened its claw and was no longer in contact with the column at a time of 177.65 seconds, the strain fell to -15×10^{-6} in./in. This overall decrease in strain exhibits the change, and overall increase, in axial compressive load on column 28. The same effect is apparent from when the processor closed and opened its claw three more times: from 184.61 to 191.17 seconds, 208.62 to 218.54 seconds, and 221.60 to 231.76 seconds. During these contact times, the column's inserted bricks began to crumble, the column became bent inward and started to become warped by the processor's twisting.

During the last processor contact time, which lasted from 247.77 to 251.74 seconds, the test column was completely cut through, and the connecting beams deflected downward.

It should be noted that the test column was cut by altering the position of the processor, meaning there was a three-dimensional cutting plane. In Figure 9, once the column was cut, the measured strain value drastically increased momentarily. Once the processor was no longer in contact with the cut column, the measured strain leveled out at approximately -29×10^{-6} in./in for strain gauge 3. Assuming the steel did not yield, the compressive axial stress increase, Δf, on the east side of column 28 was approximately 0.9 ksi— that is, $\Delta f = E_s \varepsilon_s = (29{,}000 \text{ ksi})(29 \times 10^{-6} \text{ in./in.})$.

Table 2 shows that each strain gauge located on a column measured a residual negative strain value, indicating that each column neighboring the removed column underwent compression once the test column was removed. The south column 38, which measured the largest negative residual strain, had to carry more additional axial force than the east column 28 or north column 26. Furthermore, the magnitude of strain values on the columns increased from south to

Fig. 8. Penultimate column 27 before removal (top) and after removal (bottom).

Table 2: Strain Values Measured at 300 Sec by Strain Gauges on Columns				
Gauge No.	Column	Location	Height on Column, ft	Strain, $\times 10^{-6}$ in./in.
1	26	South flange	3.08	−32
2	26	North flange	3.08	−54
3	28	West web	4.59	−29
4	38	South flange	6.17	−7
5	38	East web	6.17	−61
6	38	North flange	6.17	−103
7	38	North flange	4.59	−93

north and west to east, exhibiting that some limited the axial loads were being transferred into the building column 28 and 38.

Measured Displacements

Three displacement sensors recorded dynamic displacements during the column removal. When the processor made contact with the test column at 169 seconds, displacement values started to increase (Figure 10). The five times the processor made contact with the column are described in Table 1. Dynamic measurements of displacement that appear after 300 sec in Figure 11 were a result of the processor making contact with the test column, but for the sake of the experiment, data measurements were meant to be terminated once the column was completely removed shortly after 250 sec. The measured displacement data were compared with results from the structural analysis models. For

the purpose of presenting data clearly and straightforward, the vertical displacement scales of Figures 10 and 11 are different by a factor of 10.

STRUCTURAL MODELING AND ANALYSIS

Two-dimensional linear static (2D LS) and nonlinear dynamic (NLD) structural analyses of the western frame of Haskett Hall were performed in SAP2000 (2011). A critical modeling question is whether the steel beams behaved compositely with the concrete deck. Shear studs or other means of connection between the beams and slab were not used during construction of Haskett Hall. However, the beams were embedded into the concrete, as seen in Figures 4 and 5(b). In some instances, the concrete even extended the entire depth of the web. For structural analysis, it would be conservative to assume noncomposite behavior. However, this assumption may not yield results consistent with the field testing.
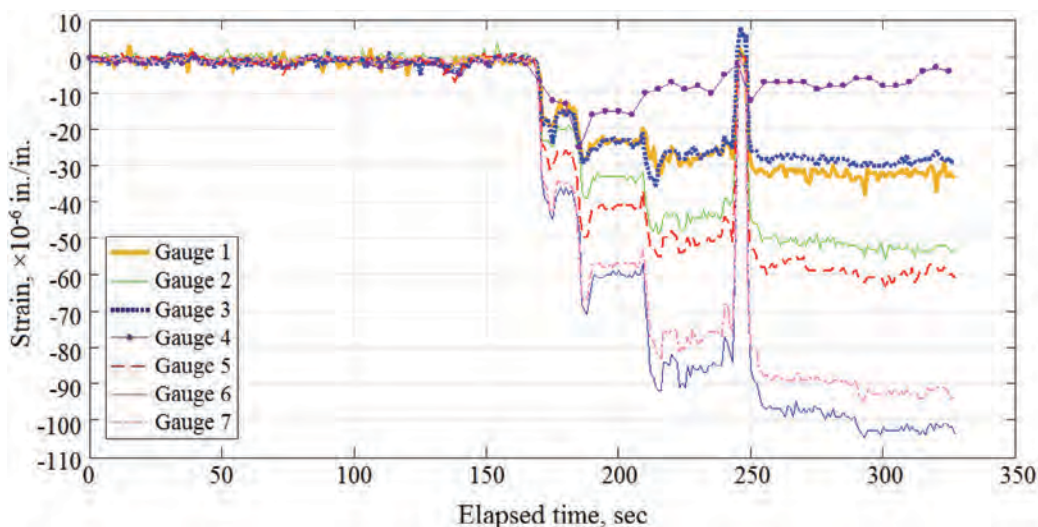

Fig. 9. Strain history measured by strain gauges 1–7 on steel columns.

Fig. 10. Comparison of measured LVDT deflections to linear static (LS) and nonlinear dynamic (NLD) calculated deflections of models: A (noncomposite beam, no slab in upper floors); B (composite beams, no slab in upper floors); C (noncomposite beams and ribbed slabs in upper floors); D (composite beams and ribbed slabs in upper floors).
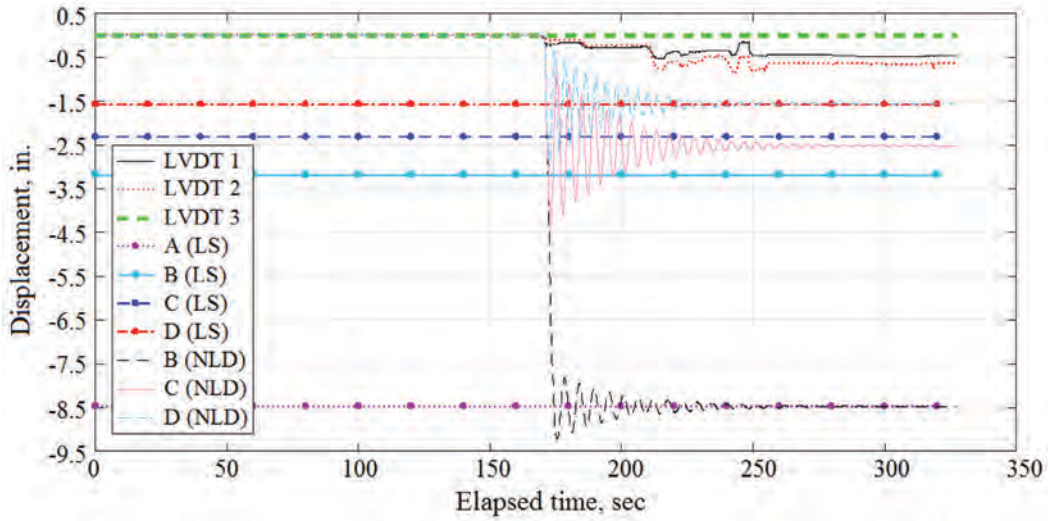

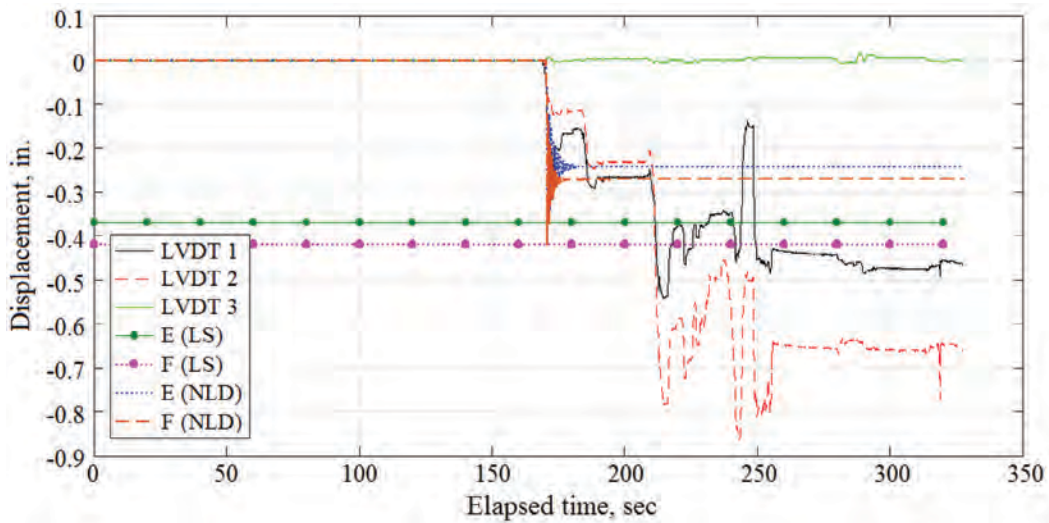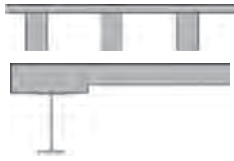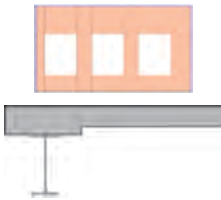*Fig. 11. Comparison of measured LVDT deflections to linear static (LS) and nonlinear dynamic (NLD) calculated deflections of models: E (composite beams and shell elements for infill walls); F (composite beams and tension-only strut elements for infill walls).*

Table 3. Calculated Deflections at Top of Column 27 with Different Modeling Assumptions						
Model	Model Assumptions	Model Details	Linear Static, in.	Change against Test Result	Nonlinear Dynamic, in.	Change against Test Result
A	Noncomposite beam, no slab in upper floors		8.46	1165%	Failed	N/A
B	Composite beams, no slab in upper floors		3.19	376%	8.47	1165%
C	Noncomposite beams, and ribbed slabs in upper floors		2.32	246%	2.52	276%
D	Composite beams, and ribbed slabs in upper floors		1.57	135%	1.56	133%
E	Composite beams and shell element for infill walls		0.37	−45%	0.24	−64%
F	Composite beams and tension-only strut elements for infill walls		0.42	−37%	0.27	−60%

Another nontypical detail in Haskett Hall was the ribbed slabs on the third and fourth floors. The ribbed slab consisted of multiple, small transverse concrete ribs below the slab. The ribbed slabs spanned between the steel beams. These slabs did not include an edge beam but were embedded into the façade at the end, as seen in Figure 5(c). This presented difficulty when developing the 2D model of the perimeter frame. Because there was not an actual beam to model, an assumption was made to include the portion of ribbed slab in the upper floors equivalent to the effective width in the composite beam-slab sections on the lower floors. The 2D perimeter frame was modeled using both composite and noncomposite beams. As shown in Table 3, four different assumptions were considered: noncomposite beams in the lower floors and no beams or slabs in the upper floors (model A), composite beams and no ribbed slabs in upper floors (model B), noncomposite beams in lower floors and

ribbed slabs in upper floors (model C), and composite beams and ribbed slabs in upper floors (model D). The maximum calculated deflections of models were compared with the experimental deflections in Table 3. The average experimental or measured maximum displacement on top of the removed column (column 27) was 0.67 in. The inclusion of the ribbed slab sections significantly influenced the overall behavior of the structure. The composite beam and ribbed slab model (model D) yielded the closest response to the experimental results for both the linear static analysis and nonlinear dynamic analysis (Table 3 and Figure 9).

Axial Load Distributions

The behavior of noncomposite and composite beam models were further compared through calculated axial load and moment distributions. Axial load distributions before and

Table 4. Calculated Change in Linear Static Compressive (–) Axial Forces in Columns in 2D Models								
	Test Column Pre-Removal, kips	Pre-Removal, kips		Post-Removal, kips		Change in Axial Force, kips		Total Change in Axial Force, kips	Increase in Axial Force, kips
Model	C27	C26	C38	C26	C38	C26	C38	C26 + C38	C26 + C38 over C27
A	145.5	126.1	77.8	192.2	160.1	66.1	82.3	148.4	2.0%
B	146.4	127.2	76.9	203.9	154.0	76.7	77.1	153.8	5.1%
C	146.8	123.2	76.4	192.2	154.9	69.0	78.5	147.5	0.5%
D	147.7	124.3	75.8	196.7	153.3	72.4	77.6	150.0	1.6%

after removal of the test column C27 for models B and C are shown in Figures 12 through 15. When compared with the calculated axial load in the test column (C27), the ribbed slab models (models C and D in Table 3) have the lowest total change in axial force in neighboring columns C26 and C38—that is, an increase of 0.3% and 1.7%, respectively, in Table 4. As the composite action increases, the total change in axial forces in columns C26 and C38 also increases compared with the test column C27. Specifically, in the non-composite beam model without ribbed slabs (model A), axial forces increase by 2.0%, while in the composite without ribbed slabs (model B), axial forces increase by 5.1%. Comparison of axial forces between the models with and without ribbed slabs show that in the models with ribbed slabs, larger axial forces are transferred to the neighboring columns (C26 and C38).

Moment Distributions

The maximum moments calculated from linear static analysis after removal of critical beams from the models. The unfactored demand-capacity ratios for plastic moments (DCR$_P$) are shown in Table 5. The unfactored load is the load combination with no live load and dead load factored by 1.0. DCR$_p$ is defined as the ratio of calculated maximum moment in a member to its plastic moment capacity, $M_p = F_yZ$, where F_y is yield strength and Z is the plastic section modulus. After column removal, the calculated maximum moments are larger in magnitude for models without ribbed slabs (models A and B) when compared with the models with ribbed slabs (models C and D). This shows that for both cases, the moments in beams in lower floors increase when the ribbed slabs are neglected and that the ribbed slab contributes to load redistribution. Comparison of calculated beam moments with flexural limits shows that the composite action generally led to a decrease in the unfactored DCR$_P$ by increasing the flexural strength. For example, the DCR$_P$ for models without ribbed slabs, beam B27-38 (Figure 2) had a DCR$_P$ of 2.46 and 0.90 in models A and B, respectively. For models with ribbed slabs, the DCR$_P$ for beam B27-38 is 0.88 and 0.49 in models C and D, respectively. In general, models with ribbed slabs have a lower DCR, showing that the ribbed slabs increase the overall flexural resistance of the frame. Moment diagrams before and after removing the test column C27 for model C are shown in Figures 16 and 17, respectively.

Fig. 12. Calculated axial load distribution for model B (with composite beams and no ribbed slabs) before the test column removal (under red cross).

Fig. 13. Calculated axial load distribution for model B (with composite beams and no ribbed slabs) after the test column removal.

Fig.14. Calculated axial load distribution for model C (with noncomposite beams and ribbed slabs) before the test column removal (under red cross).
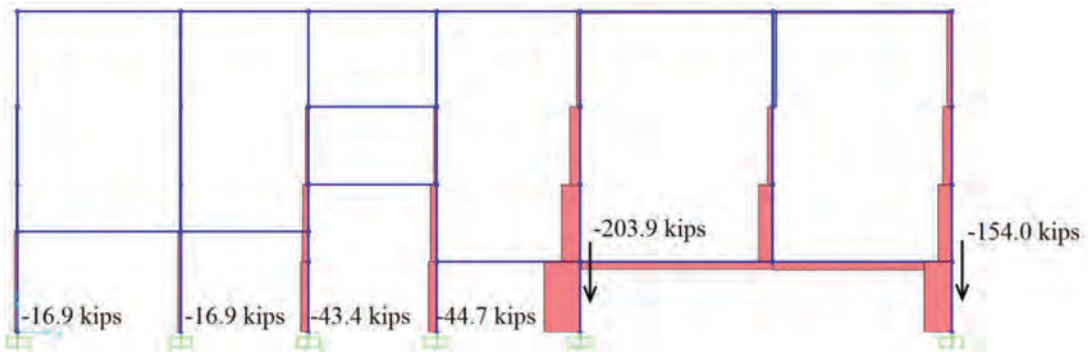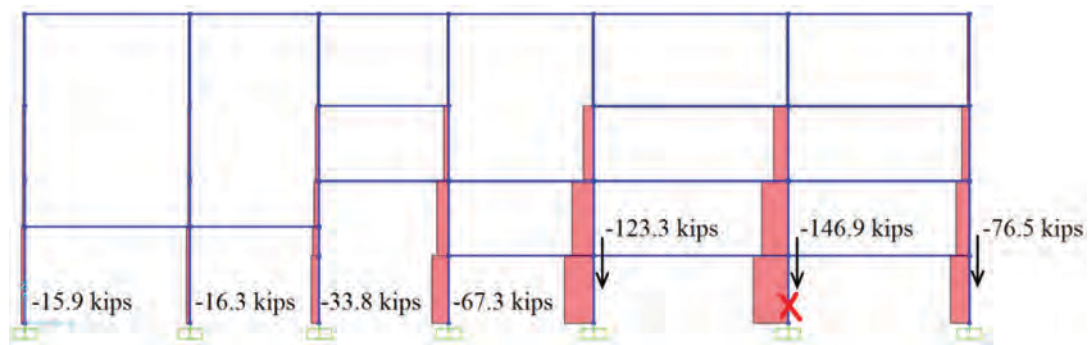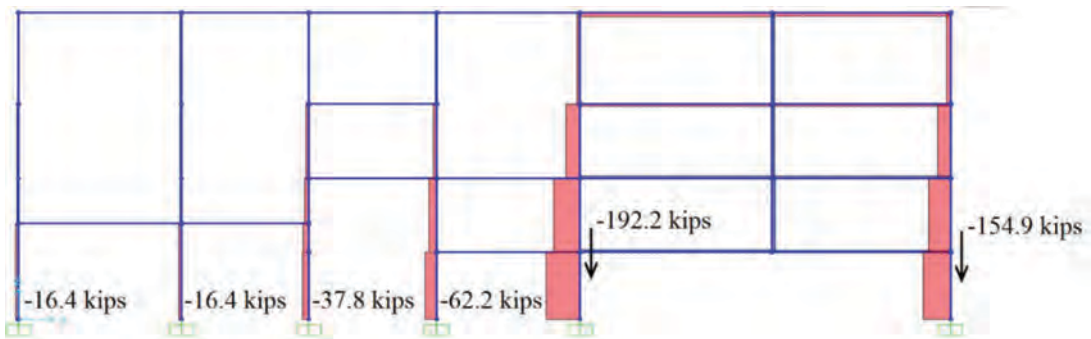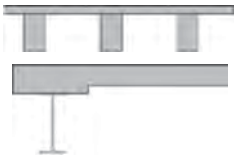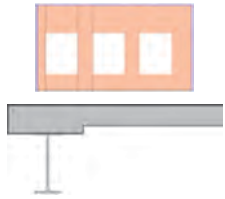

Fig. 15. Calculated axial load distribution for model C (with noncomposite beams and ribbed slabs) after the test column removal.

Table 5. Unfactored DCR of Connecting Beams (M_{max}/M_p)				
			DCR$_p$	
Model	Model Detail	Model Detail Figures	B (26-27)	B (27-38)
A	Noncomposite beam, no slab in upper floors		2.34	2.46
B	Composite beams, no slab in upper floors		0.95	0.90
C	Noncomposite beams, and ribbed slabs in upper floors		0.92	0.88
D	Composite beams, and ribbed slabs in upper floors		0.54	0.49
E	Composite beams and shell element for infill walls		0.21	0.13
F	Composite beams and compression-only strut elements for infill walls		0.38	0.39

INFILL WALL CONTRIBUTION

During the field experiment, the perimeter frame of the Haskett Hall was partially filled with unreinforced masonry walls at the second to fourth floors between the axis of 15 and 38 (Figure 1 and 2). The infill walls were directly attached to the structural beams and columns. Masonry walls have low tension strength but can provide additional stiffness in compression. As a result, it is expected that the infill walls will increase the progressive collapse resistance of Haskett Hall.

Infill walls had two types of window openings: 8.23 ft by 5.22 ft and 6.69 ft by 5.22 ft openings in the second and third stories (Figure 2). Figure 4 shows the cross-section cut through the window openings and indicates that only half of

the infill wall sits on the structural floor slabs. Therefore, in the SAP2000 model, only half of the original 12-in. thickness of the infill masonry wall was modeled. The default lower bound compressive strength of the masonry material, f'_m, was assumed to be 600 psi, as defined in ASCE 41-13 (2013). The expected strength, f_{me}, of 780 psi is used in this research (a factor of 1.3 is used to translate lower bound property to expected masonry property).

The second and third floor slabs modeled as ribbed slabs were simplified as a rectangular concrete beam of a 6.5-in. by 2-in. cross section. The infill walls were modeled using shell elements and equivalent strut elements. The shell elements with four nodes are used to model infill walls with window openings. In the equivalent strut method, the elastic in-plane stiffness of a solid unreinforced masonry wall

before cracking was modeled as an equivalent diagonal compression strut. For each strut, the elastic modulus was calculated from Equation 1 (Shames and Cozzarelli, 1997).

$$E_\theta = \cfrac{1}{\cfrac{1}{E_0}\cos^4\theta + \left(-\cfrac{2v_{0-90}}{E_0} + \cfrac{1}{G}\right)\cos^2\theta\sin^2\theta + \cfrac{1}{E_{90}}\sin^4\theta} \tag{1}$$

where θ is the angle whose tangent is the infill height-to-length aspect ratio; E_0 and E_{90} are the Young's modulus in the direction parallel and normal to the bed joints, respectively; v_{0-90} is the Poisson's ratio; and G is the shear modulus. According to TMS (2011), $E_{90} = 900 f'_{m-90}$, in which f'_{m-90} represents the expected compressive strength normal to the bed joint. $E_0 = 0.7E_{90}$, and $G = 0.4E_{90}$.

According to ASCE 41-13 (2013), the equivalent compression strut analogy shall be used to represent the elastic stiffness of the unreinforced masonry infill masonry wall of width a, given by Equation 2.

$$a = 0.175(\lambda_1 h_{col})^{-0.4} r_{inf} \tag{2}$$

in which

$$\lambda_1 = \left[\frac{E_\theta t_{inf}\sin 2\theta}{4E_{fe}I_{col}h_{inf}}\right]^{1/4} \tag{3}$$

where h_{col} is the column height between the centerlines of beams above and below the columns; r_{inf} and t_{inf} are the diagonal length of infill panel and thickness of infill panel, respectively; E_{fe} is the expected modulus of elasticity of the bare frame material; I_{col} is the moment of inertia of the column; h_{inf} is the height of infill panel; and E_θ represents the adjusted elastic modulus of the infill masonry material, which is calculated from Equation 1.

The infill walls are modeled by using two equivalent diagonal struts connected to the structural frame elements. ASCE 41-13 indicates that the tensile strength of masonry is only 10 psi for the fair condition, which is only one-sixtieth of its compressive strength, 600 psi under the same condition. For the poor stage of the unreinforced masonry, tensile strength is evaluated even as 0 psi. Due to the long-time use of Haskett Hall from its construction in 1925, the masonry
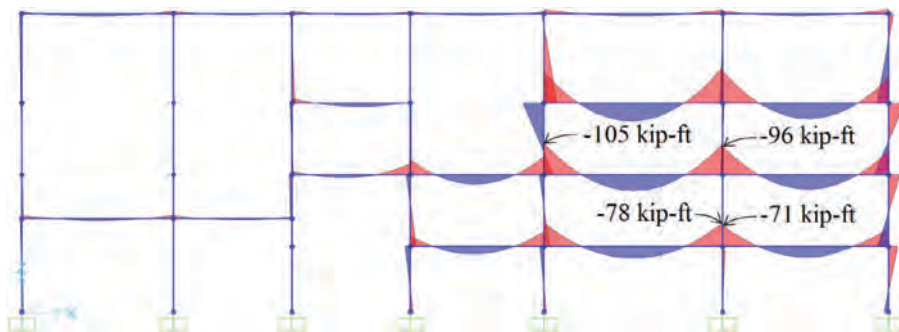
Fig. 16. Moment diagram for noncomposite with ribbed slab model (C) before test column (circled) removal. Values are for maximum moment demands in beams.
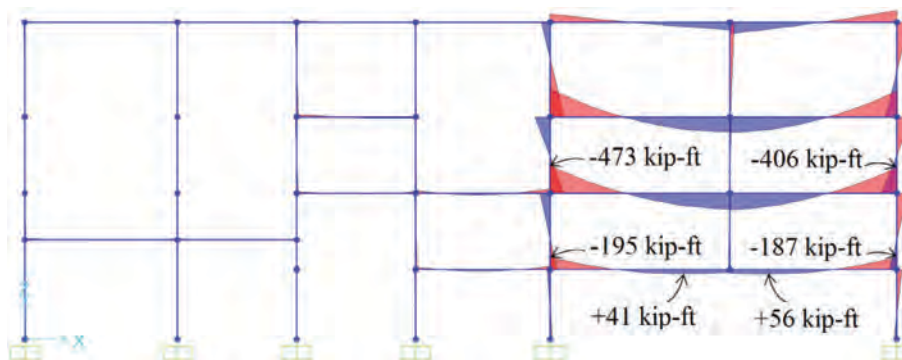
Fig. 17. Moment diagram for noncomposite with ribbed slab (C) model after test column removal. Values are for maximum moment demands in beams.

walls are likely to have potential material deficiencies and weakness between the mortar and red brick units. In this research, tensile strength of the unreinforced masonry is modeled as 0 psi. Based on this assumption, all struts subjected to tensile forces are supposed to be removed from the model. To achieve this goal in SAP2000 analysis, tension and compression stress distribution patterns of shell elements are obtained firstly as shown in Figure 18. The compression arrows are marked in warm colors (negative values), and tension arrows are marked in cold colors (positive values) on each shell element. A couple of arrows of each shell element are sustained tensile strengths and compression strengths, respectively, in the orthogonal direction. In the strut element method, the stress arrows can be roughly replaced by struts because the compressive and tensile strength are ultimately transferred to structural elements, and the struts are connected with structural components as well. By identifying the tension strength strut from the stress pattern diagram, one of the couple diagonal struts in the diagonal section is removed from the strut element model. The compression-only strut element model is developed and presented in Figure 19. All the struts were developed as frame elements with very large moment of inertia to act as truss members with axial deformation and strength only.

The shell element infill wall model is labeled as model E, as shown in Figure 18, and the compression-only strut element infill wall model is marked as model F (Figure 19). The linear static (LS) and nonlinear dynamic (NLD) analyses of infilled steel structure were performed and generated the 2D deflection data in Table 3. By comparison with the deflection data of all four bare steel structure models, the results of infilled steel structure models are much closer to the field

Fig. 18. Maximum stress distribution in model E with infill wall shell elements (and ribbed slabs in upper floors) after test column removal.

Fig. 19. Haskett House frame structure with compressive strut elements for representing infill walls.

test of Haskett Hall. Both LS and NLD analyses of model E and F yielded a maximum 64% difference ratio compared with experimental data, while the bare frame models A through D developed differences more than 100%, which indicates that the stiffness of masonry infill walls connected to the steel structural elements play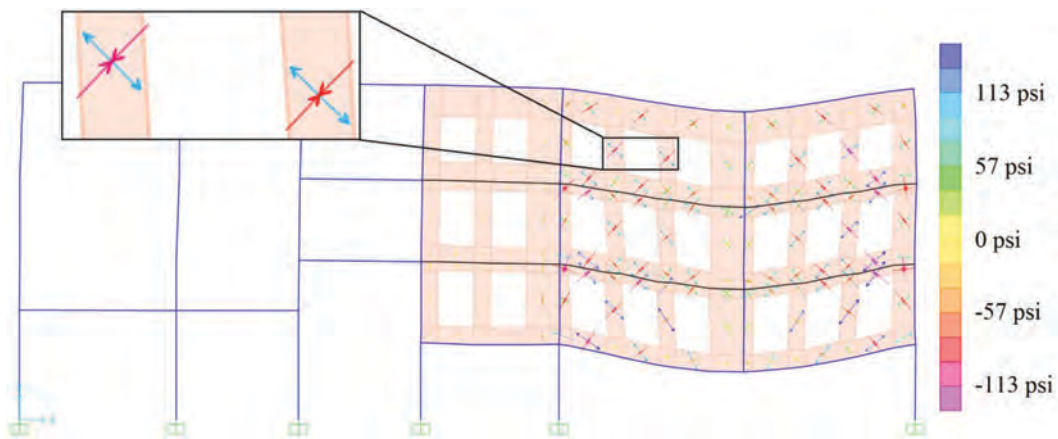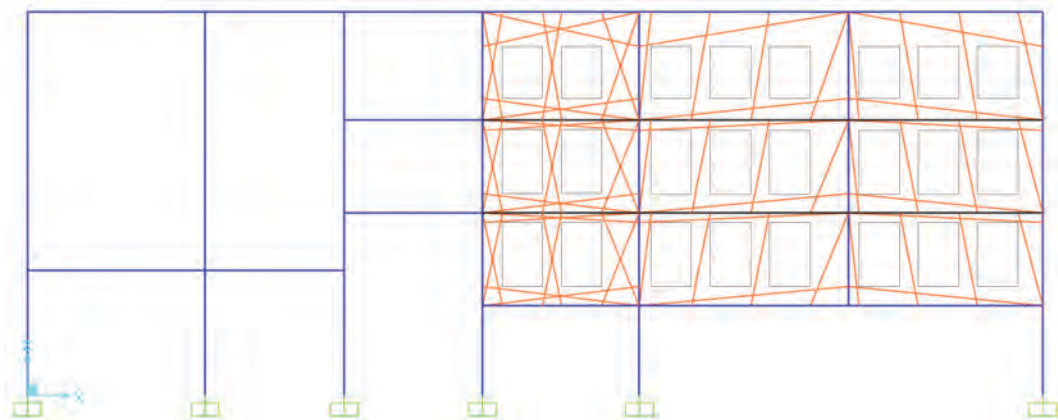s an important role in progressive collapse resistance. The infilled frame structure model was proved to decrease a minimum of 20.4% in DCR_P and increase the elastic stiffness 57.6% compared with bare frame structure model.

The calculated outcomes of two infill wall frame models E and F were compared with the measured LVDT deflections in Figure 10. It is clearly shown that the results from both the shell element model and the strut element model have higher agreement on the field test results than that of bare frame models A through D. The masonry infill walls can be simply modeled using equivalent strut element. Moreover, the strut element approach was better at modeling the unreinforced masonry wall because shell elements cannot identify and remove the tensile strength members. Figure 10 shows that both the linear static and nonlinear dynamic analyses results from strut element model F are closer to the field test data than that of shell element model E. More tensile strength contributions are made from shell elements; however, unreinforced masonry wall have little tension capacity.

Based on Figure 18, the stress distribution diagram of the infill walls is presented. It is observed that the large-magnitude stresses distribute on the infill walls of the bays in which the column was removed—that is, between axes 26 and 38. Lesser-magnitude stresses are distributed on the infill walls between axes 15 and 26. It indicates that only the infill walls within the bays where structural frames were removed develop compression and tension stresses. In general, the stiffness contribution of the masonry infill wall will be considered when large deformation appears in its attached structural frames. In Haskett Hall, large displacement was observed at column 27. The infill walls between C26 and C27 and C27 and C38 were under significant stresses and contributed in progressive collapse resistance. The DCR_P of the infill wall frame models are shown in Table 5. The maximum DCR_P of infill wall models is 0.39, which is smaller than the DCR_P of all the bare frame models. The comparison shows that the infill walls increase the flexural resistance of the steel structural frame and decrease the progressive collapse probability.

CONCLUSIONS

Haskett Hall was designed and completed in the 1920s, utilizing unique, as well as outdated, design methods. Full-scale experimental data were obtained during the removal of a first-story column. This unique field experiment on the perimeter frame of a steel building and numerical analyses have shown that the internal forces, including the axial load, on a first-story column is mainly transferred to the two neighboring columns without collapse. Due to lack of such full-scale building test data, the data measured in this research have been an invaluable addition to the state of knowledge on gravity collapse of actual buildings.

Two-dimensional linear static and nonlinear dynamic analysis results of four types of bare-frame models were compared with the data measured in the field. Analyzing the experimental and theoretical responses of the two-dimensional frame, the numerical calculation results exceeded the field data for linear static analysis and underestimated the results for nonlinear dynamic analysis. Including the ribbed slab sections appears to be critical to accurately capture the true behavior of the structure. The appropriate width of the ribbed slab to include on a two-dimensional analysis needs to be further researched. The infill wall model E shell element and the model F compression-only strut model improved the Hasket Hall structural modeling by yielding closer results to the field test data. By using the compression-strut element approach to model the unreinforced masonry infill wall, analysis results exhibited a high agreement with the field test results. It is concluded that the infill wall can improve the progressive collapse resistance performance by stiffening the structure and dissipating energy in smaller deformation. The infill walls within the column loss area can improve the stiffness of the structure as the large deformations appear.

ACKNOWLEDGMENTS

REFERENCES

Akah, A. (2015), *Experimental and Analytical Collapse Evaluation of an Existing Building*, M.S. Thesis, The Ohio State University, Columbus, OH.

AISC (2010), *Seismic Provisions for Structural Steel Buildings*, ANSI/AISC 341-10, American Institute of Steel Construction, Chicago, IL.

AISC (2011), *Steel Construction Manual*, 14th ed., American Institute of Steel Construction, Chicago, IL.

ASCE (2010), *Minimum Design Loads for Buildings and Other Structures*, ASCE 7-10, American Society of Civil Engineers, Reston, VA.

ASCE (2013), *Seismic Rehabilitation of Existing Buildings,* ASCE 41-13, American Society of Civil Engineers, Reston, VA.

Brockenbrough, R. (2003), *Rehabilitation and Retrofit Guide—A Reference for Historic Shapes and Specifications*, Design Guide 15, American Institute of Steel Construction, Chicago, IL.

DoD (2013), *Design of Buildings to Resist Progressive Collapse*, UFC 4-023-03, Department of Defense, Arlington, VA.

GSA (2013), *Progressive Collapse Analysis and Design Guidelines for New Federal Office Buildings and Major Modernization Projects*, General Services Administration, Washington, DC.

Li, K. (2017), *Collapse Assessment of Buildings by Wall Removal and Vision-Based Measurement Applications*, Ph.D. Dissertation, The Ohio State University, Columbus, OH.

SAP2000 (2011), *SAP 2000 Advanced Structural Analysis Program*, Version 15.1, Computers and Structures Inc., Berkeley, CA.

Shames, I.H. and Cozzarelli, F.A. (1997), *Elastic and Inelastic Stress Analysis*, Taylor & Francis Ltd, Philadelphia, PA.

Song, B., Giriunas, K. and Sezen, H. (2014), "Progressive Collapse Testing and Analysis of a Steel Frame Building," *Journal of Constructional Steel Research*, Vol. 94, pp. 76–83.

Song, B. and Sezen, H. (2013), "Experimental and Analytical Progressive Collapse Assessment of a Steel Frame Building," *Engineering Structures*, Vol. 56, pp. 664–672.

TMS (2011), *Building Code Requirement for Masonry Structures and Specification for Masonry Structures and Companion Commentaries*, The Masonry Society, Longmont, CO.

Nonlinear Behavior and Design of Mid- to High-Rise Diagrid Structures in Seismic Regions

ESMAEEL ASADI and HOJJAT ADELI

ABSTRACT

The aesthetics and structural advantages of the diagrid structural system have made it an attractive choice for many buildings across the world, including several notable high-rise building structures built in recent years. This paper presents an investigation of nonlinear behavior and design of mid- to high-rise steel diagrid structures. Weight, story drift, fundamental period, lateral stiffness, and sequence of plastic hinge formation in steel diagrids are studied and compared with corresponding moment-resisting frames and concentrically braced frames. To improve the nonlinear behavior and increase the collapse load capacity of diagrid structures in high seismic regions, practical design guidelines are proposed by using virtual work/energy diagrams and by performing nonlinear static analysis. So far, the diagrid system has been used mostly in the design of tall buildings in the range of 20 to 100 stories. A conclusion of this research is that the diagrid system can also be an efficient and economical structural system for mid-rise buildings in the 8- to 15-story range.

Keywords: diagrid, mid-rise, high-rise, steel, seismic.

INTRODUCTION

In recent years, there have been a number of attempts to augment the three main and commonly used structural systems for resisting the horizontal loads due to wind and earthquake loading—moment-resisting frames, braced frames, and shear walls—with innovative systems. Reviews of innovative high-rise building structures with an eye on sustainability are presented by Wang and Adeli (2014) and Rafiei and Adeli (2016). Among them is the diagrid system known to be a descendant of braced frames. While most engineers attempted to hide braced frames within the interior or façade of buildings, a few made it an integral part of the building facade. An early and notable example is the 100-story John Hancock Building in Chicago built in the late 1960s, where large braced frames were used on the exterior perimeter of the building not only to withstand the lateral loads, but also to improve the building's outer face aesthetic (Moon et al., 2007).

The word *diagrid* is a combination of *diagonal* and *grid* used for the first time by pioneering Russian architect Vladimir Shukhov for the world's first hyperboloid structure built in 1896 (Boake, 2014). The first application of diagrid in buildings appears to be the IBM building (now called the United Steelworkers Building) in Pittsburgh built in 1965 (Moon et al., 2007). Early researchers were concerned mostly with the analysis of diagonal grids in general, not specifically for tall buildings. For example, Subaramanian and Subaramanian (1970) presented partial difference equations for the slope-deflection method to find in-plane deflection of a simple uniform rectangular diagrid. Grigorian and Kashani (1976) proposed formulas to find the collapse load of rectangular diagonal grids and suggested methods for their analysis and design.

The aesthetics and structural advantages of diagrid have made it an attractive choice for many buildings across the world, such as the 42-story Hearst Building in New York, the 41-story Swiss Re Building in London (Ali and Moon, 2007), and the 54-story CCTV headquarters in Beijing. The major difference between diagrids and braced frames is the omission of vertical members, or columns, from the exterior structure. In diagrids, lateral forces due to wind or earthquake are transferred primarily via axial forces in diagonal members; bending moment makes a small contribution to the design of the diagonal section.

In the past decade, extensive research has been done on the design and diagonal configurations of diagrids in tall buildings. Moon et al. (2007) and Moon (2008) present a stiffness-based approach for the preliminary design of each diagonal member. They also study the effect of the angle of the diagonals with the horizontal axis on the overall stiffness of the frame. Zhang et al. (2010) propose gradually varying angles for diagrids and report the most efficient varying angle for diagrids in terms of the aspect (height-to-width) ratio. Kim and Lee (2012) study the nonlinear static and time-history dynamic behavior of diagrids and recommend

Esmaeel Asadi, Department of Civil Engineering, Case Western Reserve University, Cleveland, OH. Email: exa187@case.edu

Hojjat Adeli, Department of Civil, Environmental, and Geodetic Engineering, The Ohio State University, Columbus, OH. Email: adeli.1@osu.edu (corresponding)

a diagonal angle between 60° and 70° as the most advantageous angle for most diagrid structures.

Kim and Lee (2010) report progressive collapse resistance of tubular diagrid high-rise building structures as generally high, while conventional tubular structures show a slightly larger resistance. They highlight the importance of corner diagonals against progressive collapse. A review of diagrid structures as a sustainable and efficient structural system is presented in a recent article by Asadi and Adeli (2017).

The diagonal-angle, the angle of diagrid members with the horizontal line in practice, is determined based on architectural and aesthetic requirements, story heights, span length, and lateral load intensity and distribution. Several parametric studies have been conducted on the optimal diagonal angle, which are discussed in Asadi and Adeli (2017).

This research aims to encourage structural designers and stakeholders to look into an innovative structural system with unique properties for their steel structures. The goal of this research is to assess diagrid characteristics and behavior in mid- to high-rise buildings and explore practical solutions for their design shortcomings. Structural and economic aspects of typical diagrids are compared with moment-resisting frames (MRF) and concentrically braced frames (CBF) using linear analysis to study their story drift and modal response and nonlinear analysis to evaluate their performance and failure mechanism. Design guidelines are presented for the seismic design of steel diagrid structures in high seismic regions, which can be used in future AISC and ASCE seismic provisions for the diagrid system.

EXAMPLE STRUCTURES

Model Specifications

Diagrids provide considerable stiffness against lateral loads due to wind and earthquake loads and are attractive for tall buildings (Ali and Moon, 2007). Providing appropriate lateral stiffness is also important for mid-rise buildings in seismic regions—especially for those with large aspect ratios. Therefore, in this research, inelastic seismic behavior of mid- to high-rise steel diagrid buildings is studied. Three groups of office buildings with similar plans are considered with the number of stories equal to 8, 15 [Figure 1(a)], and 30 [Figure 1(b)]. The first two groups represent mid-rise buildings. The third group has a similar elevation but a different plan shown in Figure 1(b). The elevation and perspective view of the 8-story structure are shown in Figures 2(a) and 2(b), respectively. Each structure of the first and second groups consists of a core with four columns at its corners and two outer spans on either side connecting the diagrids to the core [Figure 1(a)]. The third group has a set of 25 central columns arranged on a larger square plan [Figure 1(b)]. A story height of 11.5 ft (3.5 m) is used for all models similar to previous studies (Zhang et al., 2010; Kim and Lee, 2012). Three diagrid patterns with diagonal angles of approximately 45°, 63° and 72° with the horizontal are studied. The structures are labeled by using the number of stories and their diagonal angle. For instance, structure 15-63 refers to a 15-story diagrid structure with a diagonal angle of 63°, as shown in Figure 2(a).
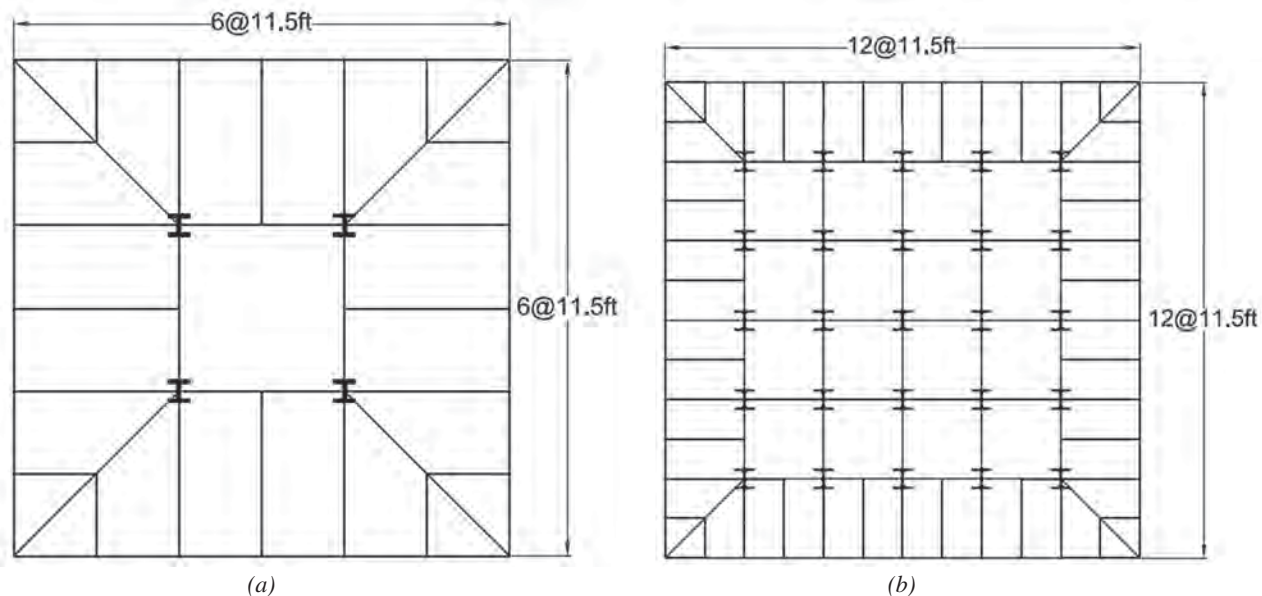

(a)   *(b)*

Fig. 1. Typical floor plan for (a) 8- and 15-story buildings and (b) 30-story buildings.

Design of Structures

All models are designed in accordance with the 2016 AISC *Specification* (AISC, 2016b) and the 14th Edition AISC *Steel Construction Manual* (AISC, 2011) utilizing the Load and Resistance Factor Design (LRFD) approach using the software package SAP2000. The response modification, *R*, factor is assumed to be 3.0, similar to previous studies (Kim and Lee, 2010, 2012; Kim and Kong, 2013). This conservative assumption does not mean that the *R* factor of steel diagrids is equal to 3.0. Note that ASCE/SEI 7 (2010) does not permit structural systems with $R \leq 3.0$ to be constructed in a site with Seismic Design Category D to F. The AISC *Seismic Provisions* (AISC, 2016a) are not used for the design of diagrid frames because they are not recognized by the current design code, but the amplified seismic load combinations are considered for the internal columns. The following two load combinations with overstrength factors from ASCE/SEI 7, Section 12.4.3.2 are included in design load combinations for the columns:

$$(1.2 + 0.2S_{DS})D + \Omega_o Q_E + L \qquad (1)$$

$$(0.9 - 0.2S_{DS})D + \Omega_o Q_E \qquad (2)$$

where *D*, *L*, Q_E, Ω_o and S_{DS} are the effects of dead and live load and horizontal seismic forces, overstrength factor assumed equal to 3.0, and design spectral response acceleration parameter at short periods, respectively. MRF and CBF models are checked according to AISC *Seismic Provisions* Section E2 (Intermediate Moment Frames) and F2 (Special Concentrically Braced Frames) (AISC, 2016a). SAP2000

has been used by a number of other diagrid system researchers in recent years in a similar fashion (Moon et al., 2007; Kim et al., 2010; Kim and Lee, 2012; Kim and Kong, 2013).

Standard W-sections are used for all diagonals, beams and columns. Following practical considerations, the same diagonals and column sections are used for every three stories across the width. Diagonal connections are moment-resisting connections, and the connections of the columns of MRF and CBF and diagonals of diagrids to the foundation are considered to be fixed except for the central columns, where a hinged condition is chosen so that those columns do not carry any unintended lateral loaded.

Diagonal members are designed to withstand both lateral and gravity loads, while the core columns are designed to carry dead and live loads only. All design loads are calculated per ASCE/SEI 7 for an office building located in southern California, near Los Angeles city, with S_s (spectral response acceleration at 0.2 sec) and S_1 (spectral response acceleration at 1 sec) of 2.461g and 1.127g, respectively. Where permitted by ASCE/SEI 7, the equivalent lateral force (ELF) procedure is used as the method of seismic analysis. In other cases, the modal response spectrum analysis is also carried out to find the critical base shear as required. For wind loads, Exposure Category C and wind speed of 110 mph are used according to the location of the structures. Floors are reinforced concrete slabs with a thickness of 6 in. A total uniform dead load of 85 psf plus a live load of 50 psf are applied on all floors except the roof. For the roof, the dead load is the same but the live load is reduced to 20 psf. The ASCE/SEI 7 requirements for story drift are checked during the design process.
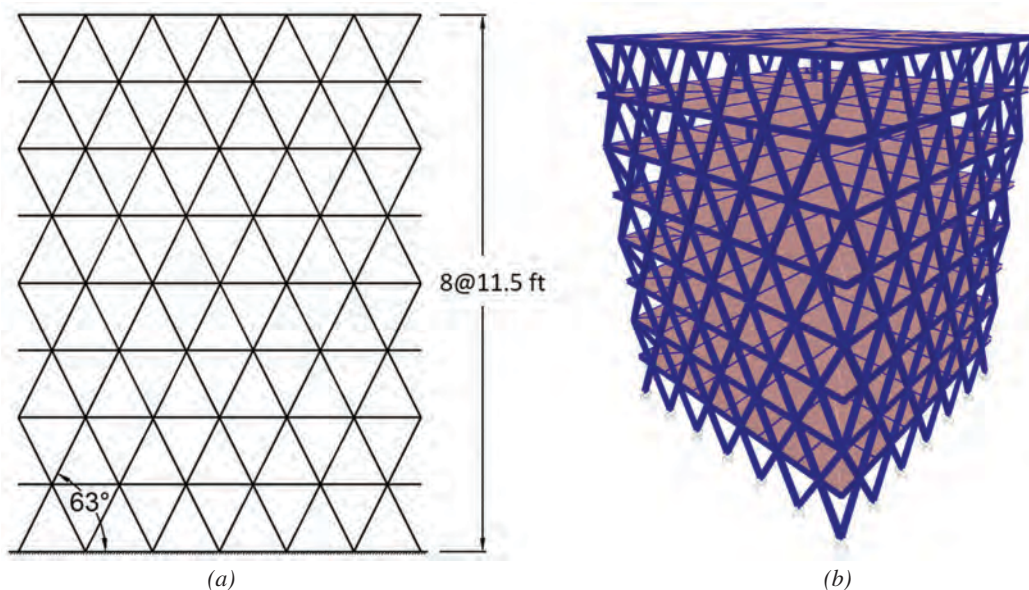

(a)   *(b)*

Fig. 2. The 8-63 model (a) elevation and (b) perspective view.

ELASTIC AND INELASTIC
BEHAVIOR OF DIAGRIDS

In this section, the elastic internal force distribution and nonlinear behavior and sequence of plastic hinge formation are studied for a typical mid-rise building, the 8-45 model.

Elastic Internal Force Distribution

In general, diagonals in diagrid structures undergo large axial forces and comparatively small bending moments under lateral loading, which can be attributed to their inclined position. As such, the axial force is the primary internal force in the design of diagonal members. Figure 3 shows the elastic distribution of axial forces in the diagonals of the 8-45 model due to the earthquake load. In general, axial forces in the diagonals under lateral loading increase from the top story to the first story. Depending on the direction of the lateral load, about half of the diagonals undergo tension and the other half compression. The axial force also increases from the middle diagonals to the corner ones (Figure 3), which indicates the critical role of corner diagonals in diagrids. To take this nonlinear variation of stress between corner and middle members, known as a shear lag effect, one can use smaller sections for middle diagonals. Shear lag is a nonuniform, nonlinear distribution of the internal forces

across the side of a tube-shaped structure or structural member. The result is large internal forces in corner members compared with the middle ones.

At each joint, four diagonal members are connected in two different inclined directions (each two are aligned). Corner joints experience either a large compression or a large tension force in one direction/alignment, only while middle joints undergo both compression and tension forces but in smaller magnitudes in two different directions/alignments. As such, this varied load bearing condition of diagrid connections that depends on their locations has a major effect on their connection design. This finding has two implications. First, researchersperforming experiments on connections in diagrids (Kim et al., 2010) need to take the load variation into consideration. Second, the current design preference of fabricators to use as many identical connections as possible needs to be revisited.

Maximum nonfactored diagonal axial forces in the first story due to gravity and earthquake loads are found to be 133 kips and 745 kips, respectively, while the maximum bending moments due to gravity and earthquake loads are relatively small, 14 kip-ft and 67 kip-ft, respectively. Similar differences are noted for diagonals in other stories showing the dominance of axial force in the diagonals compared with bending moment. Consequently, in preliminary design,
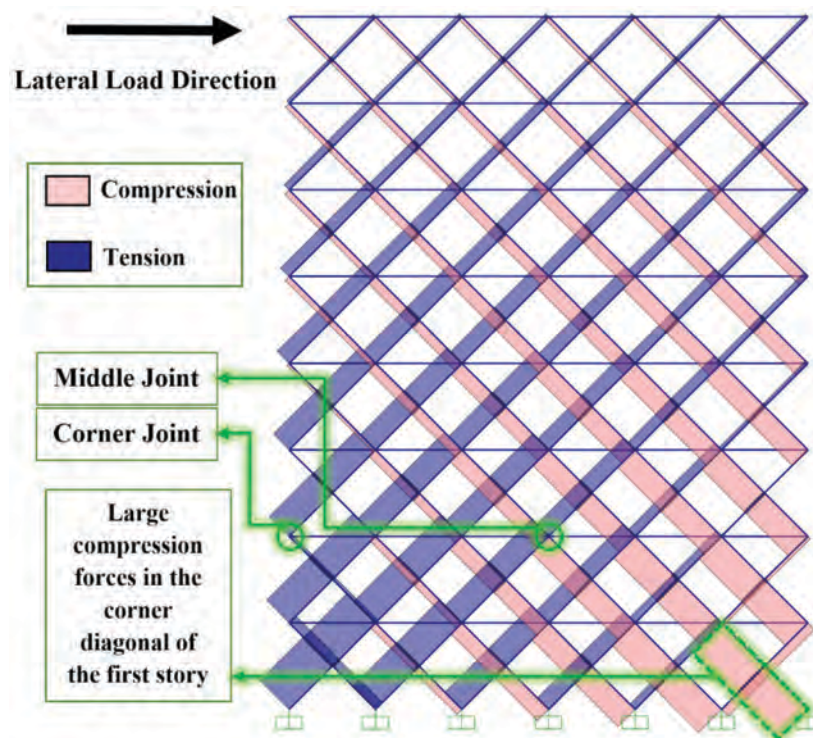

Fig. 3. Axial force in diagonals of 8-45 model due to earthquake load.

Table 1. Modeling Parameters and Acceptance Criteria for Nonlinear Analysis for Diagonal Members of Steel Diagrid Frame Adapted from FEMA-440 (2005) and ASCE/SEI 41-13 (2014)						
	Modeling Parameters			Acceptance Criteria		
Component	a	b	c	IO	LS	CP
W- or I-shaped section	$0.5\Delta_c$	$8\Delta_c$	0.2	$0.5\Delta_c$	$5\Delta_c$	$7\Delta_c$

the diagonals may be designed as axial-force compression members neglecting the small, existing, axial force-bending moment interaction.

The first two vibration modes of the 8-45 diagrid are translational modes with a fundamental period of 0.41 sec obtained using the free vibrations theory and direct eigenvalue method, while the approximate fundamental period equation $T_a = C_t h_n^x$ of ASCE/SEI 7 (2010) yields a larger value of 0.59 sec. This may lead to a nonconservative initial design. Research is needed to create relatively accurate approximate equations for estimating the fundamental period of diagrid structures similar to those developed for MRF (Young and Adeli, 2014a), CBF (Young and Adeli, 2014b), and EBF (Young and Adeli, 2016).

Nonlinear Behavior

In practice, the great majority of structures are designed based on the elastic analysis (Shan et al., 2016; Oh et al., 2017; Kim et al., 2017). During major earthquakes, however, structural members often experience nonlinear inelastic behavior (Adeli et al., 1978; Jiang and Adeli, 2005; Yang et al., 2017). To investigate nonlinear characteristics of diagrids, a static nonlinear analysis is conducted for all models according to the provisions of FEMA-356 (2000) and FEMA-440 (2005) and examples provided in FEMA P-751 (2012). As required by FEMA provisions, lateral loads are applied after the full exertion of gravity loads. They are increased proportionately until a sufficient number of plastic hinges (PH) or fully yielded axial force members result in a failure mechanism. As discussed, diagonals carry mostly axial loads, whereas beams have a large bending moment and columns carry a combination of axial force and bending moment. To model these different types of behavior, three types of PH are defined: axial (P) for diagonals, flexural (M) for beams, and interacting (PMM) for columns (CSI, 2011). The concentrated PH are assigned to mid-length of diagonals, and ends of beams and columns as suggested by FEMA (2000). The scale factors for yield rotation, θ_y, are modeled per Equations 5-1 through 5-4 of FEMA-356 for each PH.

For each member of the structure, three levels of performance are defined as follows: immediate occupancy (IO) after the earthquake, where buildings *"are expected to sustain minimal or no damage to their structural elements and*

only minor damage to their nonstructural components"; life safety (LS), where buildings *"may experience extensive damage to structural and nonstructural components"*; and collapse prevention (CP), where buildings *"may pose a significant hazard to life safety resulting from failure of nonstructural components"* as defined in the general force-deformation curve shown in Figure 4 for primary elements (FEMA, 2000, 2005; ASCE, 2014).

To capture the nonlinear behavior of diagonals at each performance level, the recommended modeling parameters and criteria of FEMA-440 and ASCE/SEI 41-13 (2014) for concentrically braced frames, listed in Table 1, are adopted in this investigation. The parameters *a*, *b*, and *c*, shown in Figure 4, are calculated based on FEMA-440, Tables 5-6 and 5-7, and are used for modeling the force-deformation relationship of the PH. The parameter Δ_c represents the axial deformation at the expected buckling load. This method captures global buckling but not local buckling explicitly. Due to large axial forces in the diagonals, a main factor in the load capacity and performance of each diagonal is the cross-sectional area. The required slenderness for the diagonal section is typically low, well below the slender limit between elastic and inelastic buckling ($KL/r = 4.71\sqrt{E/F_y}$ for grade 50 steel). Hence, noncompact sections are intentionally avoided in the design process to limit partial or global buckling while preserving the desirable performance of the system.

In addition, for nonlinear pushover analysis, FEMA-356 provisions require checking at least two different vertical load distributions. In this research, three different vertical load distributions are considered for the entire structure: uniform distribution, the distribution provided by the ELF method of ASCE/SEI 7 (ASCE, 2010), and modal shape distribution considering only the first two modes of vibrations. Out of the three, the most critical pattern is chosen for further study. The center of mass at the roof is used as the monitoring point for the displacement-control pushover analysis. The Newton-Raphson method is used for nonlinear analysis, and the convergence tolerance and maximum number of iterations are adjusted to achieve proper convergence (FEMA, 2000; CSI, 2011).

Figure 5(a) shows the results of the pushover analysis for the 8-45 model. Figure 5(b) shows the lateral stiffness of the structure at the roof level versus the lateral displacement at

the top of the 8-45 model. It is observed that the structure shows the smallest load capacity and the lowest elastic stiffness for the case of mode shape vertical force distribution pattern. Thus, the mode shape distribution is considered the most critical and is selected for further discussion on this model. The same procedure is adopted for other example structures.

The design base shear obtained using the ELF method of ASCE/SEI 7 for 8-45 is approximately 5,845 kips [shown in Figure 5(a) with a dash-dotted line], while at the formation of the first PH [shown in Figure 5(a) with a solid circle], the base shear is 8,318 kips. A part of this 42% overstrength can be attributed to the assumed R factor in the design procedure. Figure 5(b) represents the slope of the pushover curve in Figure 5(a). This slope decreases substantially after the formation of the first PH. The structure experiences its ultimate load capacity of 17,310 kips at the CP performance level, which is approximately three times greater than the design base shear.

This diagrid structure remains elastic up to a very low drift ratio of 0.2%, approximately corresponding to the lateral displacement of 2.6 in. in Figure 5(b). From this point on, development of plasticity in the diagonals leads to a sharp decrease in the lateral stiffness in a nearly step-wise fashion after the formation of each PH. This can be recognized in the pushover curve [Figure 5(a)], where the slope of the pushover curve declines gradually until it reaches the ultimate load. As PH are formed or global buckling occurs in several diagonals, the lateral stiffness of the structure is reduced from the yield load [initiation of yielding represented by the horizontal plateau in Figure 5(b)] to the LS performance level, a reduction of 86%. The load capacity of the structure increases up to the ultimate load, beyond which its load capacity drops suddenly, indicating the formation of a failure mechanism. At this point, the structure undergoes a drift ratio of 0.8%, which is, as will be discussed later, much smaller than more ductile structural systems, such as MRF.

Figure 6(a) shows the location of the first PH for each performance level. The first PH of LS level forms in the compression diagonal located at the corner of the first story. This is mostly due to large cumulative axial forces in the corner diagonals. The nonlinear analysis also confirms that corner diagonals undertake the largest amount of axial force compared to other diagonals. In general, diagrid structures consist of a number of diagrid planes on the exterior of the building, and each plane behaves similar to a plate or shell (in the case of curved planes) under lateral loads. In this case, the corner diagonals are at the interface of two diagrid planes and take loads from both. In the case of two perpendicular diagrid frames, one frame, called the flange diagrid frame, is parallel to the direction of lateral force and the other, called the web diagrid plane, is perpendicular to the former. As shown in Figure 3, diagonals in a flange diagrid frame undergo both compression and tension but in the web frame, they are either in compression or tension, depending on the direction of lateral load. Accordingly, the corner diagonals, at the interface of web and flange frames, usually receive large cumulative compression and tension forces from both frames, making them the critical members in diagrids.

When LS PH develop in several compression diagonals, the first IO PH is formed in the corner tension diagonals of the first story (compression members buckle). As the structure is pushed to a larger amount of lateral load, PH spread to other compression diagonals in the first and fourth story. Eventually, plasticity is spread to most diagonal members, and the structure turns into a failure mechanism in the form of a soft story mechanism [fourth story in Figure 6(b)]. At this step of the analysis, plasticity is developed over a good portion of the structure, indicating the ability of a diagrid structure to develop a good number of PH before failure.

In order to explain why more PH form in the fourth story and at a higher performance level than the first three stories, different factors were studied. It was found that grouping of
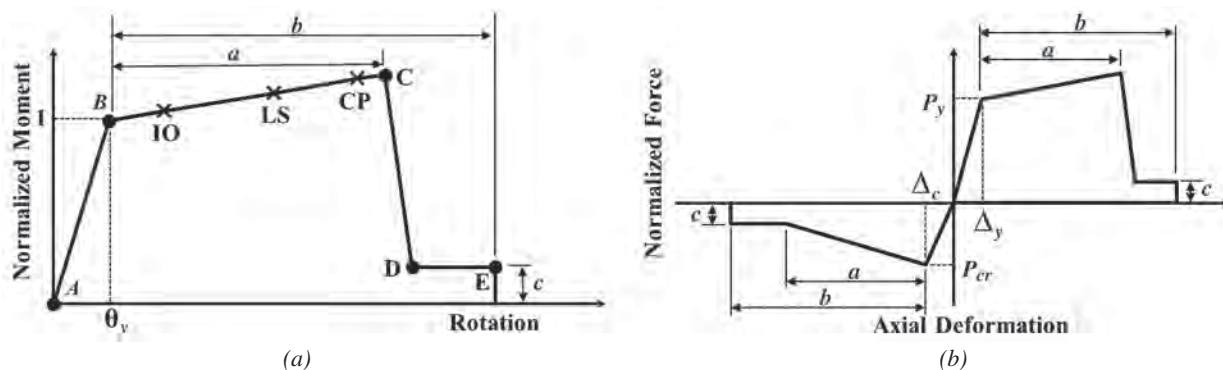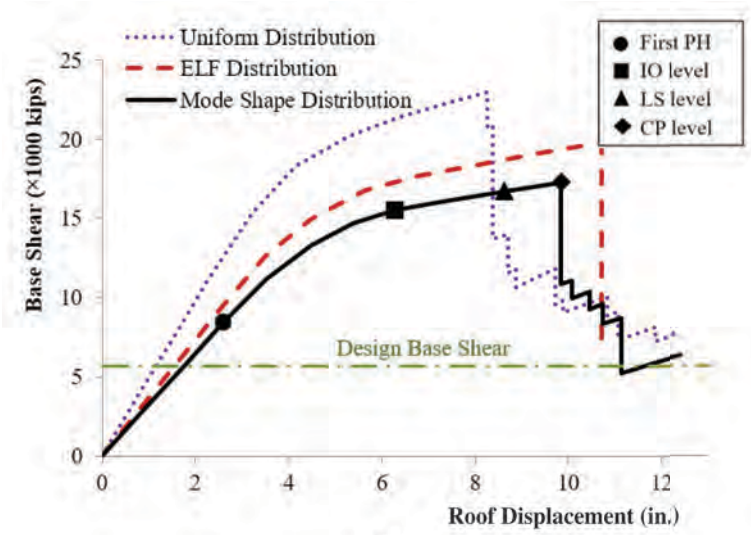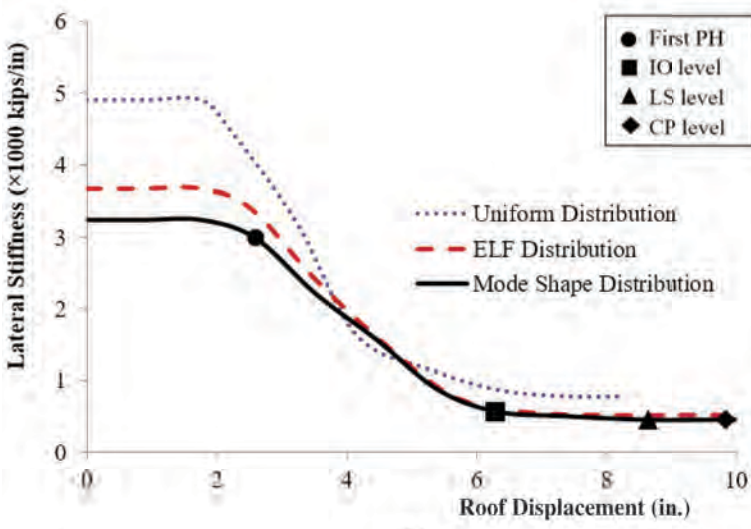

(a)   *(b)*

Fig. 4. General member force-deformation relationship and performance levels and parameters adopted from FEMA-440 (2005): (a) flexural elements; (b) diagonals.

Fig. 5. (a) Lateral load (pushover) and (b) lateral stiffness versus displacement curve for the 8-45 model.

the members in the design process has the largest influence. Because smaller diagonals are used in the fourth story based on member grouping described earlier, there is a reduction of story stiffness at the fourth story, making it more susceptible to the formation of PH than the story below. It should be noted that ASCE/SEI 7 requirements about irregularity in stiffness or strength were checked and satisfied in the design process.

COMPARISON OF DIAGRIDS WITH MRF AND CBF

General

In this section, the influence of the diagonal angle on the behavior of diagrid structures is studied for 8-story, 15-story, and 30-story models using three different angles of inclination: 45°, 63° and 72°. Further, the 8-story and 15-story diagrid structures are compared with two other commonly used structural systems: MRF and CBF. MRF are well known for their considerable ductility and are chosen to assess the ductility of the diagrids. CBF have inclined members similar to diagrids, but in contrast to diagrids, they also have vertical columns. The plan, elevation loading, and design procedures of MRF and CBF are kept the same as the diagrid. For this comparison, the gravity loads (dead and live load) and the seismic lateral loads are applied to the structure as explained earlier. Figures 7(a) and (b) show the perspective views of the 8-story CBF and MRF models, respectively. In these models, the perimeter diagrid frames are replaced with either MRF or CBF. For CBF, a number

of different bracing patterns were examined, and bracing of four bays on each side was found to be the proper choice for carrying the described design lateral loads. The perimeter frames are the primary lateral load-bearing systems in these structures, and central columns absorb only a small portion of the lateral load, similar to the diagrid structures. Table 2 lists the structural properties of the models, including the weight of the structure, fundamental period, maximum story drift, mean story drift, maximum roof displacement, and elastic lateral stiffness at the roof level.

Weight of the Structure

The weight of a steel frame is one of the important factors in choosing an appropriate structural system to carry both vertical and lateral loads. The weight per meter squared for different models is presented in Table 2 and as a bar chart in Figure 8. It is observed that the inclination of the diagonals has a significant impact on the weight of the structure, especially in mid-rise structures in the range of 8 to 15 stories. For the 8-story diagrids, a diagonal angle of inclination of 45° results in the lightest structure. This structure is lighter than the corresponding MRF and CBF by 16% and 7%, respectively. This is primarily due to large columns required in MRF and CBF to carry large lateral loads. The structural efficiency of diagrids may be attributed to their dual function in carrying the gravity and lateral loads. Further, both lateral and gravity loads produce mostly an axial force in the diagonals with little bending moment, which means near-uniform distribution of stresses in the cross-section in contrast to uneven stress distribution in members subjected to bending, a more efficient way to carry a load, as long as
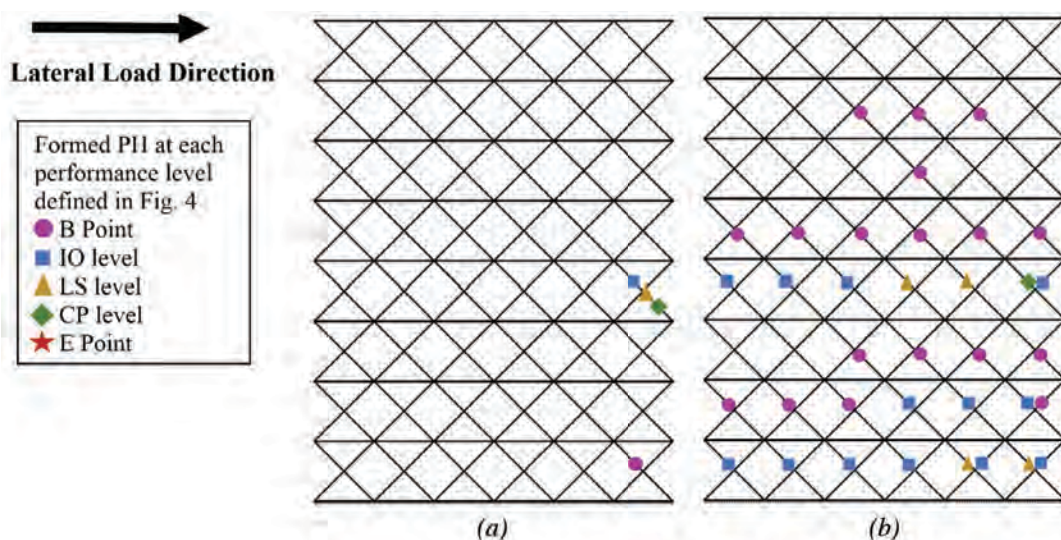
Fig. 6. (a) Location of the first hinge at each performance level; (b) location of PHs at formation of a soft story failure mechanism in the 8-45 structure.

Table 2. Properties of 8-, 15-, and 30-Story Models												
Property	8-MRF	8-CBF	15-MRF	15-CBF	8-45	8-63	8-72	15-45	15-63	15-72	30-45	30-63	30-72
Weight of the structure (lb/ft^2)	23.8	21.9	31.2	39.1	20.5	23.2	33.2	33.6	24.4	52.0	44.3	42.2	46.6
Fundamental period (sec)	1.51	0.66	2.50	1.06	0.41	0.37	0.40	0.77	0.73	0.57	1.39	1.26	1.29
Fundamental period using ASCE/SEI 7, $T_a = C_t h_n^x$ (sec)	1.04	0.59	1.72	0.95	0.59	0.59	0.59	0.95	0.95	0.95	1.60	1.60	1.60
Maximum story drift (%)	0.72	0.32	0.75	0.45	0.25	0.21	0.40	0.54	0.46	0.39	0.62	0.29	0.58
Mean story drift (%)	0.65	0.26	0.62	0.37	0.21	0.17	0.23	0.38	0.35	0.24	0.40	0.19	0.33
Maximum roof displacement (in.)	7.16	2.92	12.9	7.63	2.31	1.85	2.50	7.91	7.24	4.86	16.6	7.81	13.6
Elastic lateral stiffness at roof (kip/in.)	409	1748	253	1144	3239	4500	3604	1435	1747	3688	3862	5456	5681

(a)   *(b)*
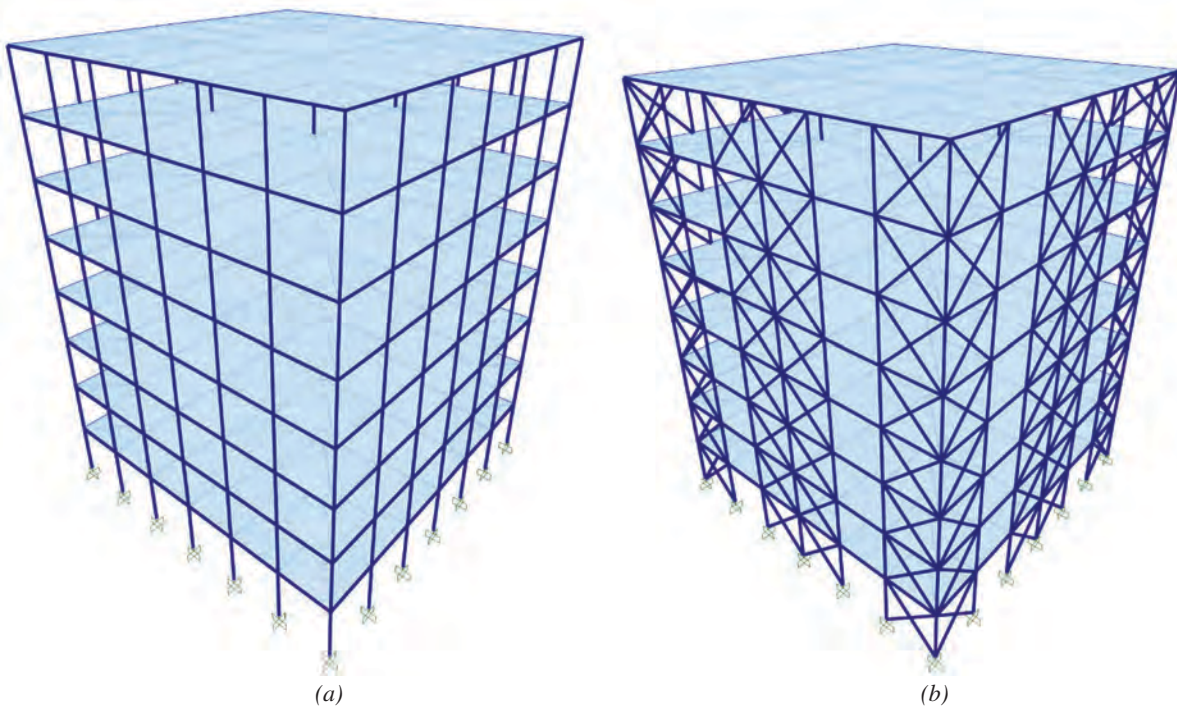
Fig. 7. Perspective view of (a) 8-story MRF; (b) 8-story CBF.

buckling is avoided. As such, it may be concluded that for a mid-rise structure such as the 8-story frames, a diagrid results in a lighter structure compared with MRF and CBF if an appropriate diagonal angle is used. This research complements prior research that pointed to the structural efficiency of diagrids for design of tall buildings in the range of 36 to 100 stories (Moon, 2008; Kim and Lee, 2012).

In the case of the 8-63 and 8-72 models, the diagonal angle has a considerable effect on the total structural weight such that they are 12% and 63% heavier than 8-45, respectively. The following relation exists between the jth lateral load, $F_{L,j}$, and the axial force in the ith diagonal, $F_{d,i}$, neglecting the rest of the structure (Figure 9):

$$F_{L,j} = 2F_{d,i} \cos\theta \tag{3}$$

This equation shows the axial force in the diagonal increases with an increase in the angle θ.

On the other hand, for the 15-story models, the 15-63 model is the lightest and is approximately 20% lighter than 15-45. The 15-63 model is also lighter than both 15-MRF and 15-CBF, indicating a possible reduction of structural weight by using the diagrid structural system. Also, the 15-72 model is substantially heavier than the 15-45 model. The comparative pattern for the 30-story models is similar to 15-story models but on a much smaller scale, where the 30-63 is lighter than the 30-45 and 30-72 models by 4.8% and 10.2%, respectively. The optimal diagonal angle for the minimum weight increases with the height of the structure up to a certain angle, θ. Previous studies reported an optimum diagonal angle in the range of 60° to 70° for 36-story diagrids (Kim and Lee, 2012) and in the range of 65° to 75° for 60-story diagrids having an aspect ratio of about 7 (Moon et al., 2007). The difference in the optimum angle for mid-rise structures, such as the 8-story frames, versus taller structures, such as the 15- and 30-story diagrids, can be explained through the effect of the overturning moment on diagonal axial forces. In taller frames, the overturning moment has a more significant impact on the required strength of diagonal members than the story shear.
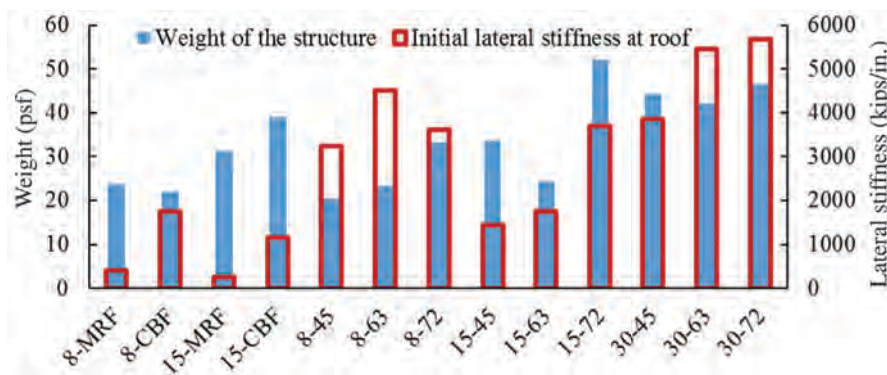
Fig. 8. Comparison of structural weight and lateral stiffness for 8-, 15-, and 30-story models.
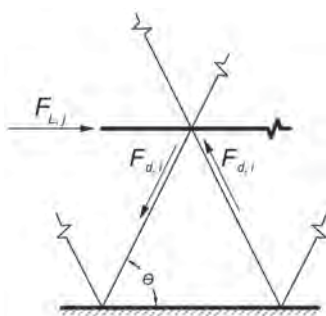
Fig. 9. Relation between the lateral load and axial forces in a pair of diagonals.

Linear Elastic Behavior

Story Drift

Figure 10 shows the variations of story drift along the height of the 8-, 15-, and 30-story models under seismic design base shear. As expected, the MRF shows the largest amount of lateral displacements as well as story drifts among all cases [Table 2 and Figures 10(a) and (b)]. The mean story drift for the MRF is three times larger than that of 8-45 and 2.5 times larger than that of the CBF. In general, diagrid models have lower story drifts than the CBF, as well. In Figure 10(a), two observations are made regarding the CBF. First, the story drift is the largest in the middle stories, which indicates the dominance of shear deformation. Second, the only diagrid with a larger story drift than the CBF is the 8-72 model.

The story drift of the 8-72 model increases considerably at the seventh and eighth stories [Figure 10(a)]. The 72° models consist of a number of 3-story modules along the height of the structure. In case of the 8-72 model, the uppermost module has only two stories (Figure 11), leading to a major increase of the lateral displacement at the seventh and eighth floors. This diagrid pattern is not recommended because it has undesirable elastic as well as nonlinear responses (discussed in the next section).

In diagrids, there are a few jumps in the story drift curve between some neighboring stories, especially in the upper stories of the structure (Figure 10). The jumps are comparatively small in the 45° models but considerably large in the 72° ones. There are two main reasons for this behavior. First, the diagrids are particularly sensitive to the diagonal axial strength, and a small change of diagonal cross-section has a considerable effect on their story drift and elastic response. Second, this behavior is partly due to the way diagonals
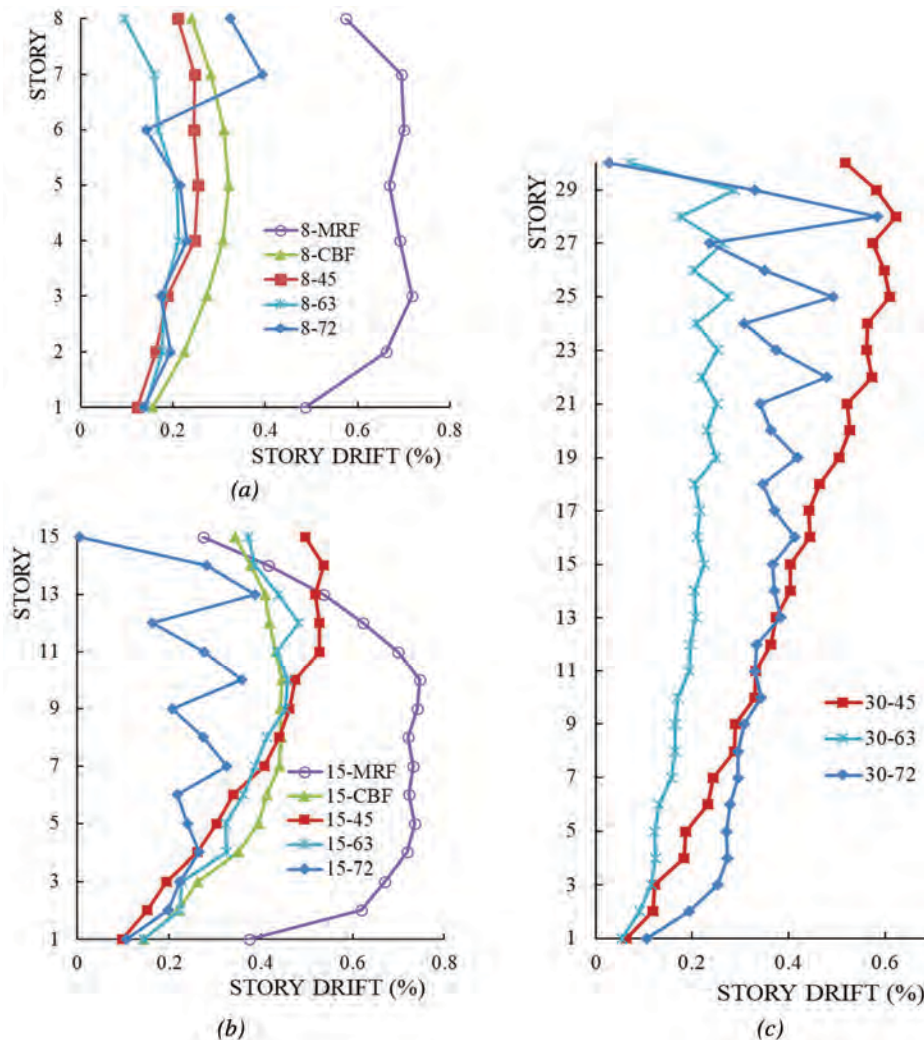
Fig. 10. Comparison of story drift for (a) 8-; (b) 15-; (c) 30-story models.

intersect with the floor beams. In each diagrid module, diagonals may intersect with the floor beams somewhere within the beam span rather than at the beam ends. This adds extra joints to the system, which affects its elastic response. For example, in the 8-72 model, at floors 3 and 6, the diagonals intersect at the beam ends, but at floors 1, 2, 4, 5, 7 and 8, they intersect somewhere within the floor beam span (Figure 11). This particular connection arrangement has a major effect on the nonlinear response of the system as well (discussed in the next section).

Lateral displacement changes similarly along the height of the 15- and 30-story models. As shown in Figures 10(b) and (c), story drift curves of the 15- and 30-story diagrids have also a number of noticeable sudden changes along the height. In the 15-story models, the 15-72 model has the smallest mean story drift but with more noticeable jumps at every three stories (where the diagonal cross-section changes). The mean story drifts for 15-45, 15-63 and 15-CBF are relatively close (Table 2). Among the 30-story models, however, the 30-63 has the smallest mean story drift similar to the 8-story models. The story drift of the 30-72 model is the largest for the lower one-third part of the structure but becomes smaller than that of 30-45 model from the 11th story to the roof. Therefore, the effect of the diagonal angle on lateral stiffness is not uniform along the height and may vary from story to story.

Fundamental Period

The mean fundamental period of diagrid models is less than the fundamental period of the MRF and CBF models (Table 2). The fundamental period of diagrids is also smaller than the generally conservative approximate period equation provided by ASCE/SEI 7 (2010), $T_a = C_t h_n^x$, by up to 59%. This indicates a need to develop more accurate approximate equations for diagrids as explained earlier.

Elastic Lateral Stiffness

Figures 12(a), (c), and (d) show the pushover curves for the 8-, 15-, and 30-story models, respectively. Figure 12(b) shows the lateral displacement curves for the 8-story models. The pushover curves start with a constant slope representing the elastic lateral stiffness reported in Table 2. As indicated in Table 2, mean initial stiffness of the 8-story diagrids is considerably larger than those of 8-MRF and 8-CBF models, by 90% and 54%, respectively. Similarly, the mean initial stiffness of the 15-story diagrids is 89% and 50% larger than 15-MRF and 15-CBF, respectively.

Figure 8 illustrates a comparison of the elastic stiffness of different models. Among 8-story diagrids, 8-63 has the largest lateral stiffness and load carrying capacity [Figures 12(a) and (b)]. This is partly due to its near-optimal diagonal angle under a combination of shear load and overturning moment.
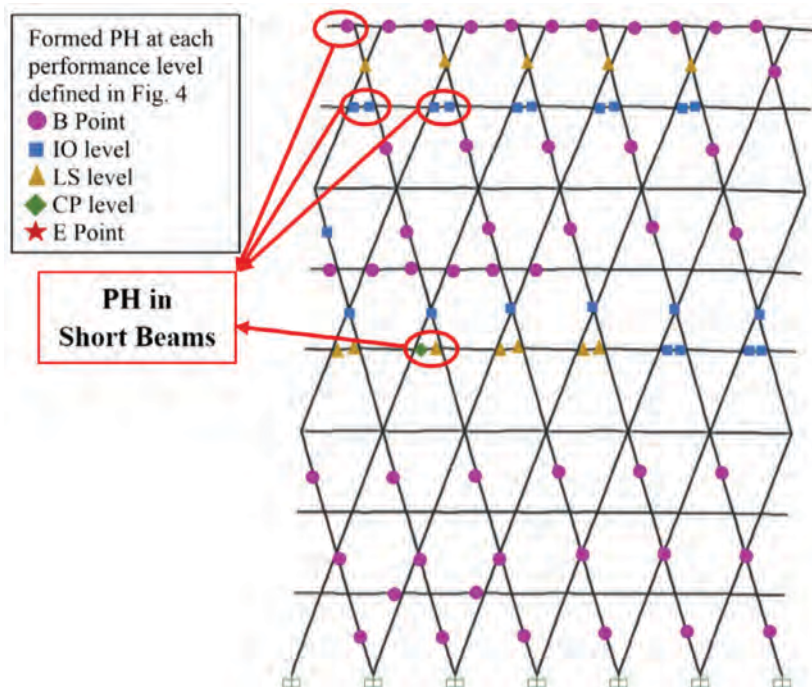
Fig. 11. Deformed shape of 8-72 model at the ultimate load magnified by a factor of 6.

The 8-72 model also shows a larger lateral stiffness than the 8-45 model, despite the fact that the uppermost module of diagrid in the 8-72 model is an incomplete 2-story module. This indicates that the 72° of the diagonal angle may result in better behavior in terms of lateral stiffness. This observation is confirmed in the 15-story models, where the 15-72 model has the largest elastic lateral stiffness [Table 2 and Figure 12(c)].

Sequence of Plastic Hinge Formation and Failure Mechanism

Plastic analysis and study of the formation of PH provide insight into the nonlinear behavior of structures (Adeli and Chyou, 1986). This section is a comparative study of the nonlinear plastic behavior of all models under lateral pushover load. The assumptions for this section are the same as those given earlier. The sequence of PH formation in the diagonals

generally depends on these factors: the axial demand-to-capacity ratio of the diagonals (the reciprocal of the member overstrength factor), the diagonal location in the plan and elevation, and the type of stress in the diagonals (compressive or tensile). PH will start developing in the diagonals with a larger axial demand to capacity ratio (near the ratio of 1.00) first. Furthermore, because of buckling and shear lag, the farther the diagonal is from the compressive corners, the later the formation of the PH will be. Due to the shear lag effect, corner diagonals are more likely to form PH first than other diagonals of each story. In addition, depending on the direction of the lateral load, the diagonals under compression are likely to fail earlier than those under tension.

The first PH in all diagrid models is formed in the diagonal located at the corner of the first story. Figure 11 shows the deformed shape of the 8-72 model at its ultimate load magnified by a factor of 6. PH developed at the start of the inelastic behavior (point B in Figure 4); performance levels
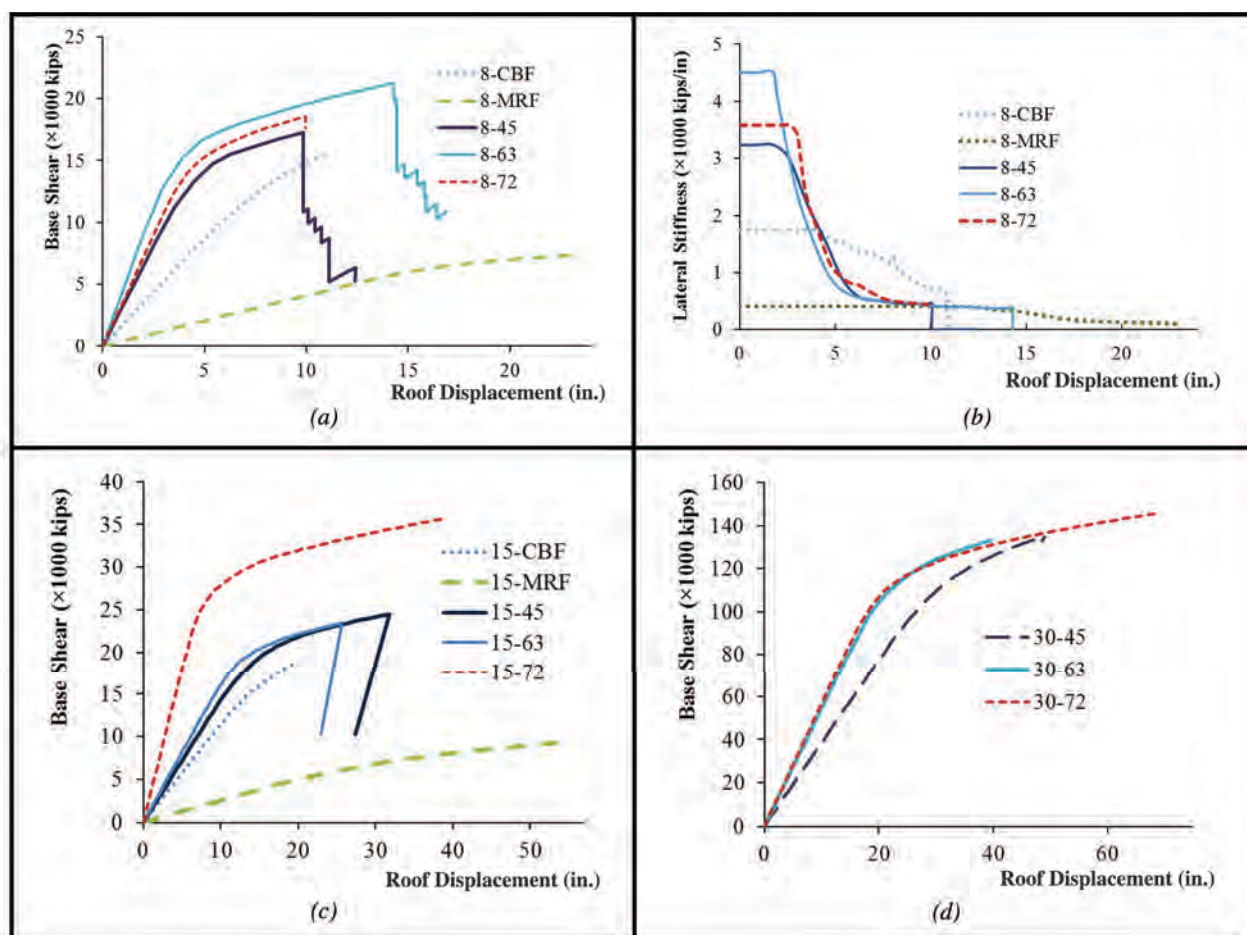

Fig. 12. (a) Pushover curves for 8-story models; (b) lateral stiffness curves for 8-story models; (c) pushover curves for 15-story models; (d) pushover curves for 30-story models.

IO, LS and CP; and the rupture point (point E in Figure 4) are identified by solid circles, squares, triangles, diamonds and stars, respectively. Diagrids having a 72° diagonal angle show a different behavior than the 45° and 63° models in terms of PH formation. In 72° models, PH spread to floor beams early and develop relatively quickly one after another compared to the 45° and 63° models. This distinctive behavior is related to the way diagonals intersect within the span of the floor beams in these models, as explained earlier, which creates a series of short floor beams. These short beams shown in Figure 11 are where the early PH are formed. Depending on the diagonal angle, story height, and floor plans, such connections are likely to be used in diagrids, and their distinctive inelastic behavior need to be addressed properly in the frame and the connection design procedure.

The 8-63 structure shows a better plastic behavior than the 8-45 and the 8-72 ones. In the 8-63 structure, hinges are spread both horizontally and vertically across the structure more broadly than the other 8-story diagrids. This can be inferred in the pushover curve as the 8-63 model shows a larger load-carrying capacity compared with other models

[Figure 12(a)]. In 15- and 30-story models, however, the 72° models show a better distribution of PH across the diagonals and the beams. Figure 13 shows the deformed shape of the 30-72 and 30-45 models at their ultimate load magnified by a factor of 6. This figure shows a large number of PH formed in beams and diagonals of 30-72 model, indicating desirable nonlinear performance and progressively failure, and some of the beam PH are developed at a higher performance level than the diagonal PH.

The governing failure mechanism in the 45- and 63-diagrids studied in this research was found to be a soft-story mechanism. As an example, Figure 14 shows the deformed shape of the 15-63 model at the formation of a soft-story mechanism at the fourth story magnified by a factor of 6. As illustrated, the failure occurs as PH are formed in all compression diagonals, some tension ones, and most floor beams of the fourth story, which is an intermediate story as opposed to the more commonly observed first story. At this point, load-carrying capacity decreases substantially when diagonals reach their rupture limit (point E in Figure 4). Figure 14 depicts a possible undesirable failure
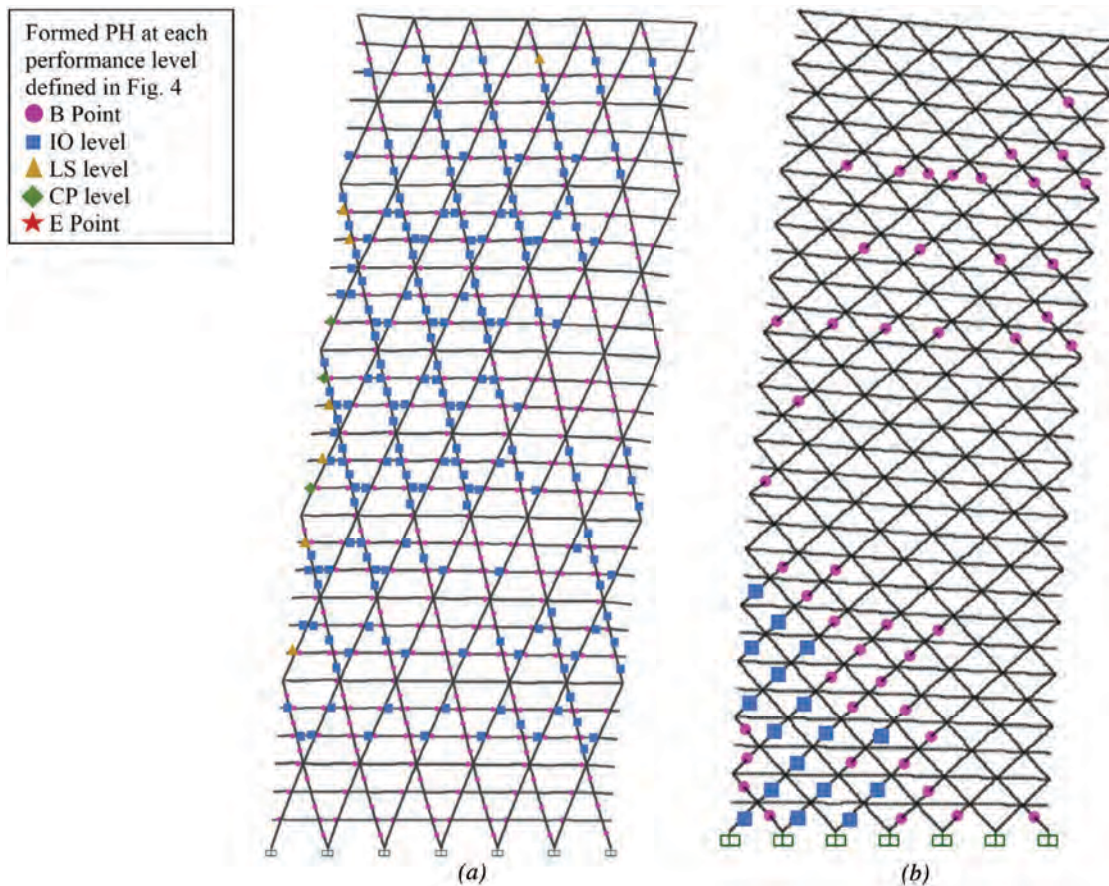

Fig. 13. The deformed shape of the (a) 30-72 and (b) 30-45 models at the ultimate load magnified by a factor of 6.

mechanism in diagrid structures where plastic hinges are not developed properly and premature soft-story failure leads to an overall collapse of the structural system.

PH are well spread across the frame for most cases, except for the 8-72 model (Figure 11). In all cases, the soft story tends to form in an intermediate story of the structure where a major change in diagonal cross-section exists. For instance, the soft story is formed in the fourth and the seventh stories of the 8-63 and the 15-45 models, respectively.

The first few PH in the 8-CBF model are formed in the coupling beams of the fifth floor. This is followed by the formation of PH in the coupling beams of the fourth and sixth floors and the braces of the second and third stories. The first PH in the columns was observed in the compression column of the first story and after formation of several PHs in beams and braces. This sequence is generally desirable because columns should be the last to yield or buckle. In addition, the PH spread to different members across the structure reasonably well. This is basically the sequence of PH formation at different performance levels (IO, LS and CP) for all CBF. The sequence of PH formations for the 15-CBF model is generally similar to 8-CBF, except for the location of the first hinge, which is formed in the fourth-story brace.

In case of MRF, the first PH forms in the compression column of the first story. PH spread to beams and columns of the other stories from lower stories to the roofs and the failure mechanism forms as all columns of the first story form a PH at the top and the bottom ends (first soft-story sway mechanism).

DESIGN CONSIDERATIONS

Virtual Work/Energy Diagram

The concept of virtual work/energy (Cha and Buyukozturk, 2015) and the corresponding distribution diagram can be used effectively to find the members that need to be stiffened to achieve improved structural deformation (CSI, 2011). The virtual work is defined for each degree of freedom (DOF) of the finite element model as the force times the displacement at that DOF. The summation of these virtual works for any member is the virtual work of that member. Figures 15(a) and 15(b) show the normalized virtual work distribution of the diagonals for the 8-45 and 30-72 models along with their height under lateral seismic load, respectively. For the 30-72 model, the mean virtual work of each 3-story module (instead of each story) is illustrated. Moreover, Figure 16 illustrates this distribution for the 8-45 model in a 3D surface diagram. For the sake of comparison, the virtual work values in Figures 15 and 16 are normalized by the maximum virtual work in the structure.

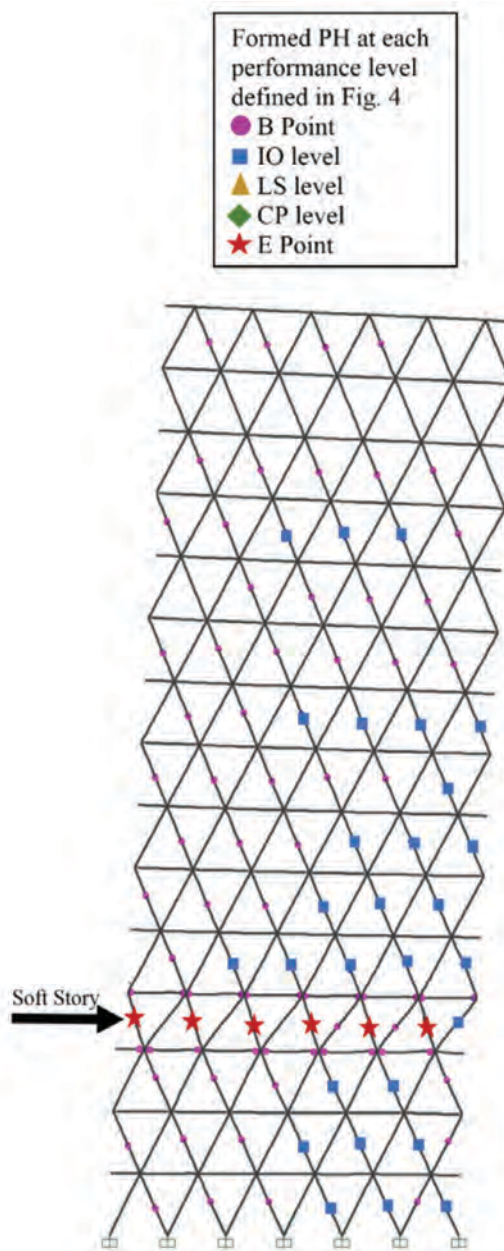For the web diagrid of the 8-45 model, the corner diagonals

Fig. 14. The deformed shape of the 15-63 model at the formation of a soft-story mechanism at the fourth story magnified by a factor of 6.
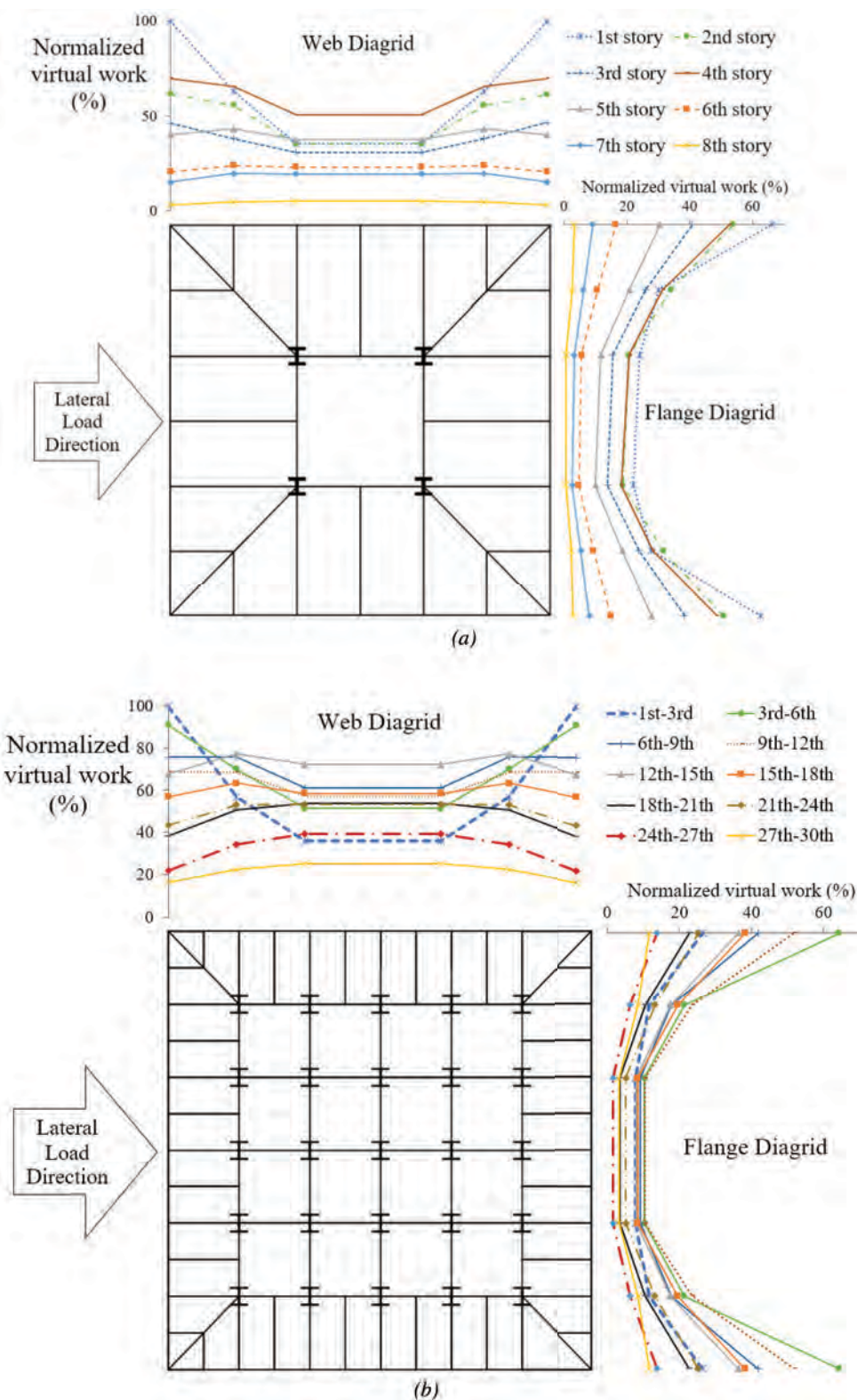
Fig. 15. Normalized virtual work distribution of (a) the 8-45 model for different stories; (b) the 30-72 model for different 3-story modules.

of the first story have the largest virtual work. Other diagonals of the first story have a substantially smaller value. This variation is different for other stories. In the second and the third stories, the difference between the corner diagonals and middle ones is much smaller than that of the first story. Along the height of the structure from the first story to the roof, the virtual work of the corner diagonals decreases while that of the middle diagonals increases. The mean virtual work is reduced from the first to the third stories. But in the fourth story, a sudden increase happens and the virtual work values increase such that they are larger than those of the second and third stories. This is manifested as a peak at the fourth story on the 3D virtual work diagram of the 8-45 model (Figure 16). The fourth story is where the diagonal sections are reduced based on the grouping approach explained earlier. More importantly, the fourth story is where the soft-story mechanism is formed, resulting in the collapse of the structure. The soft story tends to form in the middle one-third section of the structure (approximately between the third and fifth stories) where the mean virtual work is relatively large and the virtual work distribution is near-uniform across the diagrid width. On the other hand, in the one-third uppermost part of the 8-45 diagrid (sixth to eighth stories), the virtual work of the middle diagonals is slightly larger than that of corner ones [Figure 15(a)]. This suggests that in this part of the structure, the middle diagonals need to be stiffer than the corner ones, which is completely dissimilar to the variation observed in the lower stories (first to fifth). In addition, the mean amount of virtual work in the upper stories (sixth to eighth) is considerably smaller than

that of the lower ones, indicating that the upper stories are not critical in terms of lateral displacement.

In the flange diagrid, the virtual work variation for different stories is similar [Figure 15(a)]. The virtual work is larger in the corner diagonals for all stories and, similar to the web diagrid, there is some noticeable increase in the virtual work of the fourth story. Nonetheless, the mean value for the flange diagrid is smaller than that of the web diagrid.

Other models, including the 30-72, have a similar distribution of virtual work across the height and width of the web and flange diagrids. In the case of the 30-72 model [Figure 15(b)], the corner diagonals of the first module have the largest virtual work, whereas the middle diagonals of that module have a significantly smaller virtual work. From the 18th story to the 30th (approximately uppermost one-third of the structure), this variation is inverted, and the middle diagonals have a larger virtual work than the corner ones. Furthermore, the jumps due to the change of the diagonal section are not quite noticeable because diagonal sections are changed in each module every three stories.

General Recommendations

Under lateral loads, diagrids behave predominantly analogous to thin plates, where the diagonal grids form a thin plate subjected to in-plane lateral loads. This similarity is useful in developing practical design methods and formulas for diagrid design. The lateral displacement of diagrids is mostly due to overall bending of the structure known as chord drift as opposed to the shear lateral deformation,
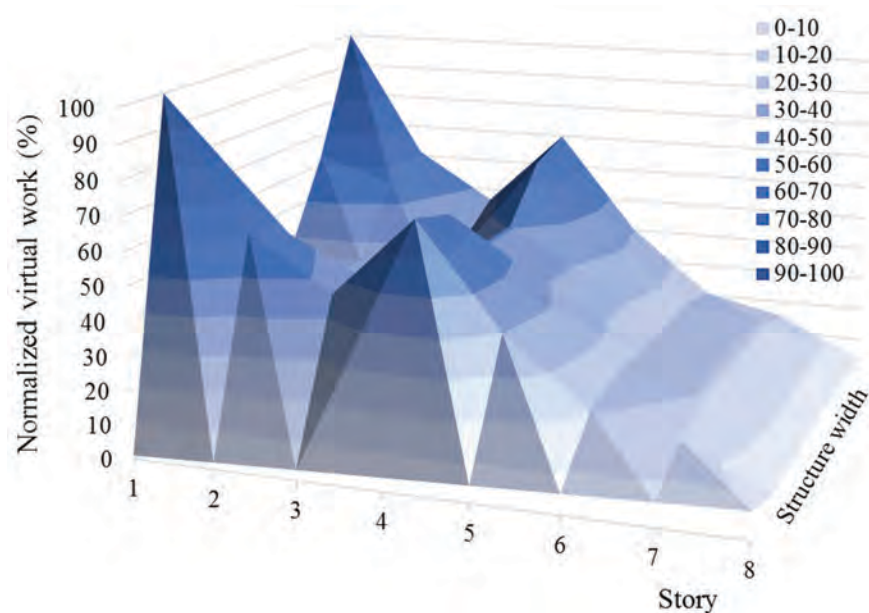

Fig. 16. Normalized virtual work distribution for different stories in the web diagrid of the 8-45 model.

similar to the bending deformation of shear walls. In a bending displacement, corner members in the web loading plane are under large compression or tension in all stories, and these forces are particularly large in the lowest stories.

According to the virtual work diagrams, the shear lag effect is more significant in the first module of the diagrid, usually the first story. The corner diagonals of these stories are always the critical member of the structure, and their virtual work is significantly larger than other members. According to nonlinear analysis, these diagonals are the first to yield and, accordingly, the key member in overall load-carrying capacity of the structure. Thus, special design considerations, such as a larger overstrength factor for these members, can prevent premature failure and increase the ultimate load capacity of the structure.

Diagonal axial strength has a major influence on the diagrid behavior and failure mechanism. To prevent an early soft-story mechanism, the size of the diagonal cross-section should be changed gradually as much as possible. Using different diagonal sections across the width of the frame in addition to the grouping across the height can improve the structural efficiency significantly and, if carefully considered, can prevent the undesirable soft-story failure mechanism under extreme loadings. In this regard, compared with other structural systems, a key difference is the shear lag effect in diagrids—in other words, the significance of corner diagonal members. The ASCE/SEI 7 (2010) criteria for soft- and weak-story consider the stiffness of the whole story and do not necessarily prevent the soft-story mechanism initiated in corner diagonals. In high seismic regions, a synthesis of these recommendations can improve the linear and nonlinear response of the diagrid system and, possibly, its ductility.

CONCLUSIONS

This research demonstrated that diagrid can be a practical and efficient structural system in mid- to high-rise buildings. Using diagrids with an appropriate diagonal angle, the designer can significantly reduce the weight of the structure as well as the mean story drift of the building. In general, diagrids in the 8- to 15-story range have a smaller mean story drift than CBF and MRF, except for the 15-45 model, whose mean story drift is 4% larger than the 15-CBF model.

In general, due to the shear lag effect, the corner diagonals are under a larger amount of internal forces than the other diagonals of the same story. However, according to the virtual work diagrams, this difference is reversed in approximately the uppermost one-third of the structure, where the middle diagonals have a larger amount of virtual work and, consequently, are more critical than other members of that story. The axial force is the major internal force in diagonals, and preliminary design of diagrids based on axial force is a reasonable assumption.

The ASCE/SEI 7 equation for finding the approximate fundamental period $(T_a = C_t h_n^x,)$ yields a generally nonconservative result for diagrids because their fundamental period is notably smaller than that of CBF and MRF. Current codes of design also offer no specific value for diagrid ductility, overstrength, and response modification factors, and using the smallest values for those factors is largely conservative for diagrids.

Diagrids have a considerably larger initial stiffness (in the elastic region) compared to MRF and CBF, and likewise, CBF have a larger lateral stiffness compared to MRF. In terms of nonlinear behavior, diagrids show smaller ductility compared with the MRF. Lateral stiffness of diagrids decreases relatively sharply as the PH are formed in the diagonals, and they reach their corresponding ultimate load at a smaller lateral displacement than the MRF. Ductility is a highly desirable property in high seismic regions for dissipating the earthquake energy. Thus, in high seismic regions, low ductility of diagrids is an issue that should be addressed. To resolve this issue, a solution would be addition of passive dampers (such as viscoelastic dampers) (El-Khoury and Adeli, 2013; Fisco and Adeli, 2011b; Gutierrez-Soto and Adeli, 2013a) or semi-active control systems (such as semi-active hydraulic dampers) (Fisco and Adeli, 2011a; Gutierrez-Soto and Adeli, 2013b) along the diagonals of diagrids. Inclined corner members of the diagrid are the most appropriate locations for installing passive or semi-active control systems to improve the overall ductility of the structure.

Diagrids are particularly sensitive to the diagonal axial strength and sudden changes of diagonal cross-section across the height and the width of the structure should be avoided because it may result in a soft-story mechanism. The soft story tends to form in the middle one-third of the structure, where the virtual work distribution is near uniform across the diagrid width.

In recent years, significant research has been reported on design optimization of high-rise building structures using nature-inspired computing techniques such as the genetic algorithm (Adeli and Sarma, 2006; Mencia et al., 2016) and the patented neural dynamics model of Adeli and Park (Adeli and Park, 1998). Applications of formal optimization techniques to high-rise diagrid structures can result in additional structural efficiencies which are currently being pursued by the authors. Other technologies yet to be applied to diagrid structures are semi-active and active vibration control (Yeganeh-Fallah and Taghikhany, 2016; Karami and Akbarabadi, 2016) and structural health monitoring (Lin et al., 2017; Tsogka et al., 2017; Cha et al., 2017).

REFERENCES

Adeli, H. and Chyou, H. (1986), "Plastic Analysis of Irregular Frames on Microcomputers," *Computers and Structures*, Vol. 23, No. 2, pp. 233–240.

Adeli, H., Gere, J. and Weaver, W.J. (1978), "Algorithms for Nonlinear Structural Dynamics," *Journal of Structural Division,* ASCE, Vol. 104, No. 2, pp. 263–280.

Adeli, H. and Park, H.S. (1998), *Neurocomputing for Design Automation*, CRC Press, Boca Raton, FL.

Adeli, H. and Sarma, K. (2006), *Cost Optimization of Structures—Fuzzy Logic, Genetic Algorithms, and Parallel Computing*, John Wiley and Sons, West Sussex, United Kingdom.

AISC (2011), *Steel Construction Manual,* 14th Ed., American Institute of Steel Construction, Chicago, IL.

AISC (2016a), *Seismic Provisions for Structural Steel Buildings*, ANSI/AISC 341-16, American Institute of Steel Construction, Chicago, IL.

AISC (2016b), *Specification for Structural Steel Buildings*, ANSI/AISC 360-16, American Institute of Steel Construction, Chicago, IL.

Ali, M.M. and Moon, K.S. (2007), "Structural Developments in Tall Buildings: Current Trends and Future Prospects," *Architectural Science Review*, Vol. 50, No. 3, pp. 205–223.

Asadi, E. and Adeli, H. (2017), "Diagrid: An Innovative, Sustainable and Efficient Structural System," *The Structural Design of Tall and Special Buildings*, Vol. 26, No. 8 (11 pages).

ASCE (2010), *Minimum Design Loads for Buildings and Other Structures*, ASCE Standard ASCE/SEI 7, American Society of Civil Engineers, Reston, VA.

ASCE (2014), *Seismic Evaluation and Retrofit of Existing Buildings*, ASCE/SEI 41-13, American Society of Civil Engineers, Reston, VA.

Boake T.M. (2014), *Diagrid Structures: Systems, Connections, Details*, Birkhäuser, Switzerland, http://alltitles .ebrary.com/Doc?id=10838294.

Cha, Y.J. and Buyukozturk, O. (2015), "Structural Damage Detection Using Modal Strain Energy and Hybrid Multi-Objective Optimization," *Computer-Aided Civil and Infrastructure Engineering*, Vol. 30, No. 5, pp. 347–358.

Cha, Y.J., Choi, W. and Buyukozturk, O. (2017), "Deep Learning-Based Crack Damage Detection Using Convolutional Neural Networks," *Computer-Aided Civil and Infrastructure Engineering*, Vol. 32, No. 5, pp. 361–378.

CSI (2011), *CSI Analysis Reference Manual for SAP2000, ETABS, SAFE, and CSiBridge*, Computers and Structures Inc., Berkeley, CA.

El-Khoury, O. and Adeli, H. (2013), "Recent Advances on Vibration Control of Structures under Dynamic Loading," *Archives of Computational Methods in Engineering*, Vol. 20, No. 4, pp. 353–360.

FEMA (2000), *Prestandard and Commentary for the Seismic Rehabilitation of Buildings*, FEMA-356, Building Seismic Safety Council for the Federal Emergency Management Agency, Washington, DC.

FEMA (2005), *Improvement of Nonlinear Static Seismic Analysis Procedures*, FEMA-440, Building Seismic Safety Council for the Federal Emergency Management Agency, Washington, DC.

FEMA (2012), *2009 NEHRP Recommended Seismic Provisions: Design Examples*, FEMA P-751, Building Seismic Safety Council for the Federal Emergency Management Agency, Washington, DC.

Fisco, N.R. and Adeli, H. (2011a), "Smart Structures: Part I—Active and Semi-Active Control," *Scientia Iranica*, Vol. 18, No. 3, pp. 275–284.

Fisco N.R. and Adeli, H. (2011b), "Smart Structures: Part II—Hybrid Control Systems and Control Strategies," *Scientia Iranica—Transaction A: Civil Engineering*, Vol. 18, No. 3, pp. 285–295.

Grigorian, M. and Kashani, K.A. (1976), "Plastic Design of Uniformly Loaded Rectangular Diagonal Grids on Simple Supports," *Building and Environment*, Vol. 11, No. 2, pp. 131–138.

Gutierrez-Soto, M. and Adeli, H. (2013a), "Tuned Mass Dampers," *Archives of Computational Methods in Engineering*, Vol. 20, No. 4, pp. 419–431.

Gutierrez-Soto, M. and Adeli, H. (2013b), "Placement of Control Devices for Passive, Semi-active, and Active, Vibration Control of Structures," *Scientia Iranica—Transaction A: Civil Engineering*, Vol. 20, No. 6, pp. 1,567–1,578.

Jiang, X. and Adeli, H. (2005), "Dynamic Wavelet Neural Network for Nonlinear Identification of Highrise Buildings," *Computer-Aided Civil and Infrastructure Engineering*, Vol. 20, No. 5, pp. 316–330.

Karami, K. and Akbarabadi, S. (2016), "Developing a Smart Structure Using Integrated Subspace-Based Damage Detection and Semi-Active Control," *Computer-Aided Civil and Infrastructure Engineering*, Vol. 31, No. 11, pp. 887–902.

Kim, Y., Jung, I., Ju, Y., Park, S. and Kim, S. (2010), "Cyclic Behavior of Diagrid Nodes with H-Section Braces," *Journal of Structural Engineering*, Vol. 136, No. 9, pp. 1,111–1,122.

Kim, J. and Kong, J. (2013), "Progressive Collapse Behavior of Rotor-Type Diagrid Buildings," *The Structural Design of Tall and Special Buildings*, Vol. 22, No. 16, pp. 1,199–1,214.

Kim, J. and Lee, Y.H. (2010), "Progressive Collapse Resisting Capacity of Tube-Type Structures," *The Structural Design of Tall and Special Buildings*, Vol. 19, pp. 761–777.

Kim, J. and Lee, Y.H. (2012), "Seismic Performance Evaluation of Diagrid System Buildings," *The Structural Design of Tall and Special Buildings*, Vol. 21, No. 10, pp. 736–749.

Kim, D., Oh, B.K., Park, H.S., Shim, H.B. and Kim, J. (2017), "Modal Identification for High-Rise Building Structures Using Orthogonality of Filtered Response Vectors," *Computer-Aided Civil and Infrastructure Engineering*, Vol. 32, No. 12, pp. 1,064–1,084.

Lin, Y.Z., Nie, Z.H. and Ma, H.W. (2017), "Structural Damage Detection with Automatic Feature-Extraction through Deep Learning," *Computer-Aided Civil and Infrastructure Engineering*, Vol. 32, No, 12, pp. 1,025–1,046.

Mencıa, R., Sierra, M.R., Mencıa, C. and Varela, R. (2016), "Genetic Algorithms for the Scheduling Problem with Arbitrary Precedence Relations and Skilled Operators," *Integrated Computer-Aided Engineering*, Vol. 23, No. 3, pp. 269–285.

Moon, K.S. (2008), "Sustainable Structural Engineering Strategies for Tall Buildings," *The Structural Design of Tall and Special Buildings*, Vol. 17, No. 5, pp. 895–914.

Moon, K.S., Connor, J.J. and Fernandez, J.E. (2007), "Diagrid Structural Systems for Tall Buildings: Characteristics and Methodology for Preliminary Design," *The Structural Design of Tall and Special Buildings*, Vol. 16, No. 2, pp. 205–230.

Oh, B.K., Kim, D. and Park, H.S. (2017), "Modal Response-Based Visual System Identification and Model Updating Methods for Building Structures," *Computer-Aided Civil and Infrastructure Engineering*, Vol. 32, No. 1, pp. 34–56.

Rafiei, M.H. and Adeli, H. (2016), "Sustainability in High-rise Building Design and Construction," *The Structural Design of Tall and Special Buildings*, Vol. 25, No. 13, pp. 643–658.

Shan, J., Ouyang, Y., Yuan, H.W. and Shi, W. (2016), "Seismic Data Driven Identification of Linear Physical Models for Building Structures Using Performance and Stabilizing Objectives," *Computer-Aided Civil and Infrastructure Engineering*, Vol. 31, No. 11, pp. 846–870.

Subramanian, G. and Subramanian, N. (1970), "Analysis of Simply Supported Uniform Diagrids," *Building Science*, Vol. 4, No. 4, pp. 209–215.

Tsogka, C., Daskalakis, E., Comanducci, G. and Ubertini, F. (2017), "The Stretching Method for Vibration-Based Structural Health Monitoring of Civil Structures," *Computer-Aided Civil and Infrastructure Engineering*, Vol. 32, No. 4, pp. 288–303.

Wang, N. and Adeli, H. (2014), "Sustainable Building Design," *Journal of Civil Engineering and Management*, Vol. 20, No. 1, pp. 1–10.

Yang, Y.S., Wang, W. and Lin, J.Z. (2017), "Direct–Iterative Hybrid Solution in Nonlinear Dynamic Structural Analysis," *Computer-Aided Civil and Infrastructure Engineering*, Vol. 32, No. 5, pp. 397–411.

Yeganeh-Fallah, A. and Taghikhany, T. (2016), "A Modified Sliding Mode Fault Tolerant Control for Large Scale Civil Infrastructures," *Computer-Aided Civil and Infrastructure Engineering*, Vol. 31, No. 7, pp. 550–561.

Young, K. and Adeli, A. (2014a), "Fundamental Period of Irregular Moment-Resisting Steel Frame Structures," *The Structural Design of Tall and Special Buildings*, Vol. 23, No. 15, pp. 1,141–1,157.

Young, K. and Adeli, A. (2014b), "Fundamental Period of Irregular Concentrically Braced Steel Frame Structures," *The Structural Design of Tall and Special Buildings*, Vol. 23, No. 16, pp. 1,211–1,224.

Young, K. and Adeli, H. (2016), "Fundamental Period of Irregular Eccentrically-Braced Tall Steel Frame Structures," *Journal of Constructional Steel Research*, Vol. 120, pp. 199–205.

Zhang, C., Zhao, F. and Liu, Y. (2010), "Diagrid Tube Structures Composed of Straight Diagonals with Gradually Varying Angles," *The Structural Design of Tall and Special Buildings*, Vol. 21, No. 4, pp. 283–295.

Technical Note

Fracture and Fatigue Design of the Wilshire Grand Tower

AMIT KANVINDE, PETER MARANIAN, LEONARD JOSEPH and JEFF LUBBERTS

ABSTRACT

The 1,100-foot Wilshire Grand Tower in Los Angeles owned by the Hanjin Group is the tallest building in the United States west of Chicago. The building, whose architect is AC Martin Inc., has a slender elevation in one direction, necessitating the use of heavy steel box columns filled with concrete on the perimeter, connected to the concrete core with outrigger trusses. The building has a slender, 272-ft-tall spire, also constructed from steel plates. The height and slenderness of the tower, as well as the spire, and its location in a seismically active zone motivated comprehensive analysis to mitigate the risk of steel fracture within a performance-based design framework. This analysis includes the following components: (1) development of acceptance criteria for earthquake-induced fracture, especially when it may follow years of wind-induced fatigue crack growth; (2) wind tunnel testing; (3) linear and nonlinear time-history simulations to determine stress demands in critical components under appropriate wind and seismic hazards; and (4) fracture mechanics simulations to characterize trade-offs among various design variables to meet the acceptance criteria. The analysis indicates that wind-induced oscillations have the potential to grow fatigue cracks in some components, affecting their performance during a subsequent maximum considered earthquake. This situation is unusual for steel buildings, being the result of the extraordinary height, geometry, heavy steel members, and location of this particular building. The analysis also indicates that fracture risk may be successfully mitigated through existing design and detailing approaches and acceptance criteria, along with use of steel material exhibiting high, but commercially available and affordable, specified Charpy V-notch toughness values.

Keywords: fracture, fatigue, tall buildings.

INTRODUCTION

The landmark 1,100-ft, 73-story Wilshire Grand Tower in Los Angeles (completed in 2017; see Figure 1), the tallest building in the United States west of Chicago, features innovative engineering in steel design and construction. Located in a seismically active zone, its lateral load-resisting concrete core and steel outrigger system has attracted public interest, with articles in the *Los Angeles Times* (Curwen, 2014), *Structure Magazine* (Nieblas, 2014), and *Civil Engineering* (Joseph and Maranian, 2017). The building is exceptional due to its height, complex shape, and narrow floor plan, resulting in a slender elevation, along with its prominence as the tallest building in the western United States.

Very heavy steel members (including built-up box sections) with complex connections were required to resist large forces accompanied by cyclic responses, both earthquake- and wind-induced, during its anticipated life span. The structural design team determined that this warranted consideration of effects beyond code as well as the performance-based design (PBD) procedures and criteria approved by the building department and its peer review panel. The goal was to mitigate the risk of steel fractures in framing, including column-foundation connections, column splices, outrigger elements, along with their connections, and the spire components and connections.

Specific criteria and procedures, using sophisticated simulations and probabilistic representations of seismic and wind hazards, were implemented for this building within a PBD framework (ATC, 2010, 2012). Special analyses were performed to predict and address structural fracture and fatigue demands within the design of the tower's framing system and spire, based on the anticipated demands during the expected life of the building. The primary objectives of this paper are (1) to provide an overview of unique fracture and fatigue issues faced by supertall and slender buildings constructed with heavy steel subject to seismic and wind hazards and (2) to provide guidance for mitigating these issues within the framework of current technology, industry standards, and professional practice.

Amit Kanvinde, Professor, Department of Civil and Environmental Engineering, University of California, Davis, CA. Email: kanvinde@ucdavis.edu (corresponding)

Peter Maranian, Principal, Brandow & Johnston Inc., Los Angeles, CA. Email: pmaranian@bjsce.com

Leonard Joseph, Principal, Thornton Tomasetti, Inc., Los Angeles, CA. Email: LJoseph@thorntontomasetti.com

Jeffrey Lubberts, P.E., S.E., Associate Principal, RGSE Inc., Simi Valley, CA. Email: jeffl@rgseinc.com

The paper begins by presenting an overview of the structural system and spire of the building, identifying regions that were studied for fracture resistance. Approaches used for simulation of wind and seismic hazards are then outlined; this is followed by a discussion of the methods used to simulate wind-induced fatigue followed by earthquake-induced fracture. The paper concludes by summarizing the effect of these studies on design decisions, along with broader implications for fracture assessment of special structures similar to the Wilshire Grand Center Tower.

STRUCTURAL SYSTEM AND SPIRE

The structural system, shown in Figure 2, is designed to be stiff for occupant comfort under service level wind loads while providing sufficient strength to resist seismic loads generated by this stiffness. Floor slabs on steel beams are supported by a concrete core and perimeter concrete-filled steel box columns. To suit the tower floor plan, the central core is narrow, with a roughly 4:1 plan aspect ratio. To improve building performance (i.e., control forces and deformations) in the transverse or "weak" direction, multi-story outrigger trusses connect core walls to perimeter columns at three levels. Atop the concrete core a trussed steel

Fig. 1. The Wilshire Grand Tower in downtown Los Angeles (rendering).

"sail" feature rises 100 ft. Tied to it is a 272-ft-tall spire consisting of a shell of brake-bent steel plates. The shell tapers from 6.5 ft to 2.7 ft in diameter. Each 40-ft segment of the spire has a constant plate thickness, with field-bolted end plate splices sized to avoid prying action. These elements of the structure are identified in Figure 2, along with steel connections and components subjected to special attention with respect to fracture: (1) complete-joint-penetration (CJP) connections from box column to cap plate on "starter columns" in the foundation, Figure 2(a); (2) field splices of box columns incorporating partial-joint-penetration (PJP) welds, Figure 2(b) (these welds contain an external flaw that increases fracture toughness demand); (3) starter column cap plates, as well as bolted end-plates in the spire with through thickness demands at the CJP welds, which involved reinforcing fillet welds, Figure 2(c); and (4) spire shell plates, Figure 2(d). Demands in these connections arise from both wind and seismic effects. For both the tower and the spire, wind-tunnel studies showed that vortex-induced oscillations occur in multiple modes (at different wind speeds) and generate cyclic stresses at connections. Wind-induced cyclic stresses are well below steel yield but not low enough to discount the possibility of fatigue crack growth from a large number ($\sim 10^6$) of cycles (high cycle fatigue). Conversely, seismic demands, especially at the maximum considered earthquake (MCE) level, induce stresses on the order of the yield stress, but with only a few (~ 10–20) cycles (ultra-low cycle fatigue).

The next section summarizes the simulation of demands; these are in the form of stress ranges and cycles for wind loading and peak stresses for earthquake loading.

SIMULATION OF WIND AND SEISMIC EFFECTS WITHIN A PERFORMANCE-BASED DESIGN FRAMEWORK

Key to PBD is probabilistic simulation of natural hazard effects (wind, earthquake) and setting of target structural performance objectives or acceptance criteria under these hazards. As for most buildings, wind-induced fatigue in itself is not a controlling limit state for the Wilshire Grand Tower. However, wind tunnel studies of both tower and spire (in conjunction with structural simulations) indicated the potential for wind-induced oscillations capable of causing fatigue crack extension in critical components, increasing the vulnerability under a late-in-life major seismic event. Acceptance criteria for this newly plausible wind followed by earthquake scenario are not established, in contrast to those that do exist for purely seismic limit states (see, e.g., ATC, 2010). As a result, new acceptance criteria were developed specifically for this project. For elements of the tower itself, the performance objective was to prevent fracture, or to have a negligible probability of its occurrence, in the scenario of the MCE earthquake occurring even after 100 years
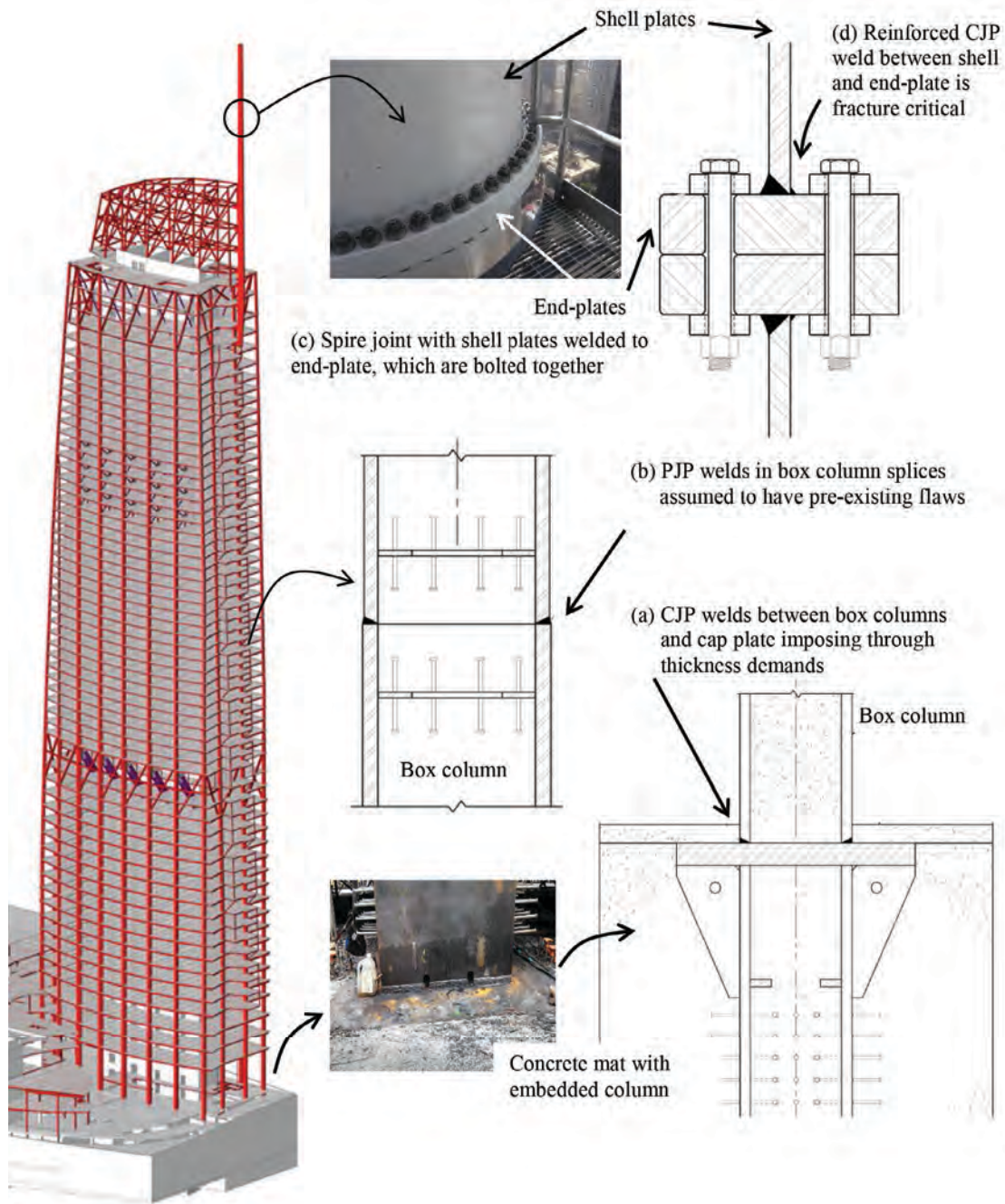
Fig. 2. Selected fracture critical details in the tower and spire.

of wind fatigue accumulation. For elements of the spire, an MCE event after a 50-year wind exposure window was selected.

Simulation of Wind Effects

To meet the acceptance criteria previously outlined, it is necessary to estimate fatigue crack growth during the time windows of interest—that is, 100 and 50 years for the tower and spire, respectively. This entails characterization of the stress cycles (both the stress ranges as well as the number of cycles in each range) due to wind-induced oscillations. The effect of wind-induced oscillations on the tower and spire was assessed through wind tunnel testing conducted on 1/400 and 1/60 scale models, respectively, by Rowan Williams Davies and Irwin (RWDI) Inc. Figures 3(a) and 3(b) show photographs of the tower and spire being subjected to wind loads. The tower study used a "rigid-building" wind tunnel model, where aero-elastic interactions between the model and the wind flow were disregarded (as is often the practice). Building deformations were not measured, while the base moments were. The spire study used an aero-elastic model focusing on the first three vibration modes. Specifically, the wind tunnel tests and associated modeling included the following tasks:

1. A statistical wind climate model was developed for the site based on wind data measured at Los Angeles International Airport. This model includes mean annual frequencies of exceedance of wind speeds, including the effects of directionality. This model may be used to determine the duration the building spends in each wind regime (i.e., combination of direction and wind speed) over a given time window.

2. For each plausible wind regime, wind tunnel testing was used to record building oscillations, which are irregular and complex in form. These were subsequently converted to equivalent sets of constant range cycles; this included characterization of mean and range quantities (such as base moment along each axis of the building), along with cycle counts (determined per hour).

3. The wind tunnel data generated in this manner were used in conjunction with structural models to determine stress history information (i.e., mean stress, stress-range, and cycles per hour) at the component level corresponding to each wind regime. The mean stress, along with the stress ranges, may be used to determine the "stress ratio" for each set of cycles; this is subsequently used in the calculation of a threshold stress range above which fatigue cracks tend to grow.

4. The final step involved integrating these data with the wind climate model (point 1) to determine stress cycle data at each critical component (i.e., the components in Figure 2) over the time window of interest. Table 1 provides a sample of such data, which are used (as discussed in a subsequent section) to estimate fatigue crack growth.

Simulation of Seismic Effects

Nonlinear response history analysis (NLRHA) simulated both geometric and material nonlinearity in the structure. For MCE-level motions (2,475-year mean recurrence interval), multiple time-history suites were rigorously selected through a peer review process to address both M7.8 strike slip events on the distant San Andreas fault and M6.6 events on a reverse or reverse-oblique local fault—for example, the Puente Hills Blind Thrust Fault. Based on the NLRHA,

(a)   *(b)*

Fig. 3. Wind tunnel model of (a) tower and (b) spire.

Table 1. Sample Table Showing Stress Cycle Data		
Stress Range Δσ, ksi	Number of Cycles, *N*	Mean Stress, ksi
6.3	565330	4.41
8.4	90190	5.88
10.5	17208	7.35
12.6	3423	8.82
…	…	…
..	..	..

the peak stresses were recorded for all critical components, including those identified previously in Figure 2. The simulations indicate that although none of the fracture critical components studied would have significant inelastic deformation, stresses in some components approach the yield strength. Note that components designed to be dissipative (e.g., the buckling restrained braces) are not fracture critical due to special detailing, except where their gusset plates are welded to large embedded plates in the core walls. In these cases, welding requirements followed those used at the connections from box columns to cap plate at the starter columns.

Simulation of Fatigue Crack Growth Followed by Fracture

The well-known Paris's fatigue law (Paris and Erdogan, 1963) was used to estimate fatigue crack growth in the components of interest. Paris's law, commonly used for fatigue assessment of mechanical and aerospace components, relates the rate of crack growth per stress cycle to the stress range (given the presence of a crack or flaw). Equation 1 expresses Paris's law mathematically, whereas Figure 4 illustrates the associated quantities and process for the
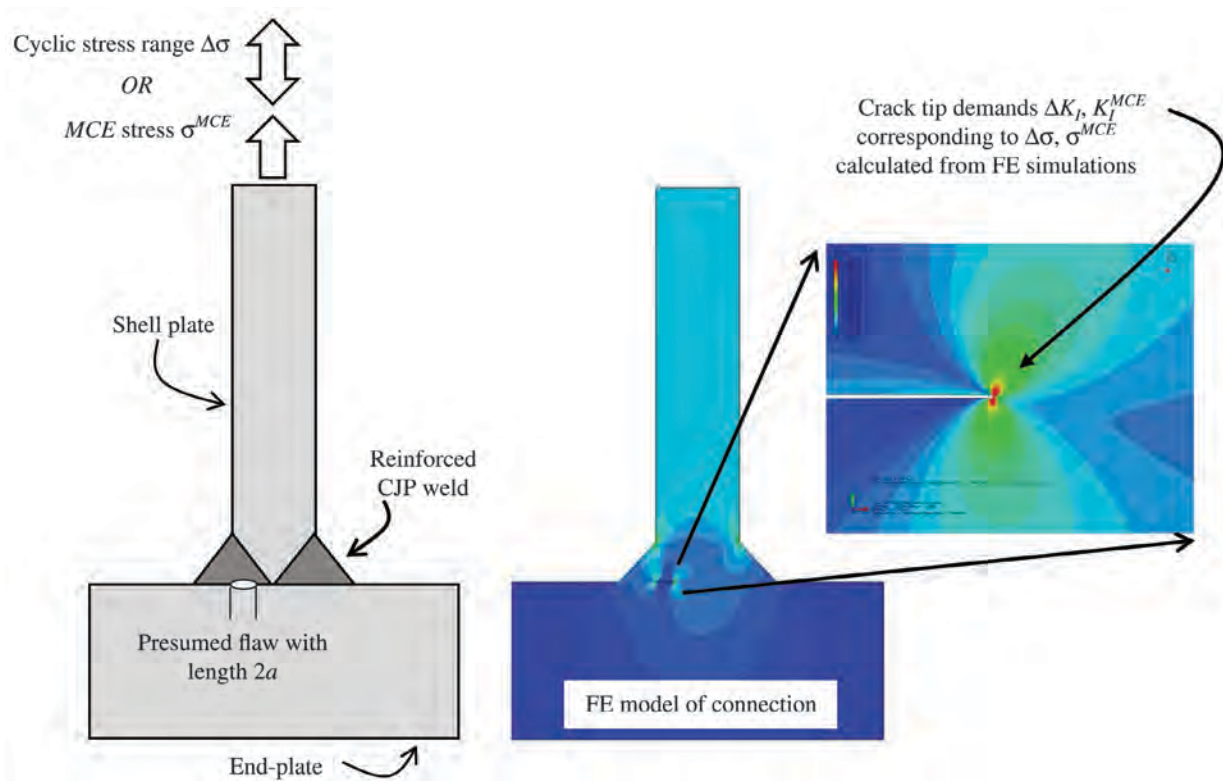

Fig. 4. Finite element model of spire connection (shown previously in Fig. 2) to determine crack tip conditions for fatigue crack growth and fracture.

shell-plate to end-plate connection in the spire shown previously in Figure 2(d).

$$\frac{da}{dN} = C(\Delta K_I)^m \text{ for } \Delta K_I \geq \Delta K_{I\text{-thresh}}; \qquad (1)$$

$$\frac{da}{dN} = 0 \text{ for } \Delta K_I < \Delta K_{I\text{-thresh}}$$

In Equation 1, da/dN denotes the rate of crack growth with respect to the number of cycles (a denotes crack length; N denotes number of cycles), whereas ΔK_I represents the range of the stress intensity factor K_I (in which the subscript I refers to mode I or crack opening), corresponding to the range of applied stress, $\Delta\sigma$ (see Figure 4). The terms C, m and $\Delta K_{I\text{-thresh}}$ are material parameters. Of these, the first two are taken as 3.6×10^{-10} and 3.0, respectively, for structural steel, whereas the threshold value $\Delta K_{I\text{-thresh}}$ depends on the ratio of minimum to maximum stress within the stress range (Barsom and Rolfe, 1999). The stress intensity factor (Anderson, 1995) relates remotely applied stresses to the crack tip stress field through relationships involving the crack length and specimen geometry. Equation 2 expresses such a relationship:

$$\Delta K_I = (\Delta\sigma)\alpha\sqrt{\pi a} \qquad (2)$$

The factor α is geometry dependent and may be determined through finite element simulation or analytical expressions (e.g., Rooke and Cartwright, 1976). For critical components in the tower and spire, the law was applied in the following manner:

1. An initial flaw was assumed in the component. The shape and size of this flaw were based on the specific detail, the way the flaw would be introduced (weld lack-of-fusion, material inclusion), and the resolution and acceptance criteria of ultrasonic testing for flaw detection. For example, Figure 4 illustrates a possible lack-of-fusion flaw in the CJP weld. Various initial flaw dimensions and locations were tested to inform design trade-offs against inspection criteria.

2. The stress-cycle ranges for each component and time window (as shown previously in sample Table 1) were interpreted through Paris's fatigue law to determine growth of the assumed flaw, by integrating Equation 1. Note that the integrand of the equation contains ΔK_I, which itself is a function of the evolving crack length as expressed in Equation 2. Consequently, the integration is performed numerically by discretizing the cycle groups in Table 1 into smaller bins. The cycle groups are applied in various orders (decreasing, increasing, or random amplitude sequences) to determine the sequence that results in the greatest crack growth at the end of the time window; this crack length is denoted as $a_{fatigue}$.

3. Once wind-induced fatigue crack growth at the end of the time window was determined for each component, fracture mechanics analyses were conducted to determine the toughness requirements to meet demands under MCE level stresses. In cases where crack tip yielding was expected to be limited (either due to geometry or lower MCE stresses), linear elastic fracture mechanics was used, including application of the stress intensity factor K_I^{MCE} to find MCE-level demands for establishing required toughness. When significant crack tip yielding was expected, elastic plastic fracture mechanics was used, relying on the J-integral as the fracture toughness demand (Rice, 1968). In many cases, where expressions relating K_I^{MCE} to σ^{MCE} were available in literature (Anderson, 1995) or in compendia of stress-intensity factor solutions (Rooke and Cartwright, 1976), K_I^{MCE} could be determined conveniently in a manner similar to ΔK_I for fatigue stresses, by using MCE-level stresses and the length of the fatigue crack (as computed previously). Specifically,

$$K_I^{MCE} = \sigma^{MCE}\alpha\sqrt{\pi a_{fatigue}} \qquad (3)$$

In some situations (e.g., CJP welded joints in the spire with reinforcing fillet welds; see Figure 2), such expressions were not available. In these cases, or when crack tip plasticity was expected, continuum finite element simulations (such as the one shown in Figure 4 for the joint previously shown in Figure 2) were used to determine fracture toughness demands. These simulations also included the effects of welding-induced residual stresses on the computed fracture toughness demands.

4. The fracture toughness capacity K_{IC} is not usually specified or measured for structural steel used in seismic construction because professional practice (including the 2016 AISC *Seismic Provisions*) relies on having material with minimum Charpy V-notch (CVN) energy measured at specific temperatures that is, 20 ft-lb at and 40 ft-lb at 70°F from heat input envelope testing. Barsom and Rolfe (1969) provide a convenient correlation between the CVN energy and a dynamic fracture toughness value K_{ID}, as shown in Equation 4:

$$K_{ID} = 0.001\sqrt{(0.005\text{CVN})E} \qquad (4)$$

where K_{ID} represents the dynamic fracture toughness (in the units of $\text{ksi}\sqrt{\text{in}}$.), which is associated with the high strain rate of a Charpy energy test, while E is the modulus of elasticity in ksi, and CVN is the measured energy in ft-lb. However, strain rates during seismic events are significantly lower (on the order of 0.01–0.1 strain/second, as compared to 1–1000 strain/second for Charpy specimens; see Lei et al., 1993). It is well known (Barsom and Rolfe, 1999) that high strain rates reduce fracture

toughness. To resolve this, the dynamic toughness K_{ID} may be reinterpreted as the available toughness at a lower temperature, through a "temperature shift," which depends on the strain rate (Barsom and Rolfe, 1999). For the Wilshire Grand Tower and spire, this implies that K_{ID}, as determined through Equation 4, using dynamic CVN measurements at 70°F provides a conservative estimate of fracture toughness under seismic loading rates for service temperatures above 35°F. This difference (35°F) is greater than the difference (20°F) implied by the AISC *Seismic Provisions* (AISC, 2016), which assumes a LAST (lowest anticipated service temperature) of 50°F.

Once both the toughness demand and capacity are thus established, they may be compared to assess the safety of a given component and guide design refinements to meet acceptance criteria. The next section describes this process.

EFFECT ON DESIGN DECISIONS

For each fracture critical component, the process just described was conducted with various trial input variables to meet the acceptance criteria (i.e., toughness demands less than capacity for MCE stresses after 50 or 100 years of fatigue crack growth). Figure 5 shows a representative graph summarizing the results of this type of analysis for one such component, the connection in the spire shell plate shown earlier in Figure 4. The figure indicates that acceptance criteria can be achieved through a combination of three variables: (1) providing adequate material fracture toughness—that is, the specified CVN value(s); (2) controlling stresses within the component by increasing weld sizing/reinforcing fillets where needed; and (3) restricting the initial flaw size based

on the detection techniques used and their precision. In this context, it is relevant to note that AWS D1.1 (2010) was used for quality control and quality assurance with requirements similar to AWS D1.8 (2009) noted on the drawings. All complete penetration welds and some partial penetration welds were tested by ultrasonic testing, and magnetic particle testing was carried out on some of the partial penetration welds and fillet welds. During construction, reinspection—including visual, magnetic particle, and ultrasonic testing—was carried out to check for possible delayed cracking.

Figure 5 shows that the consequences of larger permissible initial flaw size may be mitigated through either tougher material or a thicker shell plate. With the knowledge of such trade-offs, each of these design variables may be controlled within the constraints of available materials, technology and cost to obtain acceptable performance. In some locations, this approach involved specifying higher material toughness than mandated by existing standards, for example:

1. The cap plates on the starter columns [Figure (2a)], as well as other similar plates, subjected to through thickness demands, required a CVN of 59 ft-lb at 70°F in the through-thickness direction. CVN tests were carried out in the weld material and the heat affected zone (HAZ). The steel material required a yield ratio less than 0.85.

2. Welding procedure specifications for complete penetration welds, with connection plate subject to through-thickness loading, required testing per ASTM 770 (2012), with a 25% minimum reduction required in weld material and the HAZ.

3. The spire end plates, subjected to through-thickness loading, required CVN testing of 20 ft-lb at 70°F in the
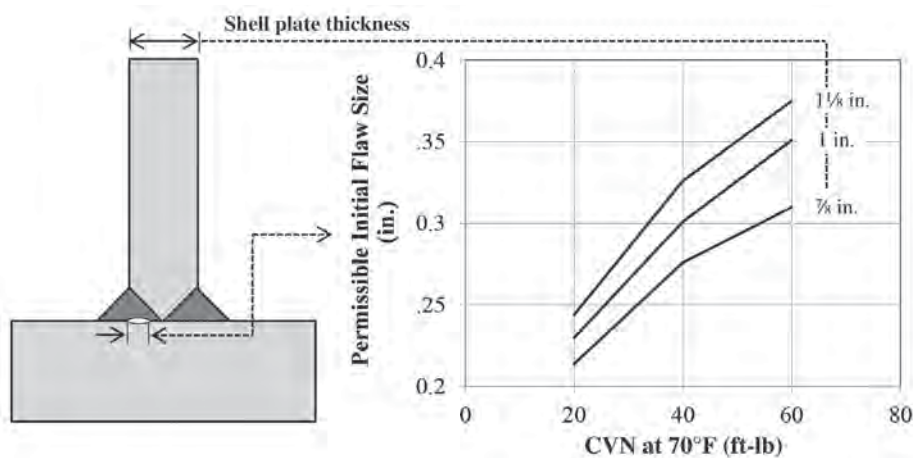

Fig. 5. Finite element model of spire connection (shown previously in Figs. 2 and 4) to determine crack tip conditions for fatigue crack growth and fracture.

through-thickness direction. Similar to cap plates on the starter columns, CVN testing was performed on the weld material and HAZ. The steel material required a yield ratio < 85%.

4. Welding procedure specifications for the spire shell plate to flange plate complete penetration welds, which included reinforcing fillet welds, required testing per ASTM 770 (2012) with a 25% minimum reduction required in weld material and HAZ.

In other situations, such as buckling restrained brace (BRB) gusset plates welded to large embedded plates in the core walls, toughness was specified and tested in the through-thickness direction of the plate, which is not typically done (e.g., the base plate shown previously in Figure 2). Finally, at all regions where fracture was a possibility, ultrasonic testing was specified on base metal subjected to through-thickness stresses, and on complete penetration welds, to detect and limit flaws to within acceptable sizes.

SUMMARY

As a landmark steel building in Los Angeles, the Wilshire Grand Tower received project-specific fracture analysis with a degree of sophistication rarely used before in the building construction industry. The analysis was suited to the PBD approach used for the building's design and its location in a seismically active region. Key findings were that wind-induced oscillations have the potential to grow preexisting flaws in the building over its lifetime and that consideration of this flaw growth is warranted while examining performance under MCE level seismic shaking.

As climatological hazards evolve, this type of multi-hazard interaction may become commonplace, and the analysis described here provides a rational methodology to assess risk under such interacting hazards. It is interesting to note that the findings, using this methodology, naturally extend the industry direction (motivated by the 1994 Northridge earthquake) toward improvements in material toughness, detailing, and material requirements. Stringent performance objectives can successfully be achieved through existing design and detailing approaches and acceptance criteria, along with steel having higher-than-typical, but commercially available and affordable specified CVN values. This is very helpful for using steel in large structures in highly seismic regions that can be subjected to wind-cyclic fatigue loading. In fact, the analysis procedures and risk mitigation measures, outlined in this study, are enabled by a confluence of two key factors: (1) increased awareness of fracture in steel structures and strategies for mitigation, after the Northridge earthquake, and (2) maturation of PBD methodologies, facilitated by landmark documents such as FEMA P-58 (ATC, 2012) and ASCE 41 (2014). In this broader context, the procedures established for this project should continue to be researched and developed further for use in similar special structures.

REFERENCES

AISC (2016), *Seismic Provisions for Structural Steel Buildings*, ANSI/AISC 341-16, American Institute of Steel Construction, Chicago, IL.

ASCE (2014), *Seismic Evaluation and Retrofit of Existing Buildings*, ASCE 41-13, American Society of Civil Engineers, Reston, VA.

ATC (2010), *Modeling and Acceptance Criteria for Seismic Design and Analysis of Tall Buildings,* ATC-72-1, Applied Technology Council, Redwood City, CA.

ATC (2012), *Seismic Performance Assessment of Buildings*, FEMA P-58, Applied Technology Council, Redwood City, CA, prepared for the Federal Emergency Management Agency, Washington, DC.

Anderson, T.L. (1995), *Fracture Mechanics*, 2nd Ed., CRC Press, Boca Raton, FL.

ASTM (2012), *Standard Specification for Through-Thickness Tension Testing of Steel Plates for Special Applications*, ASTM 770/A770M-03e1, ASTM International, West Conshohocken, PA.

AWS (2009), *Structural Welding Code—Seismic Supplement*, AWS D1.8/D1.8M: 2009, American Welding Society, Miami, FL.

AWS (2010), *Structural Welding Code—Steel*, AWS D1.1/D1.1M: 2010, American Welding Society, Miami, FL.

Barsom, J.M. and Rolfe, S.T. (1969), "Correlations between KIC and Charpy V-Notch Test Results in the Transition-Temperature Range," *Impact Testing of Metals*, ASTM STP 466, pp. 281–302.

Barsom, J.M. and Rolfe, S.T. (1999), *Fracture and Fatigue Control in Structures: Applications of Fracture Mechanics* (MNL41), 3rd Ed., ASTM Press, West Conshohocken, PA.

Curwen, T. (2014), "Built to Defy Severe Quakes, the New Wilshire Grand Is Seismically Chic," *Los Angeles Times*, November 2, 2014.

Joseph, L.M. and Maranian, P.J. (2017), "Grand Performance," *Civil Engineering*, ASCE, October Edition, pp. 48–57.

Lei, W., Van, X. and Yao, M. (1993), "Numerical Analysis of Strain Rate Field below Notch Root of Charpy V-Notch Test Specimen under Impact Loading Condition," *Engineering Fracture Mechanics*, Vol. 46, No. 4, pp. 583–593.

Nieblas, G. (2014), "Reaching New Heights in Los Angeles," *Structure Magazine*, December 2014.

Paris, P. and Erdogan, F. (1963, December), "A Critical Analysis of Crack Propagation Laws," *Journal of Basic Engineering*, ASME, Vol. 85, No. 4, pp. 268–280.

Rice, J.R. (1968), "A Path Independent Integral and the Approximate Analysis of Strain Concentrations for Notches and Cracks," *Journal of Applied Mechanics*, Vol. 35, No. 2, pp. 379–386.

Rooke, D.P. and Cartwright, D.J. (1976), *Compendium of Stress Intensity Factors*, HMSO, London, UK.

Web Crippling Strength of Longitudinally Stiffened Steel Plate Girder Webs Subjected to Concentrated Loading

NELSON LOAIZA, CARLOS GRACIANO and ROLANDO CHACÓN

ABSTRACT

Currently, the AISC *Specification* provides guidance for the calculation of the ultimate strength of unstiffened plate girder webs subjected to concentric edge loads. Specifications consider three categories: local web yielding, web crippling, and sideway web buckling. Based on previous studies, the presence of longitudinal stiffeners in the web has not been considered in the calculation procedures. Longitudinal stiffeners in steel plate girders are primarily used to increase bending. In the last two decades, a number of projects regarding the positive effect of longitudinal stiffening on the strength of plate girder webs to concentrated load have been conducted around the world. The results have shown that this type of stiffening enhances ultimate strength for web crippling, depending on the position of the stiffener that modifies the slenderness of the directly loaded panel and flexural and torsional rigidities of the stiffener. This paper presents a methodology for the consideration of longitudinal stiffening on the ultimate strength of plate girders webs subjected to concentrated loads. The methodology is based on the plastic collapse mechanism observed experimentally, in which plastic hinges are formed in the loaded flange and yield lines result in the portion of the web limited by the loaded flange and stiffener. Then, a closed-form solution accounting for the influence of the stiffener is developed following the current expression available in the AISC *Specification*. Theoretical predictions are compared with available test results, showing that the predicted ultimate loads are in good agreement with experimental results.

Keywords: web buckling, longitudinal stiffeners, ultimate resistance, concentrate load, steel girders.

INTRODUCTION

In the last two decades, a number of research projects regarding the positive effect of longitudinal stiffening on the strength of plate girder webs to concentrated load have been conducted around the world. The results have shown that this type of stiffening enhances ultimate strength for web crippling, depending on the position of the stiffener that modifies the slenderness of the directly loaded panel and flexural and torsional rigidities of the stiffener.

Currently, in the Eurocode (EC3 Part 1-5, 2006), the resistance of steel girder webs to concentrated load is calculated using an χ-λ approach. Lagerqvist and Johansson (1996), after conducting an extensive literature review, proposed a design procedure to calculate the resistance of transversally stiffened girder webs subjected to a concentrated force.

Nelson Loaiza, Ph.D. Student, Universidad Nacional de Colombia. Email: naloaizar@unal.edu.co (corresponding)

Carlos Graciano, Associate Professor, Universidad Nacional de Colombia. Email: cagracianog@unal.edu.co

Rolando Chacón, Associate Professor, Universitat Politècnica de Catalunya. Email: rolando.chacon@upc.edu

Afterward, Graciano (2002) included the effect of longitudinal stiffening into this design procedure.

Thereafter, further investigations have been conducted, particularly in Europe. Seitz (2005) conducted a series of experimental tests on longitudinally stiffened girders to investigate the influence of the patch loading length and the presence of closed section stiffeners. At the same time, Davaine (2005) performed an extensive numerical investigation on both critical load and resistance of longitudinally stiffened webs considering very deep girders, beyond the ranges studied experimentally. Continuing the investigation carried out by Lagerqvist and Johansson (1996), Gozzi (2007) numerically investigated the resistance to concentrated loads of unstiffened plate girders at ultimate and serviceability limit states. In parallel, Clarin (2007) evaluated various ultimate-strength approaches and incorporated these into a calibrated formulation for longitudinally stiffened girder webs. Considering the flange-to-web yield strength inhomogeneities present in the design of bridge girders, Chacón (2009) numerically and experimentally investigated the resistance of hybrid plate girders subjected to concentrated forces. Concerning the use of multiple longitudinal stiffeners, Dall'Aglio (2011) performed a numerical investigation to evaluate the influence of two longitudinal stiffeners in the compression zone on the ultimate strength of girder webs under concentrated loading. Figure 1 shows the nomenclature used for the longitudinal stiffened steel plate girder studied herein.

In spite of the number of research projects demonstrating that longitudinal stiffeners enhance the ultimate strength of plate girder webs subjected to concentrated forces, the latest edition of the AISC *Specification* (AISC, 2016) presents only guidance for the calculation of the ultimate strength of longitudinally unstiffened plate girder webs and webs with vertical stiffeners. Therefore, this paper is aimed at presenting a methodology for the consideration of longitudinal stiffening on the ultimate strength of plate girders webs subjected to concentrated loads. The methodology is based on the plastic collapse mechanism observed experimentally, in which plastic hinges are formed in the loaded flange and yield lines result in the portion of the web limited by the loaded flange and stiffener. The results are compared with various approaches taken from the literature.

ULTIMATE STRENGTH MODELS FOR CONCENTRATED LOADING

Failure Mechanism Proposed by Roberts

Roberts (1981) developed a failure mechanism model for the estimation of the ultimate load of an unstiffened slender I-girder subjected to concentrated forces (Figure 2). The model considers that the external load at plastic collapse is similar to the internal dissipation of plastic energy during a small variation of displacement, δ. This mechanism describes the plastic collapse of the loaded flange subjected to, and the portion of the web beneath, the load. Four plastic hinges are used in this model to represent the mode of failure in the flange and the crippling effect produced in the web panel.
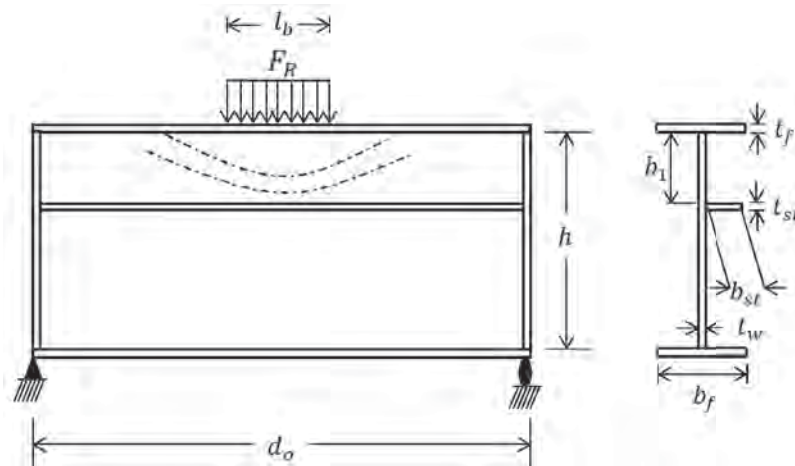

Fig. 1. Notation used for longitudinally stiffened steel plate girder webs subjected to concentrated loading.
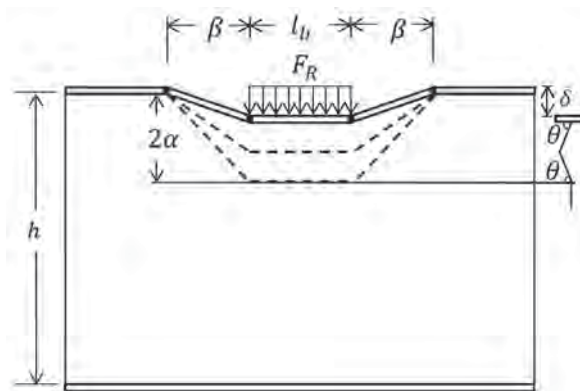

Fig. 2. Failure mechanism of four plastic hinges for longitudinally unstiffened webs.

After several mathematical operations, an expression for the ultimate load, F_R, is found:

$$F_R = 2\sqrt{2}\, t_w^2 \sqrt{\frac{EF_{yw}^2 t_f}{\alpha F_{yf}} + \frac{l_b EF_{yw}^2 t_w^4}{F_{yf}^2 b_f t_f \alpha}} \qquad (1)$$

Correspondingly, the following hypotheses are considered:

- Roberts (1981), based on the observation of its experimental results, determined that the distance α between yield lines in the web measured from the loaded flange (see Figure 2) is a function of the web thickness $\alpha = 25t_w$, then Equation 1 becomes:

$$F_R = \frac{2\sqrt{2}}{5}\, t_w^2 \left[1 + kl_b \left(\frac{t_w}{t_f}\right)^{1.5}\right] \sqrt{\frac{EF_{yw}^2 t_f}{t_w F_{yf}}} \qquad (2)$$

where

$$k = \left(\frac{1}{2\sqrt{2}}\sqrt{\frac{E}{F_{yw}}}\right)\frac{1}{b_f}$$

- Thereafter, both yield strengths for web and flange were assumed equal, $F_{yf} = F_{yw}$, and simplifying the factor k to $3/h$, the ultimate strength to concentrated forces F_R is, therefore:

$$F_R = \frac{2\sqrt{2}}{5}\, t_w^2 \left[1 + 3\left(\frac{l_b}{h}\right)\left(\frac{t_w}{t_f}\right)^{1.5}\right] \sqrt{\frac{EF_{yw} t_f}{t_w}} \qquad (3)$$

- Finally, as a safe approximation, the number $2\sqrt{2}/5$ was rounded off to 0.5.

$$F_R = 0.50\, t_w^2 \left[1 + 3\left(\frac{l_b}{h}\right)\left(\frac{t_w}{t_f}\right)^{1.5}\right] \sqrt{\frac{EF_{yw} t_f}{t_w}} \qquad (4)$$

It should be noticed that after some experimental comparisons, Equation 4 is valid only for short concentrated lengths $l_b/h \leq 0.2$ and a flange-to-web thickness ratio of $t_f/t_w \geq 3$. For a detailed derivation of these formulas, the readers are encouraged to see Roberts (1981).

Nominal Strength of the Web Against Crippling

Using Equation 4, the AISC *Specification* (AISC, 2016) provides a modified formulation for the nominal strength of an unstiffened slender I-girder subjected to concentrated forces. Several equations are proposed in AISC *Specification* Section J10, depending on where the load is applied. From *Specification* Equation J10-4, when the concentrated force is applied at a distance from the member end greater than or equal to $d/2$, the nominal strength is calculated as

$$F_R = 0.80\, t_w^2 \left[1 + 3\left(\frac{l_b}{d}\right)\left(\frac{t_w}{t_f}\right)^{1.5}\right] \sqrt{\frac{EF_{yw} t_f}{t_w}} \qquad (5)$$

and when a concentrated force is applied at a distance from the member end less than $d/2$:

For $l_b/d \leq 0.2$

$$F_R = 0.40\, t_w^2 \left[1 + 3\left(\frac{l_b}{d}\right)\left(\frac{t_w}{t_f}\right)^{1.5}\right] \sqrt{\frac{EF_{yw} t_f}{t_w}} \qquad (6a)$$

For $l_b/d > 0.2$

$$F_R = 0.40\, t_w^2 \left[1 + \left(4\frac{l_b}{d} - 0.2\right)\left(\frac{t_w}{t_f}\right)^{1.5}\right] \sqrt{\frac{EF_{yw} t_f}{t_w}} \qquad (6b)$$

Equation 5 is very similar to the one proposed by Roberts (1981). Furthermore, the influence of longitudinal stiffeners is not considered in the AISC *Specification* for concentrated forces (AISC, 2016).

Resistance to Transverse Forces: EC3 Part 1-5

The Eurocode EC3 Part 1-5 (2006) rules for plated structural elements provides another approximation for the resistance to concentrated forces of slender girders. In contrast to the AISC *Specification* (AISC, 2016), the EC3 Part 1-5 (2006) incorporates the influence of a longitudinal stiffener in the calculation of the resistance to concentrated forces. This design procedure follows a harmonized technique developed by Lagerqvist and Johansson (1996) that consists of calculating the yield resistance, F_y, and the critical buckling load, F_{cr}, of the web panel. Currently, the EC3 Part 1-5 (2006) rules are under review (Chacón et al., 2010; Graciano, 2015), and the following amendments have been suggested:

- First, the yield resistance, F_y, is obtained from a four–plastic hinge mechanism developed by Lagerqvist and Johansson (1996):

$$F_y = F_{yw} t_w l_y \qquad (7)$$

where l_y is the effective load length and is computed using the expression recommended by Chacón et al. (2010) for hybrid girders (plate girders with a yield strength ratio $F_{yf}/F_{yw} \neq 1$), which states that flange-to-web yield resistance ratio should be considered equal to 1 ($F_{yf}/F_{yw} = 1$), due to its diminished influence on the ultimate load:

$$l_y = \left[l_b + 2t_f\left(1 + \sqrt{b_f/t_w}\right)\right] \qquad (8)$$

- Next, the critical buckling load is obtained with Equation 9 proposed by Davaine (2005):

$$\frac{1}{F_{cr}} = \frac{1}{F_{cr1}} + \frac{1}{F_{cr2}} \tag{9}$$

where Equation 9 is an expression that considers an interaction between the critical buckling load, F_{cr1}, established by Graciano and Lagerqvist (2003), and the critical buckling load, F_{cr2}, of the upper web panel was developed by Davaine (2005). First, the critical buckling load F_{cr1} is computed according to classical buckling theory:

$$F_{cr1} = k_{f1} \frac{\pi^2 E}{12(1-\nu^2)} \frac{t_w^3}{h} \tag{10}$$

where k_{f1} is a buckling coefficient obtained from a linear buckling analysis of plate girders subjected to a fixed concentrated force length of $l_b/h = 0.2$ (Graciano and Lagerqvist, 2003). This expression is found in EC3 Part 1-5 (2006) as

$$k_{f1} = 6 + 2\left[\frac{h}{d_o}\right]^2 + \left[5.44\frac{b_1}{d_o} - 0.21\right]\sqrt{\gamma_s} \tag{11}$$

$$\gamma_s = 10.9\frac{I_{st}}{ht_w^3} \leq 13\left[\frac{d_o}{h}\right]^3 + 210\left[0.3 - \frac{b_1}{d_o}\right] \tag{12}$$

where γ_s is the relative flexural rigidity of the stiffener and I_{st} is the moment of inertia of the longitudinal stiffener calculated with respect to its centroidal axis parallel to the web plate. Considering the composed area of stiffener and two portions of the web plate with a width of $15t_w$ on each side of the stiffener weld, Figure 3 illustrates the effective cross-section of open section stiffeners.

Second, the critical buckling load F_{cr2} is obtained from a model proposed by Davaine (2005), in which only a portion of the web panel is studied. This part of the panel has a height of b_1, and it is simply supported, with opposite concentrated forces of lengths $l_b + 2t_f$ and $l_b + 2t_f + 2b_1$ applied to both the upper and lower ends as shown in Figure 4. The purpose of this modification was to correct the increase of ultimate load values found in EC3 Part 1-5 (2006) when the position of the stiffener increases with respect to the loaded flange. In this case, the critical buckling load, F_{cr2}, is calculated, replacing the depth of web panel, D, with the position b_1 of the stiffener

$$F_{cr2} = k_{f2} \frac{\pi^2 E}{12(1-\nu^2)} \frac{t_w^3}{b_1} \tag{13}$$

After performing an eigenvalue analysis, the buckling coefficient k_{f2} is expressed as
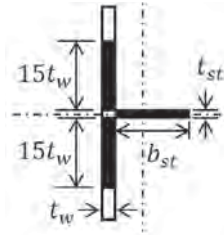

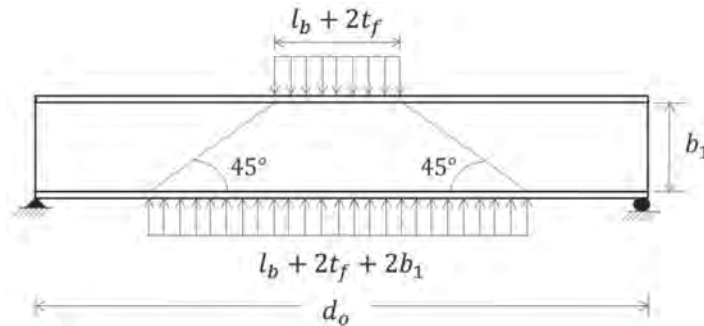Fig. 3. Effective cross area used for calculating I_{st}.

Fig. 4. Simply supported model proposed by Davaine (2005).

$$k_{f2} = \left[0.8 \left(\frac{l_b + 2t_f}{d_o} \right) + 0.6 \right] \left(\frac{d_o}{b_1} \right)^{\left[0.6 \left(\frac{l_b + 2t_f}{d_o} \right) + 0.5 \right]} \quad (14)$$

- Finally, the ultimate load, F_R, is calculated with the χ_F-λ approach, an estimation that reduces the yield resistance, F_y. This reduction is obtained multiplying the resistance function, χ_F, with the aforementioned resistance, F_y.

$$F_R = F_y \chi_F (\overline{\lambda}_F) \quad (15)$$

with the resistance function χ_F equal to

$$\chi_F = \frac{1}{\phi + \sqrt{\phi^2 - \lambda}} \leq 1 \quad (16)$$

and the slenderness parameter λ

$$\overline{\lambda}_F = \sqrt{F_y / F_{cr}} \quad (17)$$

It should be pointed out that Equation 16 was developed by Müller (2003), in which ϕ is a function that depends on the slenderness parameter λ, the imperfection factor α_0, and the plateau length λ_0—values that can be found in different resistance models (Davaine, 2005; Müller, 2003; Gozzi, 2007; Clarin, 2007; Chacón et al., 2012).

$$\phi = 0.5 \left[1 + \alpha_0 (\lambda - \lambda_0) + \lambda \right] \quad (18)$$

Proposed Failure Mechanism for Longitudinal Stiffened Plate Girders

In order to consider the influence of a longitudinal stiffener, Graciano and Edlund (2003) presented a reviewed version of the plastic failure mechanism developed by Roberts and Rockey (1979). In this mechanism, the buckling behavior is affected significantly by the presence of a longitudinal stiffener, mainly because the distance to yield lines in the web α is restricted by the position of the stiffener b_1, as shown in Figure 5. Figure 6 shows the deformed shape obtained in experimental results of longitudinal stiffened webs subjected to concentrated forces (Rockey et al., 1978).

As a result of this behaviour, Graciano and Edlund (2003) proposed a mechanical model, which uses the same mechanism developed by Roberts and Rockey (1979):

$$F_R = 8 F_{yw} t_w^2 \sqrt{\frac{E t_f}{8 \alpha F_{yf}}} + \frac{2 (C_e - \eta) M_w}{\alpha \cos \theta} \quad (19)$$
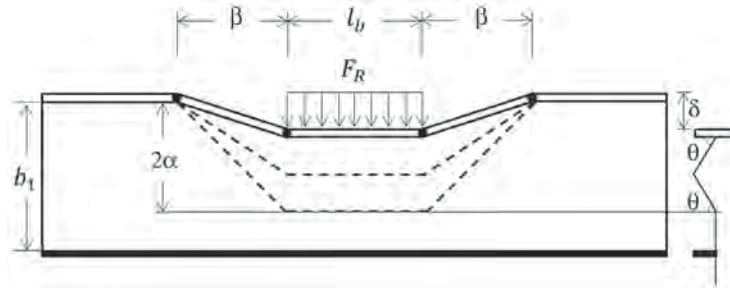

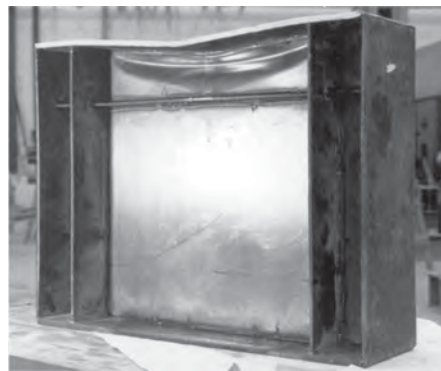*Fig. 5. Failure mechanism of four plastic hinges for longitudinal stiffened webs.*

Fig. 6. Experimental results of web crippling in a longitudinal stiffened girder (Rockey et al., 1978).

The following geometrical parameters are basically the same:

$$\eta = \frac{(4\beta + 2C_e)M_w}{2M_w + F_{yw}t_w\,\alpha\,\cos\theta} \tag{20}$$

$$\beta = \left(\frac{M_f\alpha\,\cos\theta}{M_w}\right)^{1/2} \tag{21}$$

$$\cos\theta = \frac{M_f^2}{6EI_fM_w} \tag{22}$$

and the plastic moments of the web and flange are:

$$M_w = \frac{F_{yw}t_w^2}{4} \tag{23}$$

$$M_f = \frac{F_{yw}b_ft_f^2}{4} \tag{24}$$

As seen in Figures 5 and 6, the position of the yield lines α are restricted by the position of the stiffener b_1. Hence, Graciano and Edlund (2003) conservatively proposed the following values:

$$\alpha = 0.5b_1 \qquad \text{if } b_1/t_w \le 40 \tag{25a}$$

$$\alpha = 20t_wF_{yw}/F_{yf} \quad \text{if } b_1/t_w > 40 \tag{25b}$$

Equation 25b was initially proposed by Roberts and Newark (1997); therefore, the limits to consider the influence of the longitudinal stiffener are $b_1/t_w \le 40$. Otherwise, the stiffener is unable to enhance the load carrying capacity of the girder under concentrated loading.

However, as mentioned earlier, Chacón et al. (2010) demonstrated that the flange-to-web yield strength ratio has no influence on the resistance to concentrated forces for hybrid girders. Consequently, Equation 19 can be rewritten as

$$F_R = 8t_w^2\sqrt{\frac{Et_fF_{yw}}{8\,\alpha} + \frac{2(C_e - \eta)M_w}{\alpha\,\cos\theta}} \tag{26}$$

By means of regression analysis, the position of yield lines α is adjusted herein to obtain a good correlation between experimental ultimate load and theoretical predictions:

$$\alpha = 0.42b_1 \qquad \text{if } b_1/t_w \le 40 \tag{27a}$$

$$\alpha = 17t_w \qquad \text{if } b_1/t_w > 40 \tag{27b}$$

RESULTS

In the previous section, various ultimate-strength models were explained. In this section, a comparative analysis is performed in order to contrast the experimental loads, F_{exp}, with theoretical predictions, F_R. Simple statistics for the ratio F_{exp}/F_R are used for this purpose: maximum and minimum values; mean, m; standard deviation, s; and coefficient of variation, v. Table 1 summarizes 45 experimental test results taken compiled in the literature (Graciano, 2005).

Figure 7 displays the values for the ratio F_{exp}/F_R versus $N°$ of test, corresponding to each mechanism studied. The results have been separated in terms of the type of stiffener, open-section (flat) stiffener, or closed-section (trapezoidal and triangular) stiffener. As expected, the failure mechanism proposed by Roberts (1981) is the most conservative of all, with a mean value $m = 1.85$; see also Table 2. This model also presents a large standard deviation $s = 0.34$, which makes it an unreliable prediction for longitudinally stiffened girder webs. Results obtained with the AISC *Specification* (AISC, 2016) for nominal strength attained a mean value $m = 1.16$, despite that fact that this approach is similar to the one proposed by Roberts (1981). However, it is important to notice that the standard deviation and coefficient of variation are significantly high when taking into account the mean value of predicted load ratio as seen in Table 2. Additionally, it can be observed in Figures 7(a) and 7(b) that predictions based upon Roberts's (1981) estimation of the ultimate load are quite conservative for closed-section stiffeners.

On the other hand, the predictions obtained with the revised EC3 Part 1-5 (2006) for longitudinal stiffened webs are still conservative ($m = 1.82$). Nevertheless, it must be mentioned that the range of the predicted load ratio F_{exp}/F_R is acceptable (max = 2.31; min = 1.17) [Figure 7(c)]. At the same time, Figure 7(d) shows that the predicted strengths using the model proposed herein display a good agreement with experimental test results. As observed in Table 2, the mean value for the ratio F_{exp}/F_R is around $m = 1.23$, and the standard deviation is $s = 0.15$.

Particularizing the results of the proposed model, Figure 8 shows the predicted load ratio F_{exp}/F_R as a function of various geometrical parameters. The results plotted in Figure 8 show a reduced scatter in the ratio F_{exp}/F_R for all values of slenderness ratio, b_1/t_w, and load length-to-width ratio, l_b/d_o, and it slightly increases with the flexural rigidity of the stiffener, γ_s. It is important to mention the proposed model implicitly considers that the stiffener is rigid enough to form a nodal line at the stiffener location.

Table 1. Experimental Results of Stiffened Web Panels			
Author(s)	**Test**	**Numbers of Tests**	**Type of Stiffener**
Carretero and Lebet (1998)	Panel 1-2, Panel 2-2 Panel 4-4, Panel 4-6 Panel 5-1, Panel 6-2	6	All trapezoidal stiffeners
Dubas and Tschamper (1990)	VT07-2, VT07-3 VT07-5, VT07-6 VT08-2, VT08-3 VT08-5, VT08-6 VT09-2, VT09-3 VT09-5, VT09-6 VT10-2, VT10-3 VT10-5, VT10-6	16	8 flat stiffeners 8 V-shaped stiffeners
Bergfelt (1983)	731, 732, 733 734, 735, 736	6	All flat stiffeners
Rockey et al. (1978)	R2, R4 R22 ss, R42 ss	4	All flat stiffeners
Bergfelt (1979)	A12 s, A14 s A16 s, A22 s A24 s, A26 s A32 s, A34 s A36 s	9	All flat stiffeners
Dogaki et al. (1990)	Model 4, Model 5	2	All flat stiffeners
Galea et al. (1987)	P2, P3	2	All flat stiffeners

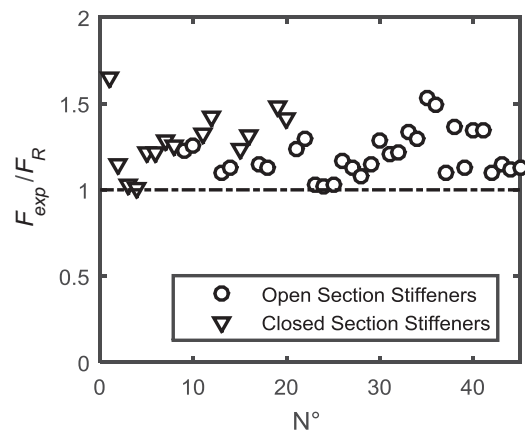| Table 2. Statistics of F_{exp}/F_R					
Methodology	**Min**	**Max**	***m***	***s***	***v***
Roberts (1981) (Eq. 4)	1.38	2.92	1.85	0.34	0.18
AISC *Specification* (AISC, 2016) (Eq. 5)	0.86	1.83	1.16	0.22	0.19
Revised EC3 Part 1-5 (2006) (Eq. 15)	1.13	2.31	1.82	0.30	0.17
Proposed mechanism (Eq. 26)	1.01	1.65	1.23	0.15	0.12
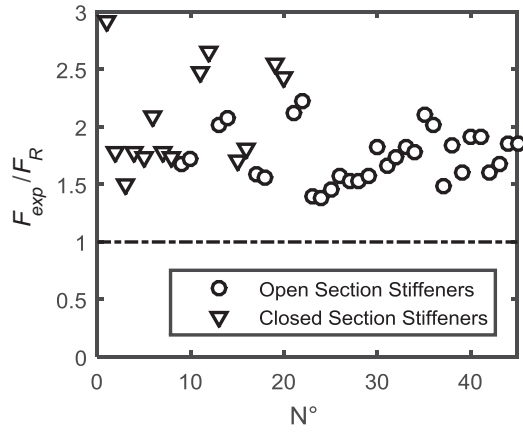
(a) Failure mechanism proposed by Roberts (1981)
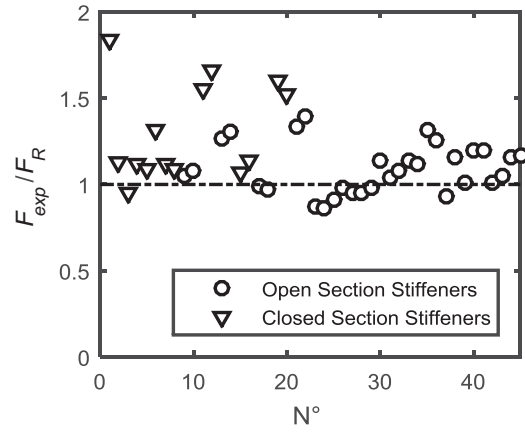
(b) AISC Specification (AISC, 2016)
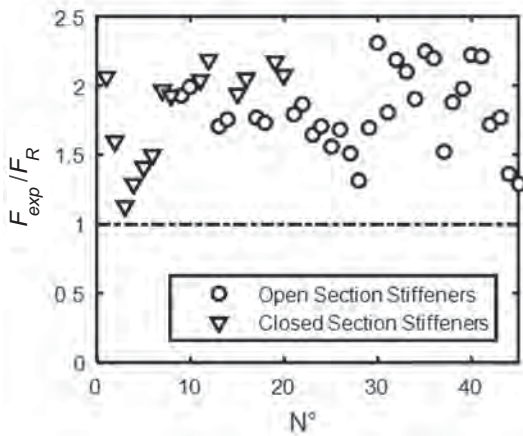
(c) Revised EC3 Part 1-5 (2006)

(d) Proposed mechanism

Fig. 7. Experimental and predicted ultimate load ratio F_{exp}/F_R for longitudinal stiffened webs.

(a) F_{exp}/F_R *vs.* b_1/t_w

(b) F_{exp}/F_R *vs.* s_s/a

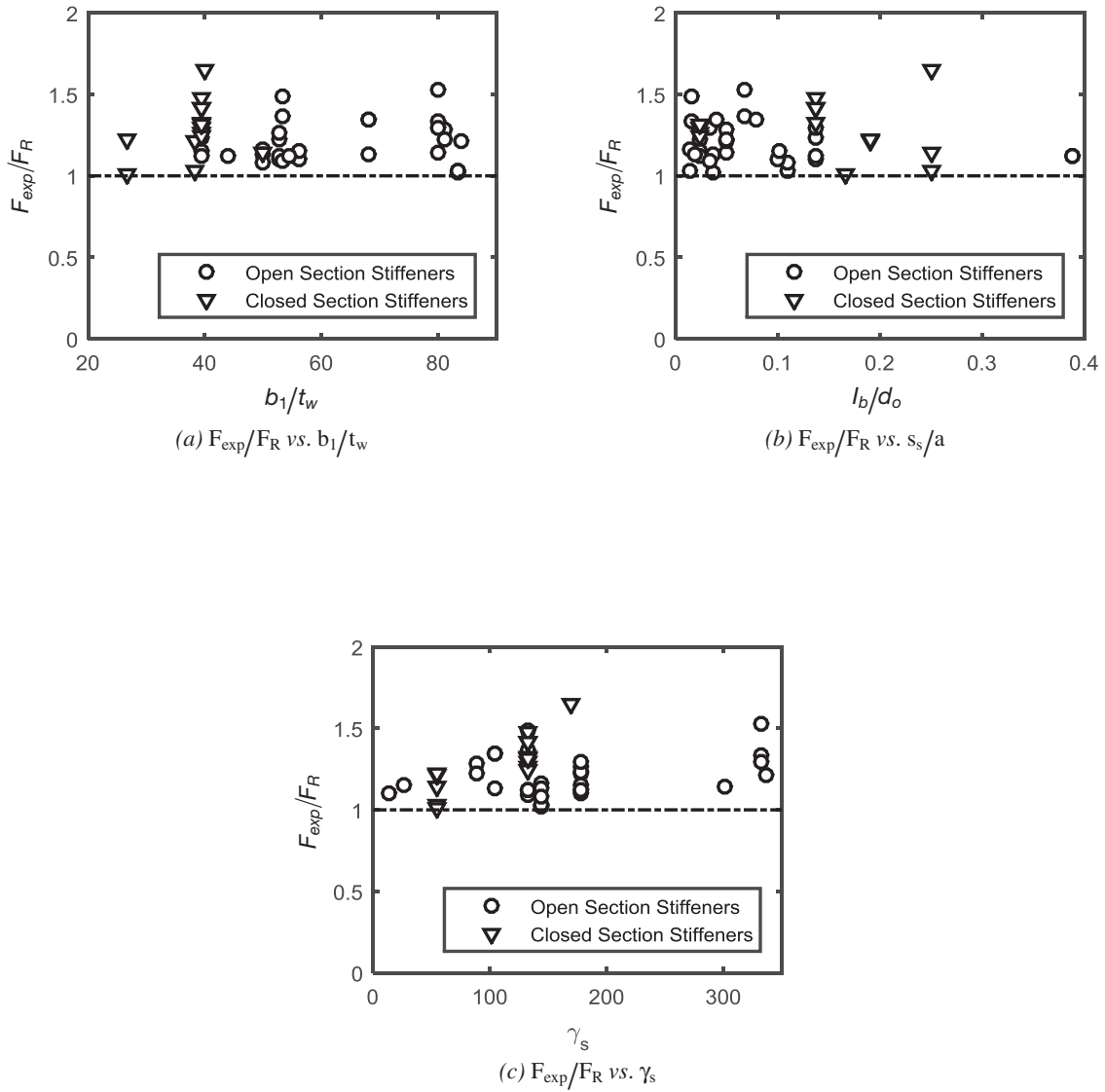*(c)* F_{exp}/F_R *vs.* γ_s

Fig. 8. Experimental and predicted ultimate load ratio F_{exp}/F_R vs. the slenderness ratio b_1/t_w,
load length-to width ratio l_b/d_o, and flexural rigidity of the stiffener γ_s (proposed mechanism).

CONCLUSIONS

In this paper, a methodology for the ultimate-strength prediction of longitudinal stiffened plate girders subjected to concentrated loads is presented. The results of the proposed methodology are compared with three approaches available in the literature. Based on those results, the conclusions are:

- Predicted strengths are conservative when the influence of longitudinal stiffeners is not considered in the prediction model.

- For all types of longitudinal stiffeners studied, the proposed model has a good correlation with the experimental results.

SYMBOLS

C_e	Effective length of the concentrated load $= l_b + 2t_f$
D	Flexural rigidity of unit width of the web plate $= Et_w^3 / 12(1 - v^2)$
E	Young's modulus
F_{yw}	Web yield strength
F_{yf}	Web yield strength
F_{cr}	Critical buckling load
F_{exp}	Experimental ultimate load
F_R	Predicted ultimate load
F_y	Yield resistance
I_f	Moment of inertia of the flange $= b_f t_f^3 / 12$
I_{st}	Effective moment of inertia of the stiffener
M_f	Plastic moment of the flange
M_w	Plastic moment per unit length of the web
b_f	Width of flange
b_{st}	Width of longitudinal stiffener
b_1	Position of longitudinal stiffener
d	Total height of web panel $= h + 2t_f$
d_o	Length of web panel
h	Depth of web panel between the inner surfaces of the flanges
k_f	Buckling coefficient
k_{fl}	Buckling coefficient for longitudinally stiffened plate girders
k_{sl}	Contribution of a longitudinal stiffener to the buckling coefficient, k_{fl}

l_b	Length of concentrated loading
l_y	Effective load length
t_f	Flange thickness
t_{st}	Longitudinal stiffener thickness
t_w	Web thickness
α	Distance to yield lines in the web
α_0	Plateau length
β	"Spread" of plastic hinges in loaded flange
γ_s	Relative flexural rigidity of the longitudinal stiffener $= EI_{st}/Dh$
γ^t	Transition rigidity
δ	Vertical displacement of the concentrated load at the instant of collapse
η	Yielded length of web plate
θ	Angle defining deformation of web prior to collapse
λ_0	Plateau length
λ_F	Slenderness parameter
v	Poisson's ratio
χ_F	Resistance function

REFERENCES

AISC (2016), *Specification for Structural Steel Buildings*, ANSI/AISC 360-16, American Institute of Steel Construction, Chicago, IL.

Bergfelt, A. (1979), "Patch Loading on a Slender Web-Influence of Horizontal and Vertical Web Stiffeners on the Load Carrying Capacity," *Chalmers University of Technology, Steel and Timber Structures*, S 79:1.

Bergfelt, A. (1983), "Girder Web Stiffening for Patch Loading," *Chalmers University Technology, Steel and Timber Structures*, S 83:1.

Carretero, A. and Lebet, J.P. (1998), "Introduction des Forces Concentrées dans les Poutres Élancées," *Construction Métallique*, Vol. 1, pp. 5–18.

Chacón, R. (2009), "Resistance of Transversally Stiffened Hybrid Steel Plate Girders to Concentrated Loads," Ph.D. Thesis, Universitat Politècnica de Catalunya, Departement d´Enginyeria de la Construcció, Barcelona, Spain.

Chacón, R., Braun, B., Kuhlman, U. and Mirambell, E. (2012), "Statistical Evaluation of the New Resistance Model for Steel Girders Subjected to Patch Loading," *Steel Construction*, Vol. 5, No. 2, pp. 10–15.

Chacón, R., Mirambell, E. and Real, E. (2010), "Hybrid Steel Plate Girders Subjected to Patch Loading. Part 2: Design Proposal," *Journal of Constructional Steel Research,* Vol. 66, No. 5, pp. 709–715.

Clarin, M. (2007), "Plate Buckling Resistance–Patch Loading of Longitudinally Stiffened Webs and Local Buckling," Ph.D. Thesis, Luleå University of Technology, Division of Steel Structures, 2007:31, Luleå, Sweden.

Dall'Aglio, F. (2011), "Resistenza di Travi Metalliche a Doppio T con Irrigidimenti Longitudinali Soggette a Carichi Trasversali Concentrati," Ph.D. Thesis. Università Degli Studi di Bologna, Dipartimento di Ingegneria Civile, Ambientale e dei Materiali, Bologna, Italy. [In Italian].

Davaine, L. (2005), "Formulation de la Résistance au Lancement d'une Âme Métallique de Pont Raidie Longitudinalement," Ph.D. Thesis, D05–05, INSA de Rennes, France.

Dogaki, M., Murata, M., Kishigami, N., Tanabe, T. and Yonezeawa, H. (1990), "Ultimate Strength of Plate Girders with Longitudinal Stiffeners under Patch Loading," *Technology Report Kansai University*, Vol. 33, pp. 121–32.

Dubas, P. and Tschamper, H. (1990), "Stabilité Des Âmes Soumises à une Charge Concentrée et à une Flexion Globale," *Construction Métallique*, Vol. 2, pp. 25–39.

Eurocode 3 Part 1-5. (2006), "Design of Steel Structures: General Rules, Supplementary Rules for Planar Plated Structures without Transverse Loading," ENV 1993-1-5.

Galea, Y., Godart, B., Radouant, I. and Raoul, J. (1987), "Test of Buckling of Panels Subject to In-Plane Patch Loading," *Proceedings of the ECCS Colloquium on Stability of Plate and Shell Structures*, pp. 65–71.

Gozzi, J. (2007), "Patch Loading Resistance of Plated Girders-Últimate and Serviceability Limit State," Ph.D. Thesis, Luleå University of Technology, Division of Steel Structures, 2007:30, Luleå, Sweden.

Graciano, C. (2002), "Patch Loading—Resistance of Longitudinally Stiffened Steel Girder Webs," Ph.D. Thesis, Luleå University of Technology, Division of Steel Structures, 2002:18, Luleå, Sweden.

Graciano, C. (2005), "Strength of Longitudinally Stiffened Webs Subjected to Concentrated Loading," *Journal of Structural Engineering*, ASCE, Vol. 131, No. 2, pp. 268–278.

Graciano, C. (2015), "Patch Loading Resistance of Longitudinally Stiffened Girders—A Systematic Review," *Thin-Walled Structures*, Vol. 95, pp. 1–6.

Graciano, C. and Edlund, B. (2003), "Failure Mechanism of Slender Girder Webs with a Longitudinal Stiffener under Patch Loading," *Journal of Constructional Steel Research*, Vol. 59, No. 9, pp. 27–45.

Graciano, C. and Lagerqvist, O. (2003), "Critical Buckling of Longitudinally Stiffened Webs Subjected to Compressive Edge Loads," *Journal of Constructional Steel Research*, Vol. 59, No. 9, pp. 1,119–1,146.

Lagerqvist, O. and Johansson, B. (1996), "Resistance of I-Girders to Concentrated Loads," *Journal of Constructional Steel Research*, Vol. 39, No. 2, pp. 87–119.

Müller, C. (2003), "Zum Nachweisebener Tragwerkeaus Stahlgegenseitliches Ausweichen," Ph.D. Thesis, RWTH Aachen, Lehrstuhlfür Stahlbau, ShakerVer-lag No.47.

Roberts, T.M. (1981), "Slender Plate Girders Subjected to Edge Loading," *Proceedings of the Institution of Civil Engineers*, Vol. 2, No. 71, pp. 805–819.

Roberts, T.M. and Newark, A.C.B. (1997), "Strength of Webs Subjected to Compressive Edge Loading," *Journal of Structural Engineering*, ASCE, Vol. 123, No. 2, pp. 176–183.

Roberts, T.M. and Rockey, K.C. (1979), "A Mechanism Solution for Predicting the Collapse Loads of Slender Plate Girders when Subjected to In-Plane Patch Loading," *Proceedings of the Institute of Civil Engineering*, Vol. 67, No. 2, pp. 155–175.

Rockey, K., Bergfelt, A. and Larsson, L. (1978), "Behaviour of Longitudinally Reinforced Plate Girders when Subjected to Inplane Patch Loading," *Chalmers University of Technology, Steel and Timber Structures*, S 78:19.

Seitz M. (2005), "Tragverhalten Längsversteifter Blechträger Unter Quergerichteter Krafteinleitung," Ph.D. Thesis, Universität Stuttgart, Mitteilung des Instituts für Konstruktion und Entwurf Nr. 2005–2. [In German].

Guide for Authors

Scope   *Engineering Journal* is dedicated to the improvement and advancement of steel construction. Its pages are open to all who wish to report on new developments or techniques in steel design, research, the design and/or construction of new projects, steel fabrication methods, or new products of significance to the uses of steel in construction. Only original papers should be submitted.

General   Papers intended for publication should be submitted by email Margaret Matthew, Editor, at matthew@aisc.org.

The articles published in the *Engineering Journal* undergo peer review before publication for (1) originality of contribution; (2) technical value to the steel construction community; (3) proper credit to others working in the same area; (4) prior publication of the material; and (5) justification of the conclusion based on the report.

All papers within the scope outlined above will be reviewed by engineers selected from among AISC, industry, design firms, and universities. The standard review process includes outside review by an average of three reviewers, who are experts in their respective technical area, and volunteers in the program. Papers not accepted will not be returned to the author. Published papers become the property of the American Institute of Steel Construction and are protected by appropriate copyrights. No proofs will be sent to authors. Each author receives three copies of the issue in which his contribution appears.

Manuscripts   Manuscripts must be provided in Microsoft Word format. Include a PDF with your submittal so we may verify fonts, equations and figures. View our complete author guidelines at **www.aisc.org/ej**.